2019

Conformational Dynamics of the Nuclear Pore Complex Studied With Coarse-Grained Modelling and Polarized Light Microscopy

Joan Pulupa

CONFORMATIONAL DYNAMICS OF THE NUCLEAR PORE COMPLEX STUDIED WITH COARSE-GRAINED MODELLING AND POLARIZED LIGHT MICROSCOPY

A Thesis Presented to the Faculty of

The Rockefeller University

in Partial Fulfillment of the Requirements for

the degree of Doctor of Philosophy

by

Joan Pulupa

June 2019

CONFORMATIONAL DYNAMICS OF THE NUCLEAR PORE COMPLEX STUDIED WITH COARSE-GRAINED MODELLING AND POLARIZED LIGHT MICROSCOPY

Joan Pulupa, Ph.D.

The Rockefeller University 2019

In my thesis work, I explored the organization and dynamics of the nuclear pore complex (NPC) through coarse-grained modelling and polarized-total internal reflection fluorescence (pol-TIRF) microscopy.

The NPC is a large (~120 MDa in humans) macromolecular assembly that controls the flow of molecules into and out of the nucleus. The NPC is a key regulator of intracellular trafficking, nuclear organization, and gene expression. The study of this cellular gatekeeper is hampered by its size and complexity, as well as the difficulty of measuring protein dynamics *in vivo*.

Although various models for how cargo translocates the NPC have been proposed, the mechanism remains unclear. However, most models for transport propose a crucial role for the phenylalanine-glycine nucleoporins (FG-Nups). I constructed a coarse-grained model to investigate the dynamics of these proteins. My coarse-grained model was able to recapitulate *in vivo* experimental results previously measured in our lab. My results also suggest that, at the time-scale of cargo translocation, some of the FG-Nups are highly mobile and capable of translocating back and forth across the NPC in milliseconds. This coarse-grained computational model and its results will be discussed in Chapter 2.

The entire NPC and its constituent nucleoporins (Nups) have been subject to a great many structural studies; however, monitoring the dynamics of the NPC *in vivo* has proven to be highly difficult. In order to overcome this challenge, I have built and validated a series of fluorescent orientational sensors. These sensors can be used in conjunction with a pol-TIRF imaging scheme to resolve the orientations and dynamics of specific Nups inside individual NPCs within living cells. By rigidly conjugating mEGFP to various Nups in the scaffold rings of the NPC, I have been able monitor Nups within the Y-shaped complex, the adaptor ring, and the inner channel ring of the NPC. In Chapter 3, I will describe the tools I have built to test NPC dynamics.

I proceeded to measure the orientations and dynamics of the Nups under different transport conditions with these tools. In Chapter 4, I show that Nup54, a member of the inner channel ring, undergoes a shift in conformation under a variety of transport conditions. An orientational shift was not observed in Nup133, a member of the Y-shaped complex. These results suggest that the inner channel ring may reorganize with respect to the NPC in response to cargo translocation.

In the final chapter of this thesis, I explore the implications of our findings and outline the immediate future directions of this work. I will close by describing how polarization microscopy can be applied to other biological systems and proposing some basic technological improvements to this technique.

a Vincente y Feliciana Pulupa

ACKNOWLEDGEMENTS

I have been incredibly fortunate throughout my life to have been inspired and supported in my pursuit of science by so many different people. I would like to first acknowledge my advisor, Sandy Simon, without whom the following work would have been impossible. His passion for science and genuine curiosity for the world around us is contagious. I will be forever grateful for all he has taught me, and look forward to many fascinating discussions on all matter of topics in the years to come (hopefully some accompanied by hikes!). Sandy has truly motivated and inspired me to continue on in academic science, while providing me the tools and support to succeed in my graduate career.

I would also like to thank all the members of the Simon lab, both for ensuring that our lab is *never* a dull place and for ensuring that (in spite of the chaos) we never forsake scientific rigor. I cannot imagine a more exciting place to have done my thesis work.

The pol-TIRF microscopy described in Chapters 3 and 4 would never have been possible without the beautiful microscope built by Daniel Johnson, a thoughtful and kind post-doc whose intellectual fingerprints are all over the work I have been able to achieve. In addition, Michelle Itano, Constantin (Nick) Takacs, Rachel Belote, Marina Bleck, Gabriella Spitz-Becker, Marcello Im, Xiao Wang, Bassem Shebl, and Mike Tomasini have provided me with friendship and scientific discourse in the lab. Melissa Jarmel has been so much more than a labmate, a true partner-in-crime and a supportive and well-loved friend.

The work presented in this thesis has benefited from two talented undergraduates who worked with me through the SURF program, Brennan Carman and Sarah Brantley, as well as a summer high school student, Quintessa Velez.

I truly owe a great debt of gratitude to Harriet Prior, a talented and motivated technician who joined our lab (and this project) in July. Since coming onto this project, Harriet has enthusiastically taken up the cause of the NPC and has made immense contributions to the project! Harriet, I am so thankful for all you do.

I would also like to enthusiastically thank Elias Coutavas from the Blobel lab. His kindness has been inspiring and heartwarming throughout my time at Rockefeller. Whether it is a generous gift of an antibody, a plasmid, a thoughtful conversation about the NPC, or a bottle of wine from a barbeque, his generosity is unsurpassed!

A big thanks is due to my committee members, Cori Bargmann and Mike Rout. My committee meetings were always filled with interesting intellectual conversation and fantastic insights.

I would like to thank the support of everyone at the Rockefeller Dean's Office. They have made the administrative logistics of doing a PhD nonexistent and have grown to be my friends during my time here at Rockefeller.

I would like to thank my HHMI Gilliam Family. This group of talented peers is constantly amazing, rejuvenating, and inspiring me.

Any professional success I have achieved is ultimately built upon the foundation laid by my family and friends. My grandparents, parents, and siblings

mean the world to me and (especially as the youngest of four!) have shaped me into who I am today. Mom and Dad clearly showed what nightly reading can do to instill a love of learning in children, as all of us are inexplicably over-educated. Patrick and Marc, thank you for being the best big brothers I could hope for! Katie María, my favorite sister, thank you for being my (sometimes) gemela and (more often) my wise older sister.

Thank you also to all my friends, near and far, Dre Dre, Bren, Sarah Jane, Allie, Charity, Andrea, Will, Laura, May, and Dylan. Your love and support has made doing 7 years of challenging work possible! I love all of you.

Lastly, I'd like to thank my husband, Timothy. You have taken care of me when I have not taken care of myself, supported me when I could not support myself, and always, always loved me. You keep me sane and grounded. I'll never be able to thank you enough, and cannot wait to see what adventure life brings us next!

TABLE OF CONTENTS

LIST OF FIGURES

LIST OF TABLES

LIST OF ABBREVIATIONS

AFM	atomic force microscopy
CM	complete media
DN	dominant negative
EOM	electro-optic modifier
FG	phenylalanine-glycine
FG-Nup	FG-repeat Nup
FG4	FG-FG off rate of 10^4/s
FG5	FG-FG off rate of 10^5/s
FG6	FG-FG off rate of 10^6/s
FG7	FG-FG off rate of 10^7/s
FG_{off}	FG-FG off rate of 10^{∞}/s
FRET	Förster resonance energy transfer
HBSS	Hank's Buffered Salt Serum
kap	karyopherin
LANS	Light Activated Nuclear Shuttle
NES	nuclear export signal
NLS	nuclear localization signal
NPC	nuclear pore complex
Nup	nucleoporin
PAIRS	Pairwise Agent Interaction with Rational Superposition
pol-TIRF	polarized-TIRF
POM	pore membrane protein
R_g	radius of gyration
R_H	radius of hydration
RNP	ribonuclearprotein
TB	transport buffer
TIRF	total internal reflection fluorescence
WGA	wheat germ agglutinin

CHAPTER 1: INTRODUCTION

The subject of the thesis is the organization and dynamics of the nuclear pore complex (NPC). This chapter provides the biological context for questions that will be addressed and provides background for the computational and experimental techniques used in the completion of the thesis research.

I will begin by providing a general introduction to the NPC, and then proceed to summarize what is known about the architecture and organization of the NPC. I will next include an introduction to cargo translocation and the current models the transport of cargos through the NPC.

Many of these transport models can be distinguished from one another because they necessitate different behaviors from a class of NPC proteins called the phenylalanine-glycine nucleoporins (FG-Nups). The subject of Chapter 2 of this thesis is my attempt to construct a coarse-grained computational model of the NPC. I will explain what other computational models have been created to elucidate the dynamics of these FG-Nups.

Next, I will introduce the idea of conformational plasticity in the NPC and explain how it has been observed over the years. The subject of Chapters 3 and 4 of this thesis are attempts I have made to measure the conformational dynamics of the NPC. I have probed the flexibilities of different scaffold nucleoporins, and in this chapter I will provide an introduction to the scaffold domains that I have surveyed. I will close the introduction by providing a brief introduction to polarized light microscopy, the technique that I used to monitor conformational dynamics.

1.1 The Nuclear Pore Complex (NPC): A General Overview

Eukaryotic cells are defined by the compartmentalization of their genomic DNA into a nucleus, a double membrane-bound organelle. Biomolecular cargo is able to enter and exit the nucleus, bypassing this barrier by transiting through the nuclear pore complexes (NPCs). By selectively allowing transport through this membrane through NPCs, the cell both protects the DNA from viruses and allows an additional layer of control for the temporal expression of genes.

Although small molecules can freely diffuse through the NPC, the NPC is capable of selectively transporting specific cargoes while restricting the passage of cargoes sized over 30-60 kDa (Timney et al., 2016). As result, regulation of this selective transport impacts many cellular functions. Key transport events include the export of the mRNAs that are synthesized inside of the nucleus, and the export of 60S and 40S ribosomal subunits that are assembled inside of the nucleus and transported into the cytoplasm. Conversely, nuclear proteins must also be imported, often in a regulated fashion. For example, gene expression can be temporally controlled by selectively transporting certain transcription factors into the nucleus, and proteins can be differently regulated in the nucleus and the cytoplasm by maintaining different proteasome populations in either compartment. In this manner, the NPC serves as a key regulator of intracellular trafficking, nuclear organization, and gene expression.

As an essential modulator of cell behavior and health, the NPC is associated with many pathological conditions. NPC proteins have been implicated in an array of cancers through three distinct routes: chromosomal translocations that generate

fusion proteins, changes in protein levels, and single point mutations (Simon and Rout, 2014). Many viruses interact extensively with the NPC to disrupt its function. HIV-1 hijacks nucleoporins as the virus exits the nucleus (Monette et al., 2011). Some viruses, such as poliovirus and Ebola, disrupt or alter protein import into the nucleus, whereas other viruses, such as influenza A, inhibit the export of mRNAs (Gustin and Sarnow, 2001; Satterly et al., 2007; Shabman et al., 2011). The current research indicates that the viral inhibition of host NPCs serves to both inhibit immune responses and allow viruses to hijack host NPC machinery.

Although some of the biophysical properties of individual Nups have been characterized *in vitro*, the study of this important cellular gatekeeper has been greatly hampered by its size and complexity, and the difficulty of following the dynamics of molecules in living cells.

1.2 Architecture and Organization of the NPC

Although the nucleotide sequences of the Nup genes have diverged significantly over evolution, the basic architecture of the NPC has remained fundamentally conserved (Alber et al., 2007a, 2007b; Brohawn et al., 2008; Devos et al., 2006; Franks et al., 2016; Kim et al., 2018; Kosinski et al., 2016). The basic architecture of a NPC is a cylindrical channel with its axis perpendicular to the nuclear envelope. This cylindrical channel is composed of proteins that form an eight-spoked core. NPCs are composed of ~30 distinct nucleoporin proteins (Nups). Since some are in 8, 16, or 32-fold symmetry, an individual NPC from different species has ~500-1,000 total proteins (Alber et al., 2007b; Brohawn et al., 2008; Devos et al., 2006; Franks et al., 2016; Hoelz et al., 2011). Proteomics suggest that the yeast NPC is approximately 50 MDa (Allen et al., 2001) and that the mammalian NPC is approximately 110 MDa (Reichelt et al., 1990).

The most heavily studied NPCs are those from yeasts and vertebrates, both members of Opisthokonta, a taxon of the eukaryotes that includes fungi and metazoa (Adl et al., 2012; Obado et al., 2016). Within these NPCs, Nups historically have been divided into three different classes: the pore membrane proteins (POMs), core scaffold Nups, and FG-Nups (Figure 1) (Alber et al., 2007a; Devos et al., 2004). However, more recent work has introduced another class of Nups, known as the linker Nups, which serve as flexible connectors between subcomplexes within the NPC (Fischer et al., 2015; Kim et al., 2018; Teimer et al., 2017). POMs contain trans-membrane domains and membrane binding motifs that anchor the NPC to the nuclear envelope. Core scaffold Nups are the structural

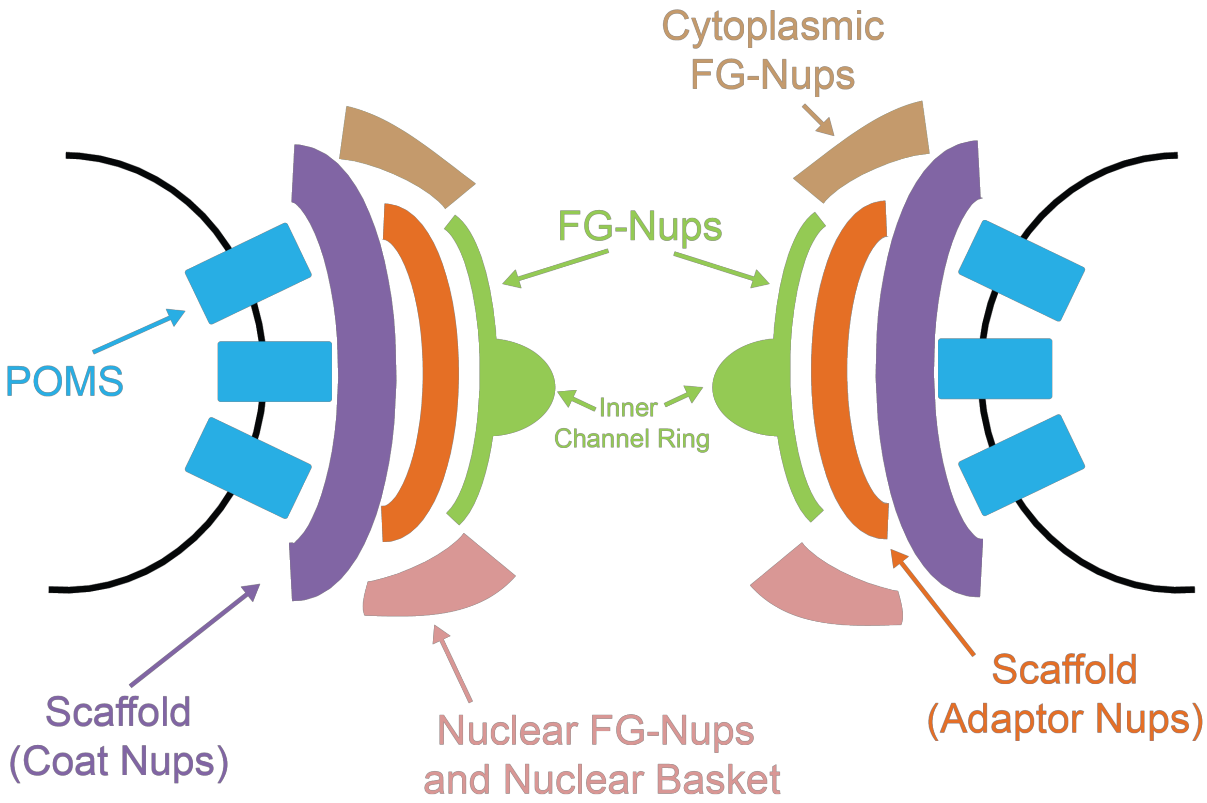

Figure 1. Structure and Composition of the NPC

The nuclear envelope is shown here as black; POMs are shown in blue; Scaffold/Coat Nups are shown in purple; Scaffold/Adaptor Ring Nups are shown in orange; Cytoplasmic FG-Nups are shown in brown; Central FG-Nups are shown in green; Nuclear FG-Nups and the Nuclear Basket are shown in pink.

proteins that make up the major architecture of the NPC and most of its mass, these historically have been further divided into Coat Nups and Adaptor Nups. These proteins anchor to the nuclear envelope and POMs. Mounted onto the scaffold Nups are the FG-Nups. The FG-Nups contain intrinsically disordered regions (IDRs) called FG-domains that protrude into the lumen of this channel. FG-Nups can be further divided into cytoplasmic FG-Nups, central FG-Nups (including an inner channel ring), and nuclear FG-Nups. The FG-domains are believed to form the selectively permeable barrier that prevents non-specific cargo from translocating the NPC (Fahrenkrog et al., 1998; Keminer and Peters, 1999; Kiseleva et al., 2004; Paine and Feldherr, 1972; Paine et al., 1975).

Even though these organizing principles of the NPC appear to be largely shared across eukaryotes, emerging data suggest that there are some organizational differences between different taxa and within individual organisms. Although approximately two thirds of Nups proteins have been identified in the last eukaryotic common ancestor via comparative genetic studies (Neumann et al., 2010), some Nups have remarkably low conservation across species (for example, yeast Nup133 and human Nup133 share only 18% amino acid identity in a ~360 amino acid region (Vasu et al., 2001). Proteomics analysis of a divergent eukaryote (*Trypanosoma brucei*) has shown that even though only five Nups were easily identified via sequence homology, 22 Nups were found when the primary sequences were searched for features associated with known Nups. These Nups, which were confirmed via GFP-tagging, showed remarkable similarity in number, molecular weight, and architecture to the opistokont proteins, suggesting that they are the

homologs despite limited sequence similarity (DeGrasse et al., 2009). Although there is a strong degree of conservation in Nup components, there are some notable differences that exist between mammalian NPCs and yeast NPCs. For example, Nup358 (Ran-binding protein 2), a 358 kDa protein that regulates cellular transport is only found in metazoans (Cronshaw et al., 2002; Wu et al., 1995), and three Nups, Nup155, Nup35, and Nup98 in vertebrates, are duplicated into Nup157/Nup170, Nup53/59, and Nup100/116/145N (Beck and Hurt, 2016). Tpr1, another vertebrate Nup, is duplicated into yeast Mlp1/Mlp2 (Strambio-de-Castillia et al., 1999). The yeast and the human NPC have been characterized on an architectural level, even in these two species differences emerge between their structures. For example, the vertebrate outer ring composed of the Nup84 complex, or Y-shaped complex, is formed from two reticulated rings in vertebrates, but only made of a single ring in yeast (Alber et al., 2007b; Bui et al., 2013; Fernandez-Martinez et al., 2012). Moreover, Nup358 is a major component in an outer cytoplasmic ring in vertebrates, but is not present in yeast (von Appen et al., 2015; Kosinski et al., 2016). Recently, the structure of the NPC from *Chlamydomonas reinhardtii* was characterized with cryo-electon tomography. From this structure, this NPC was observed to have an inner ring of unexpectedly large diameter and other rings that exhibited asymmetric oligomeric states that have not been observed in any other NPCs studied (Mosalaganti et al., 2018). NPCs with different Nup stoichiometries have been observed in humans (Ori et al., 2013). Different expression levels of Nups have been observed in different cell types (D'Angelo et al., 2012; Gomez-Cavazos and Hetzer, 2015; Lupu et al., 2008). Compositional and structural flexibilities in the NPC

underscore the complexity of this macromolecular complex, and their effects on transport and regulation are so far uncharacterized, but remain exciting future avenues of research in the field.

1.3 Transport Through the NPC

Although there are key differences between the structural Nups, all species characterized possess FG-Nups, whose FG-domains form a diffusion barrier for non-specific cargo.

The filamentous domains of the FG-Nups of all species possess characteristic phenylalanine-glycine (FG) repeat motifs, and a single NPC contains thousands of these repeat motifs. The FG-domains can self-associate and the FG-repeats have been predicted to bind to other FG-repeats via hydrophobic interactions (Ader et al., 2010; Frey and Görlich, 2007; Frey et al., 2006; Kraemer et al., 1994). However, the reports of the strength of these FG-FG interactions have varied over orders of magnitude (Kuss et al., 2013; Patel et al., 2007; Rangl et al., 2012). Indeed, some groups have suggested that the hydrophobic interactions are negligible (Hayama et al., 2018). The FG repeat domains also bind to karyopherins (kaps), chaperone complexes that mediate transport in and out of the nucleus (Radu et al., 1995; Wozniak et al., 1998). Kaps are also referred to in the literature as importins, exportins, and nuclear transport factors, for the remainder of this document I will use the “kap” nomenclature to refer to this class of proteins.

The kaps associate with nuclear localization signals (NLSs) or nuclear export signals (NESs) on cargo proteins, enabling selective translocation of cargo because the kaps are also capable of binding to the FG-Nups, and thus these complexes can

infiltrate the diffusion barrier. Usually, the directionality of translocation is coupled to interactions with the nuclear GTPase Ran (Moore and Blobel, 1993; Schwoebel et al., 1998).

Once cargo with an NLS reaches the nuclear side of the NPC, RanGTP binds to the kap and induces a conformational change, causing it to release the cargo. When cargo with an NES reaches the cytoplasmic side of the NPC, RanGAP and Ran binding proteins disassemble export complexes (Kutay et al., 2000; Lei and Silver, 2002; Moore and Blobel, 1993; Smith et al., 2002). Kaps are largely conserved across eukaryotes, such that a rice karyopherin-β1 will transport GFP tagged with a viral (SV40) NLS in permeabilized HeLa cell (Jiang et al., 1998).

This selective barrier prevents the translocation of non-specific cargo while allowing for the rapid transport of select cargo, thousands of events per pore per second (Görlich and Kutay, 1999; Lei and Silver, 2002; Moore and Blobel, 1993; Ribbeck and Görlich, 2001; Wälde and Kehlenbach, 2010). Indeed, some cargo have been seen to transit the pore on millisecond time scales (Sun et al., 2008; Yang et al., 2004). However, some other estimations of the total transit time of endogenous cargo, such as the pre-ribosome in yeast, have been estimated to be as long as ~90 milliseconds (Delavoie et al., 2019).

1.4 Models of Transport

Numerous different models exist for the exact mechanism of selective transport, many of which are not mutually exclusive. What follows is a brief summary of the fundamental features of each:

Selective phase:

The selective phase model postulates that interactions between FG-repeats on different FG-Nups lead to the creation of a cross-linked gel (Frey et al., 2006; Ribbeck and Görlich, 2001). Under this model, NLS cargo binds to a kap and outcompetes FG-FG interactions for FG binding sites. This competition results in the cargo melting into the meshwork of FG-FG filaments, enabling transport into the cell through repeated steps of binding and melting.

Entropic exclusion:

The entropic exclusion model posits that the unstructured FG-Nups occupy space and prevent the passage of non-NLS cargo over a certain size (Rout et al., 2003). Since NLS cargo can bind FG-Nups, NLS-cargo is capable of overcoming the entropic barrier of entering the pore, whereas non-NLS cargo will be excluded. The competition model of transport proposes that the presence of NLS cargo enhances the ability of the NPC to exclude non-NLS cargo by occupying the available space and binding sites within the NPC (Jovanovic-Talisman et al., 2009).

Reduction of dimensionality:

This model proposes that once a kap binds to an FG-binding site, it can easily and rapidly switch from binding site to binding site (Peters, 2009).

A kap experiencing a two-dimensional random walk over the surface of the filament meshwork could be faster than the three-dimensional random walk of non-NLS cargo.

Selective gating/collapse model:

This model maintains that the FG-Nups form a meshwork that prevents the diffusion of non-specific cargo (Lim et al., 2007). When NLS-tagged cargo binds to the FG-repeats, the corresponding FG-Nups undergo a conformational change that enables the cargo to enter the nucleus.

The forest/tube gate/copolymer brush gate model:

This model suggests that the tips of some FG-Nups coalesce into a diffusive barrier in the center of the NPC while their ‘stalks’ form an extended bush zone along the periphery. Under this model, the FG-Nups behave in a ‘tree-like’ manner and provide a diffusive landscape that can be penetrated by the transport factors but not by other macromolecules (Ando et al., 2014; Yamada et al., 2010).

Brownian ratchet:

This model of transport suggests that a given FG-Nup binds to the kap-cargo complex on one side of the nuclear envelope and then diffuses through the

NPC, bound to the same FG-Nup or a restricted set of FG-Nups (Mincer and Simon, 2011; Simon et al., 1992). When the cargo reaches the opposite side of the nuclear envelope, Ran-GTP or RanGAP, and Ran binding proteins, sever the bond between the FG-Nup and the cargo, effectively preventing the cargo from diffusing back across.

Even though little agreement exists on the mechanism of cargo transport, most models posit a critical role for the FG-Nups. Although recent structural work has allowed localization of individual Nups within the mammalian NPC (von Appen and Beck, 2016; Kosinski et al., 2016; Lin et al., 2016; Stuwe et al., 2015), *in vivo* measurements of the dynamics and orientations of the FG-Nups remain elusive.

Characterizing these FG-Nups could be essential for elucidating the mechanism of NPC transport. The *in vivo* study of these FG-Nups is severely limited by their unstructured domains, symmetries, and packing within the NPC.

1.5 Computational Simulations of the NPC

Computational simulations of the entire NPC and its components have provided insight into the potential dynamics and interactions within the NPC. Molecular dynamics simulations have explored the nature of interactions between FG-Nup domains and between FG-Nups and kaps (Gamini et al., 2014; Miao and Schulten, 2010). Unfortunately, molecular dynamics simulations are currently limited to timescales under a microsecond, whereas transport occurs on a millisecond timescale. In addition, these simulations cannot yet recapitulate the complexity of the NPC with its multiple rings of proteins. Therefore, some groups have used coarse-grained simulations to either reach the timescales of transport or incorporate the complexities of the NPC. The NPC is amenable to coarse-grained computational modeling as a macromolecular machine because many of its biophysical properties, such as the anisotropy of FG-Nups at various locations along their length (Atkinson et al., 2013), the approximate locations of their anchor regions and the arrangements of other Nups (Alber et al., 2007b), approximate Nup stoichiometry (Cronshaw et al., 2002; Rabut et al., 2004; Rout et al., 2000), and predicted binding of FG-Nups with kaps are reported in the literature (Bayliss et al., 1999, 2002; Kapinos et al., 2014; Patel et al., 2007).

Our group previously modeled the NPC without invoking an *a priori* mechanism of transport using generic homogeneous FG-Nups arranged in rings of eight-fold symmetry that were evenly spaced through the cylindrical pore (Mincer and Simon, 2011). In order to characterize the local environment of the NPC and probe the electrostatic potential of the pore, some groups

have used coarse-grained amino acid sequences to render predicted electrostatic fields and predict cargo's interactions with these fields (Ando et al., 2014; Tagliazucchi et al., 2013). More recently, the role of 'like charge regions' in the formation and regulation of the selective barrier of the NPC has been studied, suggesting that positive 'like charge regions' play a role in enabling FG-Nups to maximize interactions and cover a larger space within the lumen of the NPC (Peyro et al., 2015a, 2015b). Likewise, simulations suggest the hydrophobic and electrostatic properties of the amino acid sequences of FG-Nups contribute to the arrangement of the filament mass within the lumen of the NPC (Ghavami et al., 2014). Other coarse-grained models probe cargo translocation through the pore, attempting to capture the necessary components of a selective transport mechanism (Mincer and Simon, 2011; Moussavi-Baygi et al., 2011; Zilman et al., 2007). These models include three-dimensional (Mincer and Simon, 2011), two-dimensional (Mincer and Simon, 2011; Moussavi-Baygi et al., 2011a; Zilman et al., 2007), and one-dimensional models (Zilman et al., 2007). Even though these simulations attempt to capture the dynamics of the pore, many assume that FG-Nup filaments are tethered at uniform positions inside the scaffold of the NPC and that binding sites are distributed homogenously along the FG-Nup filaments (Mincer and Simon, 2011; Moussavi-Baygi et al., 2011a; Zilman et al., 2007), which may obfuscate the underlying molecular interactions and the dynamics of the FG-Nups. More recent simulations have explored the interactions of FG-Nup filaments with each other and with kaps (Vovk et al., 2016; Zahn et al., 2016), yielding different results for how FG-Nups might behave in the lumen of the NPC. Coarse-grained modeling of FG-

Nup filaments tethered in the NPC suggests that the intrinstically disordered FG-Nups enable the maintenance of a diffusive barrier through their rapid Brownian motion (Mincer and Simon, 2011), reconstructing itself mere microseconds after a local disruption by a cargo (Moussavi-Baygi and Mofrad, 2016).

In Chapter 2, I will describe coarse-grained computational model that I built in order to probe the behaviors of the FG-Nups at physiologically relevant time scales.

1.6 Plasticity of the NPC Scaffold

In recent years, the widely held view has been that the Nups form a rigid scaffold; however, both historical studies and recent advances in the field have indicated that there may be extensive conformational changes to certain Nups to allow for the passage of cargo. Unravelling how these NPC components might respond to transport factors is a key to understanding the NPC's role as a cellular regulator.

For the last 30 years, there have been suggestions that the NPC scaffold may exhibit plasticity in response to cargo. A diversity of shape and diameters of the pore structure have been observed with electron microscopy. Structural reorganization of the NPC "basket" proteins in response to ribonuclearprotein (RNP) granules suggests that this part of the pore can reorganize in response to cargos (Kiseleva et al., 1996). Additionally, the interior diameter of the pore has been measured to be larger when NPCs are engaged to large cargo such as the Balbini ring granules, pre-messenger RNP particles that contain the genetic information for secretory proteins and pass through the NPC in *Chironomus tentans* (Mehlin et al., 1991). When the 50-nm granule passes through the pore, it adapts an elongated

conformation, squeezing down to a diameter of 25-nm. The diameters of the pores observed in EM through which this cargo was passing through were observed to be larger than the other pores observed in the same sample (Mehlin et al., 1991). The permeability of the NPC to large cargos has been shown to be cell-cycle dependent, which implies that this permeability might be due differences in the diameter of the transport channel (Feldherr and Akin, 1990). Conformational variations of the inner channel ring were observed to have alternative inner diameters of either 10 nm or 26 nm and were implicated to change based on transport activity (Kiseleva et al., 1998). By applying cryo-ET to transport-competent, intact NPCs, distinct structures were obtained in the presence and absence of the central plug/transporter, suggesting that the addition of transport factors in the NPC led to structural rearrangements to the NPC scaffold (Beck et al., 2004). More recently, the revolution of cryo-electron tomography in conjunction with sub-tomogram averaging has allowed for the resolution of individual protein domains of the NPC (Eibauer et al., 2015). The NPC was isolated in both a transport-active and a transport-reduced state, and two distinct states emerged, with particular changes to the central transporter, suggesting that this region might undergo substantial conformational changes upon engagement of cargo (Eibauer et al., 2015; Zwerger et al., 2016).

Atomic Force Microscopy (AFM) has also been used to look at the dynamics of the NPC scaffold. Different conformations have been observed with different concentrations of calcium (Wang and Clapham, 1999). Chemically modifying the FG-FG interactions with *trans*-cyclohexane-1,2-diol has also been shown to modulate the diameter of the central channel of the NPC via AFM (Liashkovich et al.,

2011). More recently, high-resolution AFM has been used to visualize pores of different sizes and has revealed highly heterogenous lumens (Stanley et al., 2018).

Super resolution imaging has been used to visualize NPCs at different stages of development in *X. laevis* oocytes, demonstrating that the organization and diameter of the NPCs changes over time (Sellés et al., 2017).

Furthermore, recent structural studies, based on two discrete crystal states of short peptides of three inner channel ring Nups, Nup58, Nup54, and Nup62, has led to the proposal that the structured regions oscillate between a dilated ring of 40-50 nm in diameter and a constricted ring of 20 nm in diameter. The Ring Cycle hypothesis suggests that this ring undergoes conformational changes and directly regulates cargo import and export (Melčák et al., 2007; Solmaz et al., 2011, 2013).

Although it has been argued that massive diameter changes in the 30-nm range would buckle the membrane of the nuclear envelope (Liu et al., 2012), it has also been proposed that the evolution of the NPC into a complex sized over 120 MDa was in part driven by the need to cushion the huge diameter changes of the central transport channel by a large and deformable surrounding protein matrix (Hoelz et al., 2011).

Whether the scaffold and FG-Nups reorganize in response to transport events and kaps remains to be discovered. However, in addition to the compositional flexibility observed between NPCs from different species and from different cell types within humans, conformational flexibility has been observed within the scaffold. This conformational flexibility of scaffold components is separate from that observed in the intrinsically disordered regions of the FG-Nups.

1.7 Nups Imaged in This Study

In Chapters 4 and 5, I will describe my attempts to probe the NPC scaffold to determine if different rings of the NPC are subject to major conformational shifts. I will do this by placing fluorescent proteins in Nups localized to three different rings of the NPC, the Y-shaped complex (Nup133), the adaptor ring (Nup93), and the inner channel ring (Nup 54 and Nup58) (Figure 2). Below, I will provide an introduction to the current literature on the arrangement of each of these proteins within the NPC.

Nup133

Nup133 is a member of the Y-shaped complex. This complex is also referred to as the Nup84 complex in yeast and the Nup107 complex in humans (Siniossoglou et al., 1996; Walther et al., 2003). The Y-shaped complex is made of seven conserved members Nup96 (Nup145C in yeast), Nup160 (Nup120 in yeast), Nup133, Nup85 (also known as Nup75), Nup107, Sec13 homologue 1 (SEH1), and Sec13. In humans, there are three additional proteins, Nup43, Nup37, and ELYS. Each Y-shaped complex is iso-stochiometric, meaning that each Y-shaped complex has one version of each of the constituent proteins, except ELYS, which is only found on the nuclear facing rings. The fungal Y-shaped complex has been heavily analyzed through X-ray crystallography (Kelley et al., 2015; Stuwe et al., 2015) and cryo-EM (Kampmann and Blobel, 2009). Nup133 contains amphipathic motifs that allow it to bind to the nuclear envelope (Drin et al., 2007).

The Y-shaped complex is believed to form two reticulated rings at both the nuclear and cytoplasmic faces of the NPC and provide a site for functional transport

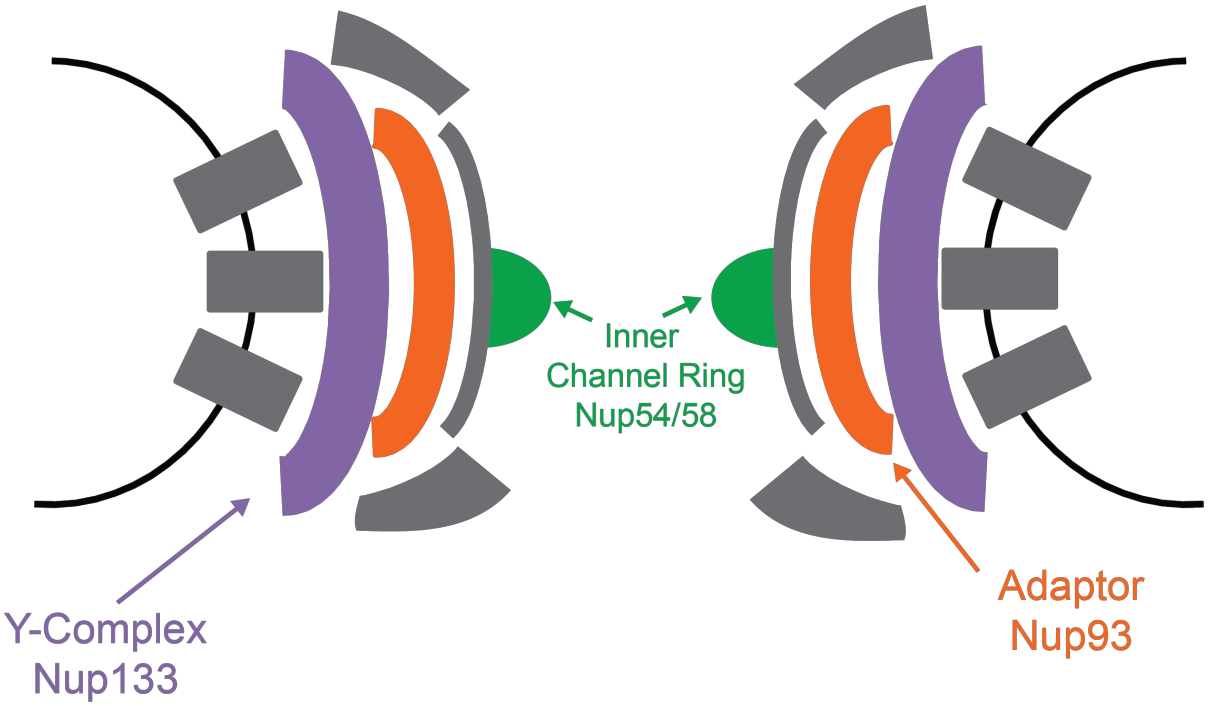

Figure 2. Location of the Nups Studied in this Thesis in the Mammalian NPC

The nuclear envelope is shown here as black; Nup133 is part of the y-complex which is localized to the coat scaffold Nups (purple); Nup93 localized to the adaptor scaffold Nups (orange); Nup54 and Nup58 are part of the inner channel ring (green).

Nups to associate (Bui et al., 2013). Using fluorescence-polarization microscopy, our group showed the Y-shaped complexes are aligned in a head-to-tail arrangement around the diameter of the ring (Kampmann et al., 2011). This result has been confirmed through tomographic mappings of the NPC that have allowed sufficient resolution to fit X-ray structures of the Nups to their locations in the NPC (von Appen et al., 2015; Bui et al., 2013; Eibauer et al., 2015; Kosinski et al., 2016).

Nup93

Nup93 is a member of the adaptor ring or inner ring complex (or Nup93 complex). The other members of this ring are Nup205 (Nup192 in yeast), Nup188, Nup155 (Nup170 and Nup157 in yeast), and Nup35 (Nup53 and Nup59 in yeast) (Beck and Hurt, 2016). Like the y-complex, this complex also forms 4 concentric rings. This ring sits inside of the y-complex, and Nup155 may serve as a connector between the inner Y-complex and this ring (von Appen et al., 2015).

Nup54/Nup58

Nup54 (Nup57 in yeast) and Nup58 (Nup49 in yeast) are members of the inner channel ring (or Nup62 complex) of the NPC along with Nup62 (Nsp1 in yeast) (Finlay et al., 1991; Guan et al., 1995; Kita et al., 1993). The adaptor ring complex (or Nup93 complex) forms a continuous contact with this ring (Beck and Hurt, 2016) and anchors it at the pore. Depletion of these proteins in Xenopus impairs NLS-driven trafficking (Finlay et al., 1991; Hülsmann et al., 2012). The arrangement and dynamics of this region of the NPC remains contested in the NPC field.

The Ring Cycle hypothesis suggests that this ring undergoes conformational changes in response to interactions with cargo and kaps to directly regulate cargo import and export (Melčák et al., 2007; Solmaz et al., 2011, 2013). Under this model, the Nup62-54-58 complex is able to reorganize and form an additional scaffold ring that restricts the passage of macromolecules but widens upon the binding of kaps. This model was built upon the structures of small coiled-coil fragments. A competing crystal structure of the human inner channel ring has been solved in which the intermediates necessitated by the ring cycle are prohibited (Chug et al., 2015). When the NPC was isolated in both a transport-active and a transport-reduced state, two separate states emerged via cryo-electron tomography in conjunction with sub-tomogram averaging, providing independent evidence that the inner channel ring experiences some structural rearrangement after disruption of cargo translocation (Eibauer et al., 2015; Zwerger et al., 2016), even though the mechanism and regulation have yet to be elucidated. I was therefore interested to see if I could visualize a rearrangement of this ring *in vivo* using polarized light microscopy.

1.8 Polarized Fluorescence Microscopy

The following section introduces concepts that are directly relevant to the work presented in Chapters 3 and 4.

Polarized fluorescence microscopy can be used to characterize the organization and dynamics of a protein or population of proteins with an orientationally constrained fluorescent tag (Atkinson et al., 2013; Burghardt, 1984; Corrie et al., 1999; Dale et al., 1999; Kampmann et al., 2011; Mattheyses et al., 2010). This technique has been used sporadically to characterize the behaviors of different proteins, but has remained an underdeveloped imaging tool.

The ratio of total mEGFP emission when illuminated with light parallel to its dipole over emission when illuminated with light perpendicular to its dipole is 30:1 (Inoué et al., 2002). Because mEGFP contains a short N-terminal alpha-helix, the mEGFP can be synthesized in frame to the protein of interest in a manner that constrains its excitation dipole. Therefore, mEGFP can serve as a reporter of protein orientation (Kampmann et al., 2011; Vrabioiu and Mitchison, 2006).

I have coupled polarization microscopy with total internal reflection fluorescence (TIRF) microscopy. TIRF is a super resolution technique that generates an excitation field that decays exponentially as it enters the sample, with a space constant approximately one-fifth to one-eighth the wavelength of the excitation light.

TIRF excitation serves to both increase axial resolution and improve spatial contrast by reducing excitation of out-of-focus fluorophores. When coupled with polarized-light, TIRF can be used to study molecular orientations and dynamics.

Polarized-TIRF (pol-TIRF) has been applied to study the plasma membrane structure (Johnson et al., 2014; Sund et al., 1999), exocytosis (Anantharam et al., 2010b, 2010a; Zenisek et al., 2002), vesicle fusion on a supported lipid bilayer (Kiessling et al., 2010), membrane lipid order (Oreopoulos and Yip, 2009; Oreopoulos et al., 2010; Thompson et al., 1984), as well as protein dynamics (Beausang et al., 2008) *in vitro*. Our lab has broadened this technique to use pol-TIRF to study the *in vivo* dynamics of proteins by looking at how the orientation of a key structural protein of HIV-1 changes during viral assembly (Johnson et al., 2019). In Chapter 3, I will describe how I have applied this technique to study the organization of the scaffold rings of the NPC.

CHAPTER 2: COARSE-GRAINED MODELLING OF FG-NUPS

The FG-Nups, which are the largely unstructured proteins that occupy the lumen of the NPC, are critical for NLS-mediated cargo translocation across the nuclear envelope. Transport through the pore is on the millisecond or tens of millisecond timescale, a timescale that is prohibitively long to reach through molecular dynamics simulations.

In this chapter, I will describe my how I used a coarse-grained computational model to simulate the dynamics of the FG-Nups. The goal was to have simulations that covered a sufficiently long period so that they could produce predictions that could be tested by experiment. There are two kinds of experimentally addressable measurements that are relevant to the dynamics of the NPC. First, we have measurements of the anisotropy of the FG-Nups at various locations along these lengths. These are fluorescence based measurements and thus the simulations would need to be at a minimum of milliseconds, preferably up to the second time scale. Second, there are measurements of both macroscopic transport rates and also transit rates for individual cargo, which are at the order of millisecond to tens of milliseconds. Again, it would be optimal to have the simulations extend to the time domain of seconds.

I will describe the formulation of this model, describe how the dynamics of the modeled FG-Nups corresponded to orientational measurements taken in our lab, and describe the behaviors of these FG-Nups over the time-course of our model.

2.1 Overview of the Coarse-Grained Model

To explore the dynamics of a full-cohort of Nups on the timescale of cargo translocation, I used coarse-grained computational simulations. My simulations generated predictions that can be experimentally tested to distinguish between proposed mechanisms of transport.

Because the architecture of the yeast NPC has been characterized with cryo-EM and X-ray crystallography of its parts, I used it to determine FG-Nup anchor site locations, filament lengths, FG repeat binding site positions, and densities of FG-Nups. The geometry and FG-Nup sequences used in our model are similar to the conditions by Tagliazucchi *et al.* (2013) in their coarse-grained simulation of the NPC. The transit rates for individual cargos have been reported to be on the order of milliseconds (Dange et al., 2008; Sun et al., 2008; Tu and Musser, 2011). The mesoscale model allows simulation times 10^2-10^3 longer than the transit rate. To ensure that the model behaved in a biologically relevant fashion, a single simulated filament was compared to published values of radius of gyration (R_g) and end-to-end measurements. The orientational autocorrelation functions of the FG-Nups were compared to the *in vivo* anisotropies of the FG-Nups previously measured in our lab.

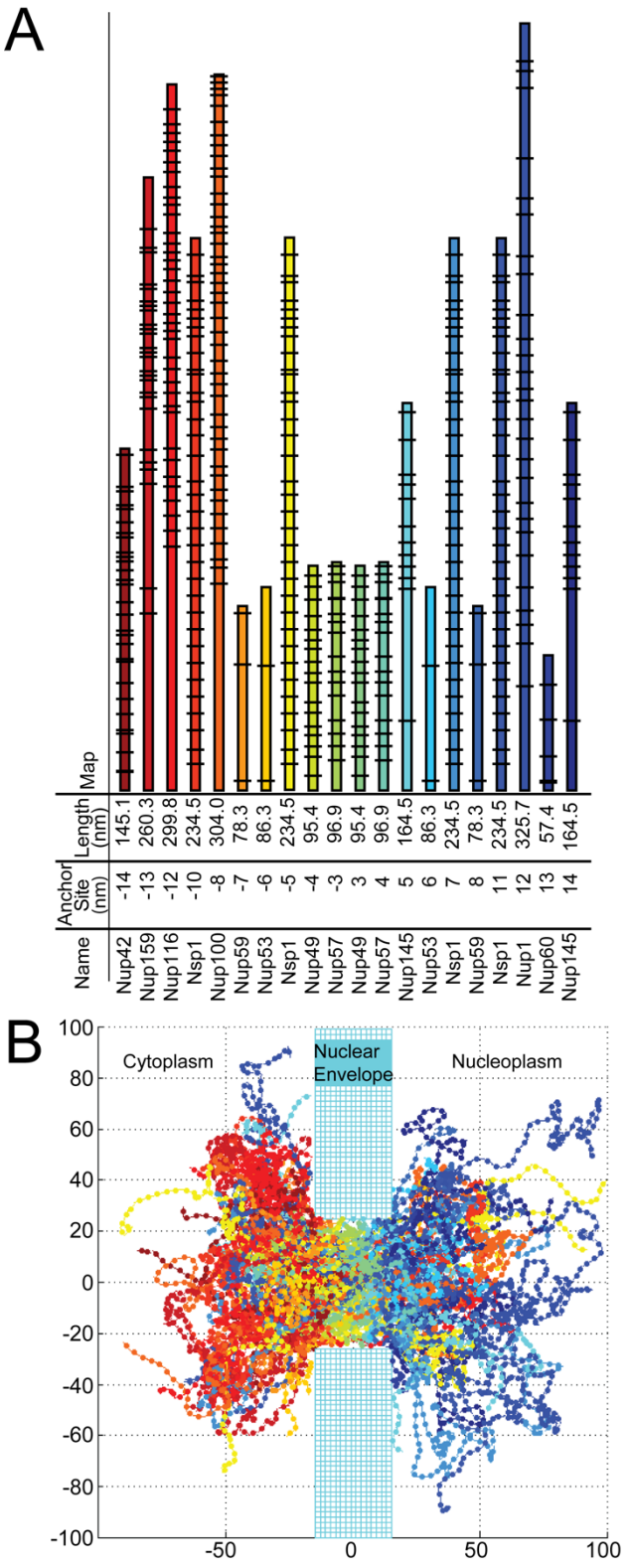

Figure 3. The Geometry of the Model NPC.

A) The anchor site of each NPC filament indicates the attachment position along the nucleo-cytoplasmic axis of each FG-Nup with the NPC geometry. The lengths of FG-Nups correspond to the size of the unstructured portions of the primary amino acid sequence. The black lines indicate FG-repeat locations. These FG-Nups are found in eightfold-symmetry, anchored around the scaffold of the NPC. B) Plotted snapshot of our simulation, all axes are in nanometers.

2.2 Model Construction

The model space was three-dimensional and encompassed a single cylindrical NPC, embedded in a wall representing the nuclear envelope and continuous on each side with hemispheres representing the nucleoplasm and cytoplasm in which filamentous FG-Nups and cargo can freely diffuse (Figure 3B). The NPC lumen is modeled as a cylinder of 30 nm in length and of 50 nm in inner diameter, dimensions approximately consistent with the size of the yeast NPC (Alber et al., 2007b). Twenty rings of FG-Nups anchored in 8-fold symmetry are located at the approximate *in vivo* positions experimentally determined (Alber et al., 2007b; Tagliazucchi et al., 2013). The length of each filament and the location of FG-repeat sites along its length are determined from the primary amino acid sequences of the predicted unfolded regions (Yamada et al., 2010) except for Nup53 and Nup59, which were defined by the largest continuous amino acid sequence containing the FG motifs FxFG, GLFG, FG, and FxF, separated by approximately 100 amino acids and including 10 amino acids at the terminus of the domain (Tagliazucchi et al., 2013; Yamada et al., 2010).

Each FG-Nup is modeled as a flexible filament anchored to the interior surface of the NPC cylinder. In this model, each FG-Nup is subdivided into the appropriate number of rigid cylindrical filaments segments of length 4 nm and radius 0.3 nm to reach the length based on the amino acid sequence (10.5 amino acids per cylindrical segment). The radius of 0.3 nm was chosen because the radius of an amino acid chain averaged over all amino acids is on the order of 0.3-0.4 nm (Counterman and Clemmer, 1999).

A coarse-grained Nsp1 filament composed of 4 nm segments recapitulates the end-to-end distances from molecular dynamics simulations for packed filaments. In Miao and Schulten (2009), the authors divided the 600 AA of Nsp1 into twenty-five 100 AA fragments and then tethered these segments onto a plane such that the tethered endpoints formed a 5 x 5 lattice. These filament segments collapsed into a brush structure, with a height of approximately 8 nm. Therefore, the expected end-to-end from these simulations of Nsp1 in a packed environment would be 48 nm (Miao and Schulten, 2010).

In our simulations, the filaments were allowed to interact at sites of FG groups. The "on" rate for these interactions was assume to be diffusion limited and the off-rate was varied over orders of magnitude from FG-FG off rate= 10^4/sec (referred to as FG4) to FG-FG off rate of 10^7/sec (FG7). By eliminating the original binding, it was treated as if there was an instantaneous off rate, which will be referred to as FG_{off}.

In our simulations, the radius of gyration (R_g) of a single tethered Nsp1 filament with the binding of FG_{off} is 21.2 nm (Radius of Hydration (R_H) = 16.9 nm) and the R_g of a tethered Nsp1 of FG4 binding is 19.3 nm (R_H = 15.5 nm). The end-to-end distance of our tethered Nsp1 filament is 49.7 nm in the absence of FG-FG binding (FG_{off}) and 43.5 nm in the presence of FG4 binding (FG-FG off rate of 10^4/sec). The R_g of a single untethered Nsp1 filament with FG_{off} binding is 21.1 nm (R_H = 16.8 nm) and the R_g of an untethered Nsp1 of FG4 binding is 19.9 nm (R_H = 16.0 nm). The end-to-end distance of our untethered Nsp1 filament is 50.0 nm in the absence of FG-FG binding and 47.1 nm in the presence of FG4 binding. These

values are in close agreement to the value of 48 nm from the molecular dynamics of Miao. These results differ from a coarse-grained single isolated filament simulation, where the end-to-end distances for NSP1 was 24 nm (Peyro et al., 2015b). However, I believe that our filaments behave most similarly to those in a confined volume. Miao and Schulten (2009) note that the array forms a brush-like structure with a height far larger (approximately 8 nm) than the R_g of a single chain, which they measure at 1.4 - 2.0 nm (for a 100 AA segment). Similarly, in a coarse-grained model of the NPC, the R_g of FG-Nups within the NPC was shown to be 3.9 to 6.5 times greater than R_g of isolated filaments (Ghavami et al., 2014). According to a MD simulation of full-length NSP1 the R_g is 6.5 nm (Ghavami et al., 2014), meaning that our measurement of ~20 nm is reasonable for an R_g of a packed FG-Nup.

In addition to being consistent with other modelling work, these results are consistent with previous experimental results from our own lab, where the FG-Nups anchored inside the NPC exhibited a higher effective persistence length than the FG-Nups artificially anchored to the plasma membrane, which demonstrated very high flexibility, suggesting that polymer dynamics are strongly influenced by the local environment (Atkinson et al., 2013).

2.2 Modulating FG-FG Interactions Creates Different Diffusive Barriers

In the simulations the density and distribution of both the FG-Nup filament segments and the FG-repeat sites were studied as a function of FG-FG binding by varying the FG-FG off rate over several orders of magnitude. The fraction of FG-repeat sites occupied was determined for the various binding conditions of the simulation (Figure 4A). At the strongest FG binding condition probed, FG4, about a third of the FG-FG binding sites were occupied with FG-FG bonds. In a much weaker binding condition, FG7, only a maximum of 0.3% of binding sites were occupied at any one time. These disassociation rates remained constant over the total simulation time, which was a hundred milliseconds. The density of FG-Nups within the NPC lumen decreased with binding strengths weaker than FG4 (Figure 6F). The FG-FG bond strength also affected the packing of filaments. I measured packing as the distance from the center of the pore along the axis within which 75% of filament mass was contained (Figure 4B). In the FG4 condition, the mass of filaments was closer within the NPC channel (Figure 4B). With weaker bonds, the FG-Nups extended farther outside of the lumen of the NPC into the cytoplasm and nucleoplasm. On average, 75% of the filament mass was within 44 ± 1 nm (FG4) or 52 ± 2 nm (FG7) of the center of the NPC.

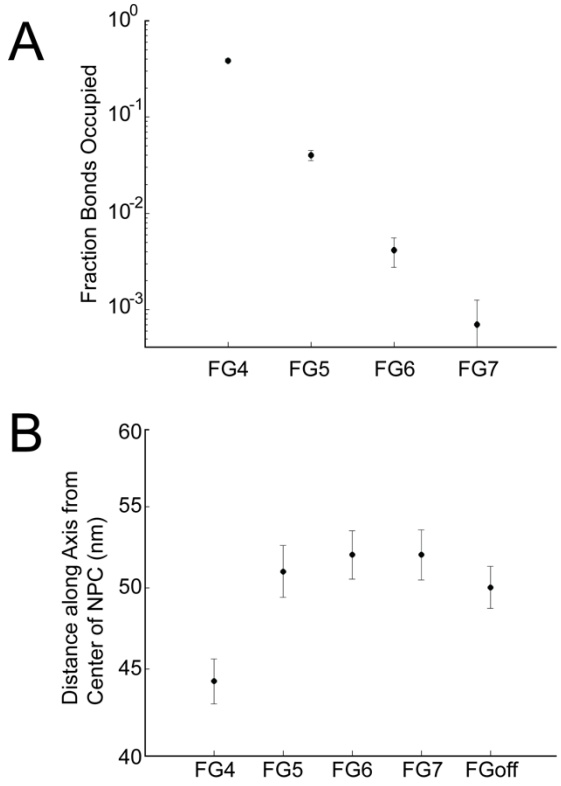

Figure 4. Modulating FG-FG Binding Strength Changes Arrangement of FG-Nups.

A) The fraction of FG-binding sites occupied at a given time step. B) Distance from the center of the NPC lumen that 75% of filament mass is located within. (All plots are mean ± S. D.)

2.2 Simulated FG-Nups Experience Similar Orientational Freedoms as *In Vivo* FG-Nups

As an experimental test of the predictions of our simulations, I probed if the orientation freedom predicted from the simulations matches the experimental observations of anisotropy of the filaments. Our lab had previously measured anisotropy at the base and tip of Nup57 and the base, middle, and tip for Nup116 and Nup159 using fluorescently labelled FG-Nups. Anisotropy is a measurement of the orientational freedom of molecules that can be related to the orientational autocorrelation function. This relationship between these measurements is formalized by the Perrin equation:

$$\frac{r_0}{r} = 1 + {}^{\tau}/_{\Theta},$$

where τ is the fluorescence lifespan, θ is the rotational correlation time, r is the measured anisotropy and r_0 is the fundamental anisotropy (the anisotropy of the probe in a fixed position). Faster decay of autocorrelation functions correlates with a lower measured anisotropy value and longer decay of autocorrelation functions correlates to a higher measured anisotropy value.

To test if the simulations of the FG-Nup filaments in this model quantitatively recapitulated experimental measurements, the autocorrelation functions of Nup116, Nup57, and Nup159 were calculated and averaged across four iterations of a given simulation (Figure 5). Members of our lab previously measured the anisotropy of these Nups in their native context inside the NPC. This approach was taken because we found that Nups in the NPC showed altered anisotropy when we changed their

location in the NPC. Moreover, we saw that these Nups exhibited much lower anisotropy when they were expressed elsewhere in the cell, outside of the packing of the NPC (Atkinson et al., 2013). We evaluated their orientation and dynamics by inserting fluorescent probes at several points along the unstructured domain of the FG-Nups and measuring the fluorescence anisotropy at the different positions (Atkinson et al., 2013; Kampmann et al., 2011; Mattheyses et al., 2010). Fluorescence anisotropy experiments are performed by exciting fluorophores with a given linear polarization of light. By measuring the light emitted parallel to the excitation and the light emitted perpendicular to the excitation, one can calculate a fluorophore's anisotropy, or its orientational freedom.

For both Nup116 (299.8 nm) and Nup159 (260.3 nm), probes placed at the base, middle, and tip of the FG-region yielded a clear difference in measured anisotropy, with the most flexibility observed at the tip, an intermediate flexibility observed at the middle, and a low flexibility observed at the base. For Nup57 (96.9 nm), probes placed at the tip and the base did not yield a clear difference, with a only a slightly more flexibility observed at the tip than the base. Therefore, anisotropy of Nup57 did not decrease to the same extent as Nup159 and Nup116.

The anisotropies of these FG-Nups were also measured in their mammalian cell homologues, and the same behaviors were conserved and amplified between the species. In the mammalian system, the signal to noise of the system was improved by the reduction in nucleus curvature. With this improved signal, the mammalian homologue to Nup57, Nup54, did not exhibit an increase in flexibility along its length. In mammalian cells, the anisotropy measurements of these FG-

Nups measurements were taken both in the presence and the absence of karyopherins (kaps) which were removed in a digitonin permeabilized system. No difference in anisotropy measurements were measured upon the removal of kaps (Atkinson et al., 2013). This measured anisotropy is directly related to the rotational correlation time.

To compare these experimental results to our coarse-grained model I needed a method to measure the orientational flexibility of the simulated FG-Nups. I calculated the autocorrelation function, a measure of orientational self-correlation, which can be calculated for a single filament segment over the time course of the entire experiment as follows:

$$f(k) = \frac{1}{(n-k)} \cdot \sum_{t=1}^{n-k} (\bar{u}_t) \cdot (\bar{u}_{t+k}) \ ,$$

where *k* represents the difference in time, n represents the total number of data points, and $\bar{u}_t$ represents the orientation unit vector at time *t*. In an ideal case, this autocorrelation is expected to approximate a single exponential decay, the half-life of which should be directly correlated to the decay of anisotropy that a fluorescent probe placed along the filament length should experience. Therefore, a faster decay in the autocorrelation function is equivalent to a lower anisotropy and a longer decay in the autocorrelation function is equivalent to a higher anisotropy.

In the case of FG_{off} simulations, for all FG-Nups (no interactions between the filaments), the orientational freedom was lowest near where the filament was anchored and increased toward the tip of the filament (Figure 5). This increase in

orientational freedom was evident because near the tip the autocorrelation curve decayed faster and its asymptote was lower. Nup116 and Nup159 exhibited this trend regardless of the strength of the FG bonds. In contrast, Nup57 behaved differently from the others: when FG-FG bonding was allowed, no difference in the orientational rigidity along its length was observed. Each of these observations was consistent with our previously described experimental results.

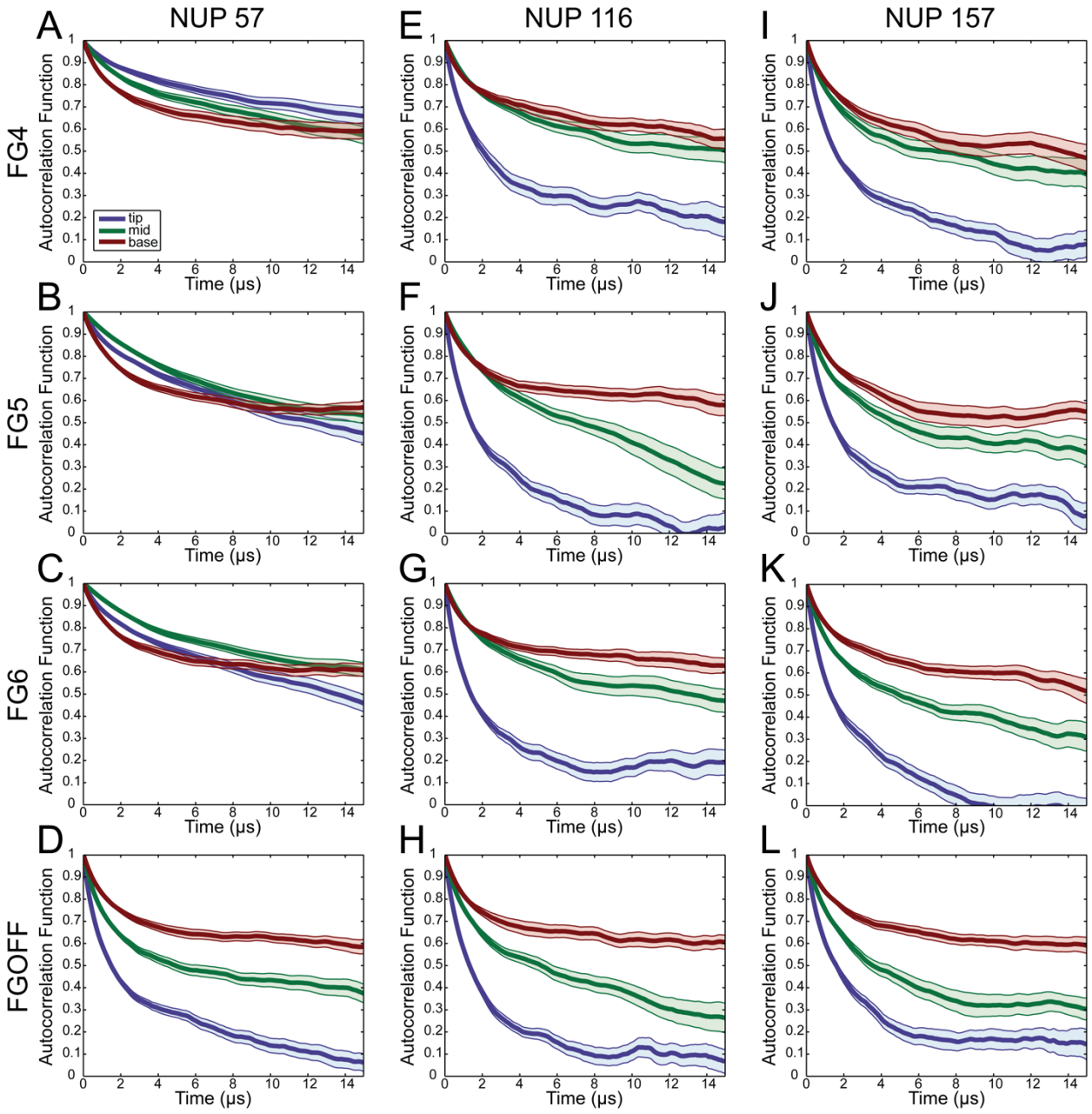

Figure 5. The Orientational Rigidity of FG-Nups Exhibit Differential Dependence on FG-FG Bond Strength.

Autocorrelation plots of filaments, taken at three locations along filament length, base, middle, and tip. A-D) FG-Nup116, E-H) FG-Nup57 I-L) FG-Nup159, each at four different FG-FG off rates (FG4, FG5, FG6, and FGoff). Plotted lines represent mean of autocorrelation functions ± S.E. Blue = tip segment, green = middle segment, red = base segment.

2.3 Distribution of FG-Nups in the Lumen of the NPC

The density profiles of FG-Nups within a 4 nm transverse slice through the center of the pore (Figure 6) were calculated. The greatest density of filaments was located along the periphery of the NPC lumen, and density decreased moving radially towards the center of the NPC, resulting in a central channel of decreased density. This central channel was more prominent with FG-FG bonds of a lower stability. These results are consistent with the simulations by Tagliazucchi *et al*., using static potential of mean force calculations. The bulk of the simulated FG-Nups explore a region outside of the lumen of the pore due to the volume of the open space on either side of the NPC similar to the simulations of Tagliazucchi *et al*. Increased stability of FG-FG binding increases the crosslinking of filaments within the pore, decreasing the prominence of this central channel. Interestingly, I did not observe the well-defined “doughnut-like” region of FG-Nups that was observed in the simulations of Ghavami et al. (2014). This could be attributed to differences in anchor locations between the two simulations and the lack of charged residues in our simulation that they argue pushes the FG-Nup mass towards the center of the NPC channel.

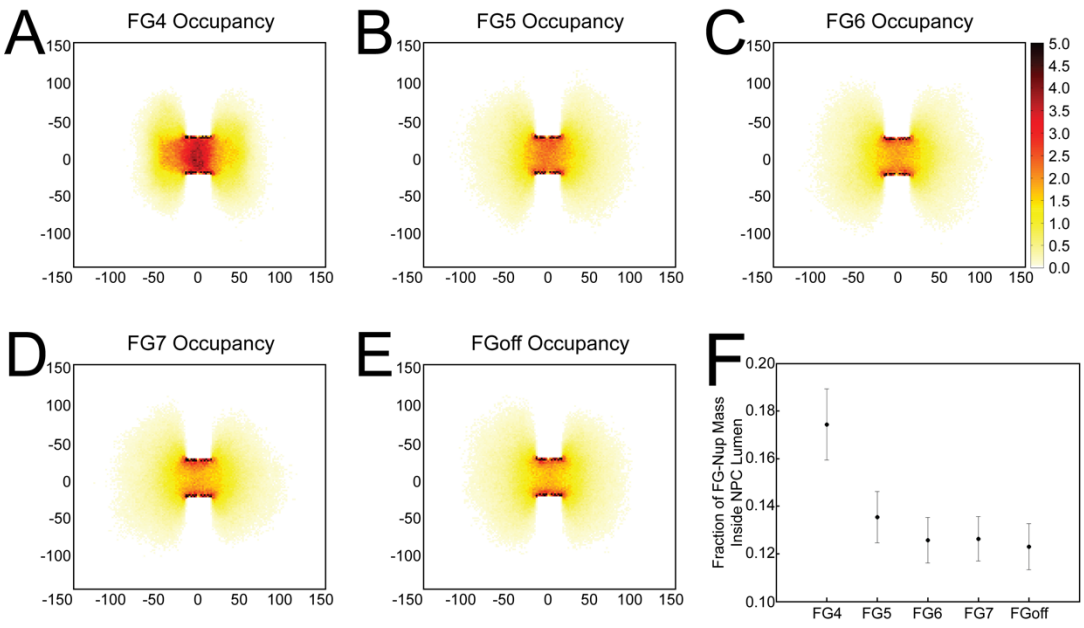

Figure 6. FG-Nup Packing Creates Channel in the Center of the Lumen.

2-Dimensional histogram of filament locations normalized over a 100ms simulation in a 4 nm slice through the center of the NPC under: A) FG4 bond strength. B) FG5 bond strength. C) FG6 bond strength. D) FG7 bond strength. E) No FG Bonds. The scale goes from 0 to 5 and indicates the average number of filaments in that spot over the time course of the simulation. F) The fraction of filament mass that is located within the lumen of the NPC. Plot is mean ± S. D.

2.4 FG-FG Bonds Occupy the Lumen of the NPC

In each of the FG binding conditions, the majority of the FG-FG bonds are within the lumen of the NPC. In FG4, around 650 bonds populate the lumen of the NPC. These bonds increase FG-Nup mass within the lumen and thereby reduce the prevalence of the central channel discussed above. In weaker binding conditions, not only is the number of bonds reduced, but also their localization to the lumen of the NPC is reduced, resulting in a more prominent central channel of decreased FG-Nup density.

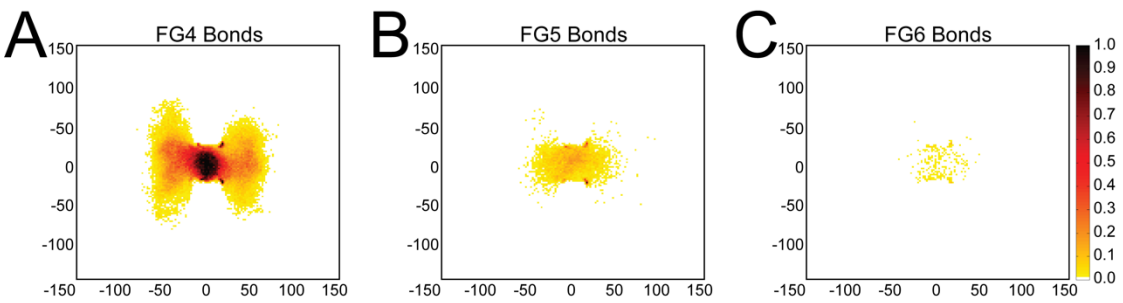

Figure 7. FG-FG Bonds Are Most Concentrated in Interior of NPC.

2-Dimensional histogram of FG-FG bonds normalized over a 100ms simulation in a 4 nm slice through the center of the NPC under: A) FG4 bond strength. B) FG5 bond strength. C) FG6 bond strength. The scale goes from 0 to 1 and indicates the probability of an FG-FG bond existing in that spot at any given time point in the simulation.

2.5 Nematic Order inside the NPC Decreases with Stronger FG-FG Interactions

Previously, behavior resembling a liquid crystal was observed for FG-Nups in the *in vivo* NPC (Atkinson et al., 2013). The FG-Nups showed a higher degree of anisotropy, or orientational order within the pore, similar to the orientational order of fatty acid tails in a lipid membrane. This order was affected by the location of each FG-Nup within the NPC and was significantly reduced when the FG-Nups were outside the lumen of the NPC. The anisotropy, or orientational order was highest near the base of the FG-Nups and decreased towards the tips of the filaments. These observations are consistent with the FG-Nups in the interior of the pore acting in an orientationally ordered manner, i.e. aligning along the nuclear-cytoplasmic axis.

The nematic order parameter is used to characterize the orientational order in liquid crystals. It is calculated by taking the largest positive eigenvalue from a second order orientational descriptor, *Q* (Eppenga and Frenkel, 2006).

Q takes the form of a three-by-three second order tensor, where each element, $Q_{\alpha\beta}$, is defined as follows by α and β, which represent *x*, *y*, and *z*:

$$Q_{\alpha\beta} = \frac{1}{2\times N}\left(\left(3 \times \sum_i \bar{u}_{i\alpha} \times \bar{u}_{i\beta}\right) - \delta_{\alpha\beta}\right),$$

where *N* represents the number of segments, $\bar{u}_{i\alpha}$ is the α component of the orientation unit vector of the ith segment, and $\delta_{\alpha\beta}$ is the Kronecker delta function. The nematic order parameter is always between 0 and 1, with 1 indicating the maximal order and 0 indicating complete disorder.

The nematic order parameter was calculated for the FG-Nups. The first five segments along a filament were not included in calculations to avoid the effects of

the anchoring domains. In the lumen of the NPC, the nematic order parameter was inversely proportional to the FG-FG bond strength: the stronger the binding, the weaker the orientational order (Figure 8A). In the case of high FG-FG bond strength, many bonds were formed, as discussed above, effectively packing FG-Nups into the lumen. This held them in a denser meshwork that was only loosely organized according to orientation. At weaker FG-FG bond strengths, the filaments were not as restrained with the pore by FG interactions. Instead, the filaments were relaxed into a liquid-crystal-like state, with higher nematic order organization along the nuclear-cytoplasmic axis.

Across all FG-FG binding conditions, the nematic order parameter for the filaments was greater within the NPC lumen relative to outside (Figure 8A). When the nematic order parameter was calculated over the entire lumen of the pore, the nematic order was substantially different for conditions of high binding, FG4 with a nematic order of 0.060 ± 0.004 and conditions with very low binding, FG7 with a nematic order of 0.17 ± 0.02. Interestingly, the nematic order was higher for FG7 than for FG_{off}, which may indicate that a certain amount of FG-FG binding may contribute to order within the NPC. For each binding condition, the nematic order was significantly higher inside the lumen as compared with both the cytoplasm and nucleoplasm. This is consistent with it being an indication of the packing of the filaments.

When the nematic order parameter was calculated in 5 nm increments along the nuclear-cytoplasmic axis, higher values were obtained than the values for the entire lumen because of increased local order. For FG4, the nematic order within the

NPC ranged from 0.090 ± 0.002 to 0.115 ± 0.004 and for FG7, the nematic order within the NPC ranged from 0.16 ± 0.01 to 0.24 ± 0.01 (Figure 8B). Interestingly, for each binding strength, the highest order within the NPC lumen occurred near the peripheries near the cytoplasm and the nucleoplasm, with a local minima in the center of the NPC.

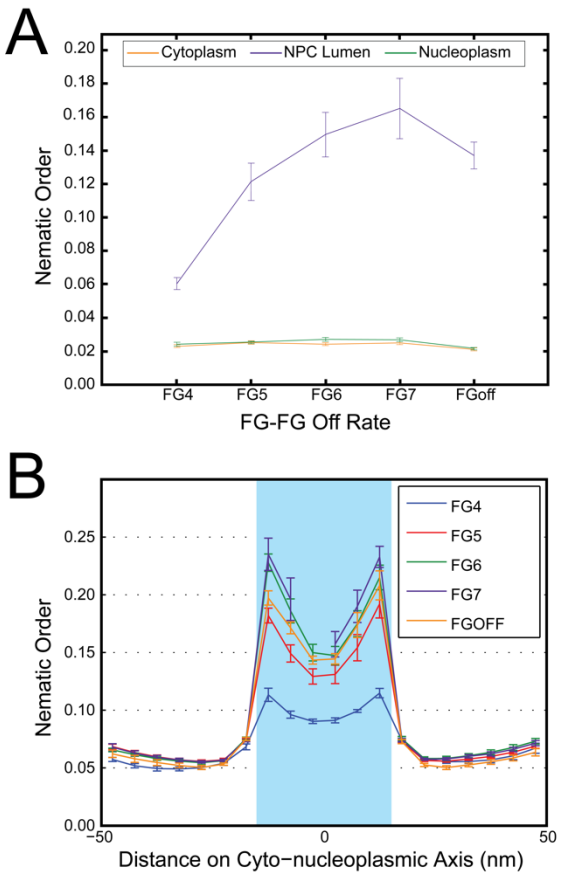

Figure 8. Nematic Orders are Highest in Lumen of NPC.

A) Nematic order parameters calculated inside and outside of the NPC lumen, averaged over four data sets of 100ms. With decreasing FG-Nup binding strength, increased nematic order within the NPC is observed. B) Nematic order parameters calculated across the nuclear cytoplasmic axis, x-axis is in nanometers, the nematic order parameters are averaged over four data sets of 100ms. (All plots are mean ± S. D.)

2.6 FG-Nup Filaments Translocate the NPC

In all of the simulations, FG-Nup filaments translocate the NPC moving between the cytoplasmic and nuclear domains (Figure 9A). Almost half of the FG-Nup filaments that started outside of the lumen of the NPC on the cytoplasmic side reached the nucleoplasm within the course of a 100 ms simulation time (Figure 9A). For FG4, 38.5% of filaments initially in the cytoplasm reached the inside of the nucleus during the course of the simulation. For FG5-7 and FG_{off}, the translocation fraction was higher (Figure 9B).

Translocation time was measured as the time elapsed from the last moment at which the filament was located outside the lumen of the NPC on one side (nuclear or cytoplasmic +/- 15 nm) to the first time point the filament was located outside the lumen of the NPC on the opposite side (cytoplasmic or nuclear -/+ 15 nm). The mean translocation time was shorter with faster FG-FG off rates. For FG4, the translocation time was 2.2 ms ± 1.8 ms. Without FG-FG bonding, the mean translocation time was 0.27 ± 0.13 ms. To confirm that the translocations were not an artifact of our segment length, I simulated shorter sized filament segments and observed translocations at indistinguishable timescales for FG_{off} (Figure 9D).

Therefore, the FG-Nups in the simulation reptated back and forth through the NPC at time-scales commensurate with the experimental measurements of the speed of cargo transport through the NPC. These results are consistent with models of transport where FG-Nup filaments are free to move across the central channel of the NPC, informing how cargo might transverse the NPC.

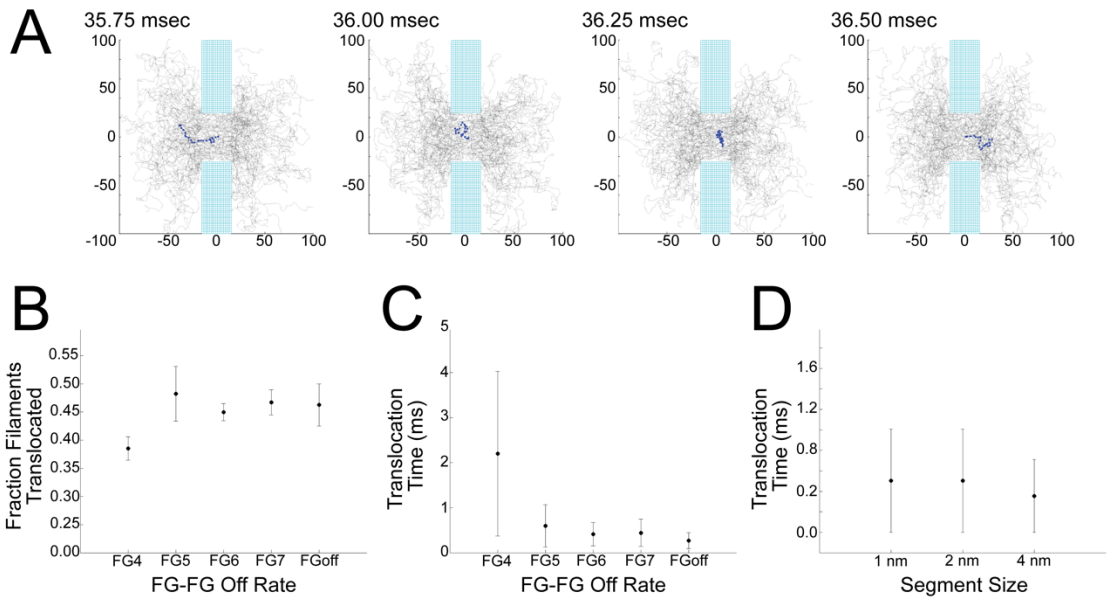

Figure 9. Filaments Translocate the Nuclear Envelope.

A) Translocation event of a single FG-Nup49 filament under no FG-bonding condition, all axes are in nanometers. B) For all binding conditions, the fraction that translocate is defined as the fraction of filaments that started the simulation on the cytoplasmic side of the NPC and eventually made it into the nucleus. C) Time to translocate is defined as the time elapsed between entering the NPC on one side and emergence on the opposite side, in either direction. D) Time to translocate for filaments composed of segments of different sizes. (All plots are mean ± S. D.)

2.7 Inner Ring FG-Nup Filaments Translocate the NPC Most Frequently with Low Binding Affinity

The number of translocation events per unit time increased with increasing off rates for FG-FG bonds, with the highest rate occurring in the absence of FG-FG bonding. Much of this increase was due to the greater frequency of translocations of Nup57 and Nup49, two relatively short centrally located FG-Nups that contain many FG-repeats (Figure 10).

In addition to recapitulating the orientational behavior of FG-Nups *in vivo*, this model yielded the testable prediction that individual FG-Nups are able to traslocate through the NPC on time scales commensurate with cargo translocation. This result is consistent with models of transport where FG-Nups are free to move across the central channel of the NPC and remains to be tested in future experiments.

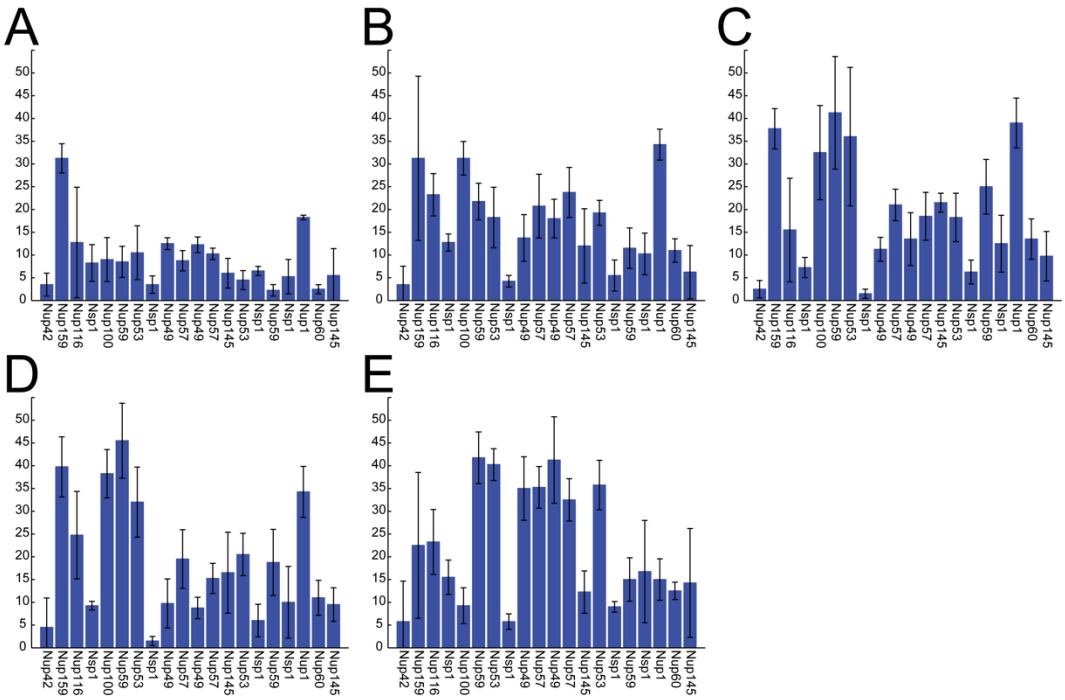

Figure 10. The Number of Translocations per Ring Increases with Increased FG-FG Off Rate.

A-E) Number of translocations per ring of 8 FG-Nups, averaged over four data sets of 100ms. (All plots are mean ± S. D.) A) FG4 bond strength. B) FG5 bond strength. C) FG6 bond strength. D) FG7 bond strength. E) FGoff bond strength.

CHAPTER 3: FLUORESCENCE POLARIZATION IMAGING OF THE NPC

Polarized fluorescence microscopy can yield information about the orientation and dynamics of proteins within living cells. By fluorescently tagging Nups and imaging them with polarized-TIRF (pol-TIRF) microscopy, I have been able to measure not only the orientations and dynamics of different Nups, but also the dynamics of different domains within the same Nup.

In this chapter, I will describe the polarized-TIRF set-up that I used to measure Nup orientations and dynamics *in vivo*. I will also describe the automated algorithms to quantify these measurements that I built, tested, and validated.

I have placed mEGFP sensors in multiple positions of four different Nups: Nup133, Nup93, Nup54, and Nup58. These Nups are localized to the Y-shaped complex (Nup133), the adaptor ring (Nup93), and the inner channel ring of the NPC (Nup54 and Nup58). I will describe how I have validated these Nup-mEGFP orientational sensors to confirm that they are reporting on the orientations of the Nups of interest.

Furthermore, I will describe how I created five CRISPR cell lines where I replaced both endogenous copies of Nup133 or Nup54 with the fusion protein sensor equivalents. I will describe how these CRISPR cell lines compare to the transient transfections of the equivalent fusion protein sensors.

The tools developed in this chapter will be applied in Chapter 5 to test NPC dynamics under different physiological conditions.

3.1 Microscope Construction

The basal surface of the nucleus was illuminated using TIRF with the capability to control the polarization of the excitation light (pol-TIRF). This technique allows the fluorophores to be excited using either *p*-polarized (perpendicular to the coverslip) or *s*-polarized (parallel to the coverslip) light. The nucleocytoplasmic axis of each NPC is perpendicular to the plane of the nuclear envelope NE which is, for the Nup along the bottom surface of the nucleus, parallel to the coverslip (Figure 11A-D). Therefore, the *p*-polarized light is parallel to the nucleocytoplasmic axis of each NPC and the *s*-polarized light is perpendicular to the nucleocytoplasmic axis of each NPC. Many commonly used cultured cell lines, including HeLa, U2OS, and Cos7, hold their nuclear envelopes low to the coverslip, allowing for the parallel measurement of many NPCs within a single cell. As will be shown below, the variability in the ease of exciting the NPC with *p* or *s* polarization does not detectably vary across the bottom surface of the nucleus, indicating the NPCs have a shared orientation.

The fluorescently-conjugated Nups were imaged with both *p*-polarized and *s*-polarized light (Figure 11C-D). Images were collected on an inverted microscope (IX-81, Olympus) with a custom built through-the-objective (100X UAPON 1.49 NA, Olympus) polarized TIRFM illuminator (Johnson et al., 2014). In order to reduce spatial nonuniformities caused by the diffraction of excitation light within the system, the excitation TIR light was azimuthally scanned at 200 Hz with mirror galvanometers (Nutfield Technology). All emission light was collected after it was

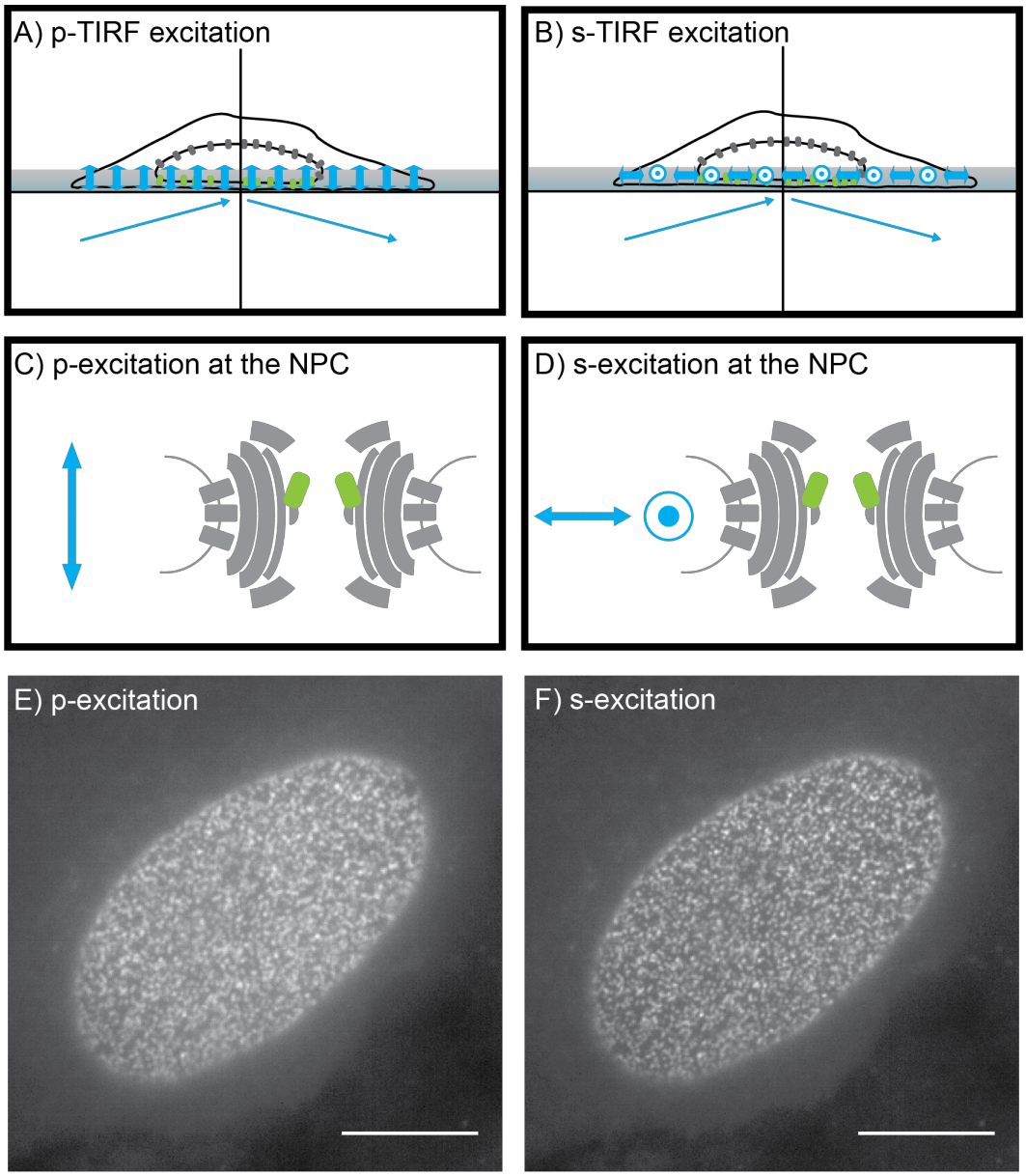

Figure 11. Individual NPCs can be Resolved with pol-TIRF.

A-B) Using pol-TIRF, the bottom of the nucleus is illuminated and Nup-mEGFP fusion proteins are selectively excited using *p*-polarized light (perpendicular to coverslip) or *s*-polarized light (parallel to coverslip). C-D) *p*-excitation and *s*-excitation at the NPC in TIRF microscopy. E-F) Nup54-mEGFP fusion proteins in HeLa cells 24 hours post transfection imaged with polarized-TIRF. Each punctum is a NPC. (*Scale bar = 10 µm).*

passed through a multiband polychroic (zt405/488/594/647rpc 2mm substrate, Chroma) to isolate the excitation light from the emitted light.

For each excitation of the sample, the galvanometers completed one full azimuthal scan. This scan reduced the diffractive interference patterns by averaging them. If linearly polarized light were simply rotated around the back-focal plane, then the polarization of light relative to the axis of the object will continuously change. Light that enters the back focal plane at one point to produce *p*-polarization at the coverslip, would, after a rotation of $\pi/2$ in the back-focal plane, produce *s*-polarization at the cover slip. Thus, I used an electrooptic modifier (EOM, Conoptics, Danbury, CT) and a quarter-wave-plate (Thorlabs) before the galvanometers to control the polarization of the 488 nm laser (100 mW LuxX diode laser, Omicron, Rodgau-Dudenhofen, Germany). The polarization of the EOM was modulated such that the polarization of the excitation light was spun in sync with the azimuthal scan of the galvanometers and either *p* or *s* was maintained in the sample throughout the azimuthal scan.

Images were collected on a CMOS camera (Flash-4.0, Hamamatsu, Hamamatsu City, Japan) connected with a Hamamatsu Camera Link interface to a workstation (Precision Model T7500, Dell, Round Rock, TX) running image acquisition software (Metamorph). A sequence of 20 images was taken, alternating between p and s with each acquisition and yielding 10 *p* and 10 *s* images. Each individual *p* or *s* image had an exposure time of 5 ms (laser power was 100 mW), and a new image was collected every 15 ms. The polarization images were captured in this interleaved manner in order to minimize artifacts that may have been created

by having an exposure time longer than experimentally detectable fluctuations. The galvanometers, EOM, camera shutter, and 488 laser shutters were all driven by a multifunctional data acquisition board (PCIe-6323, 577 National Instruments) and controlled from custom written software in LabView (Johnson et al., 2014).

3.2 Computational Analysis: Orientation Measurements

All image analysis was automated with analysis algorithms written in MATLAB (Figure 12, also Methods, page 174). For static measurements, twenty sequentially acquired images, 10 *p* and 10 *s,* were summed to form a single *p* and a single *s* image for each time point. Camera background was subtracted from each image, then NPCs were identified via an automated algorithm. The fluorescence of each NPC was fit to a Gaussian and if the Gaussian fit could not be performed then the data point was rejected as poor quality. The intensities from the original (non-background subtracted) image were then extracted for analysis by taking the intensity from the maximum intensity pixel from each punctum. A ratio was then calculated for each time point. Using this algorithm, initial *p/s* ratios were obtained for experimental condition and measurements of the changes of the ratio of *p/s* over time could be obtained for many NPCs within the same cell.

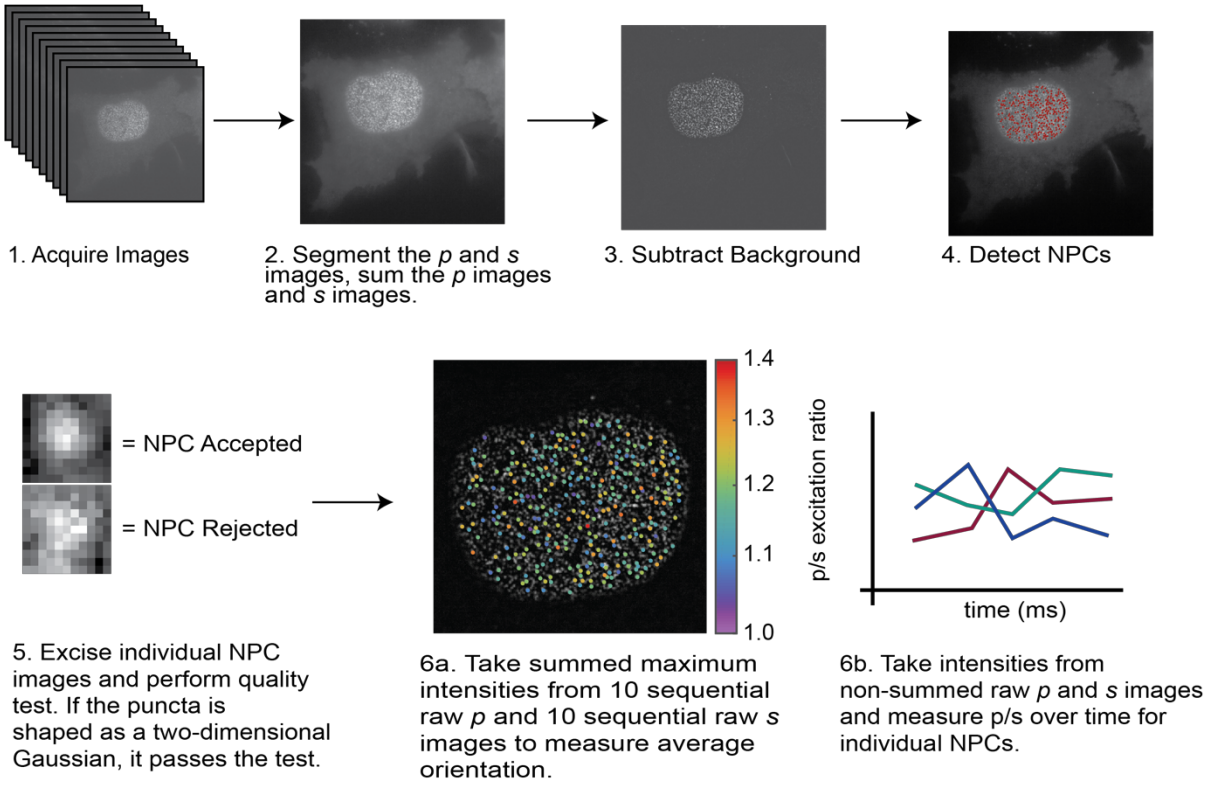

Figure 12. Schematic of Automated Data Processing Algorithm

Schematic of Automated Algorithm to Detect NPCs and calculate both average *p/s* orientation measurements and *p/s* orientation measurements over time.

3.3 The *P/S* Ratios of Nup-mEGFP Sensors Report on Nup Orientation *in vivo*

Plasmids were engineered to encode a Nup (Nup133, Nup93, Nup54, or Nup58) expressed as a fusion to mEGFP via an alpha-helix. mEGFP contains a short N-terminal alpha-helix, which was synthesized in frame to the proteins of interest. We have previously shown that this approach can restrict the excitation dipole of mEGFP and allow this mEGFP to provide a read out of orientation (Kampmann et al., 2011; Vrabioiu and Mitchison, 2006). The ratio of mEGFP emission when illuminated with light parallel to its dipole over emission when illuminated with light perpendicular to its dipole is 30:1 (Inoué et al., 2002), enabling mEGFP to serve as a read out of protein orientation when rigidly conjugated to our Nups of interest. Each of these fusion proteins will be tested and, if validated, I will refer to them as conformational sensors.

As described in Chapter 1, Nup54 and Nup58 sit in the inner channel ring of the NPC and have been implicated in a potential conformational shift that would result in a diameter shift of the NPC (Melčák et al., 2007; Solmaz et al., 2013). Furthermore, this area undergoes a structural change in NPCs in a depleted transport state (Eibauer et al., 2015). Nup93 sits in the adaptor ring of the NPC and Nup133 sits in the Y-shaped complex. Although there is little evidence to suggest that these scaffold Nups undergo any orientational changes in response to cargo, these NPC scaffold proteins in yeast might allow local rearrangements to permit the hydrophilic domains of inner nuclear membrane proteins to translocate the NPC (King et al., 2006).

With both *p*-polarized and *s*-polarized TIRF illumination, I was able to image these fusion proteins in individual NPCs after transient transfection in HeLa cells (Figure 13). I measured the light emitted from each individual NPC under the two different polarization excitations. By comparing the ratio of light emitted in response to perpendicular (*p*) excitation and parallel (*s*) excitation, I calculated what I will refer to as the *p/s* ratio. If the mEGFP is rigidly conjugated to a protein that is appropriately integrated into the NPC, this *p/s* ratio is equivalent to a measurement of the orientation of that protein.

Figure 13. Nup-mEGFP Fusion Proteins can be Imaged with Polarized Light

The *p/s* ratio of individual NPCs was calculated and then mapped to the location of the NPC on the image of the Nup-mEGFP fusion proteins with a color corresponding to the *p/s* ratio. A) Nup133-mEGFP with the mEGFP at the carboxyl-terminus of the protein. B) Nup93-mEGFP with the mEGFP at the carboxyl-terminus of the protein. C) Nup54-mEGFP with the mEGFP at the carboxyl-terminus of the protein. D) Nup58-mEGFP with the mEGFP at the carboxyl-terminus of the protein. (*Scale bar = 10 µm).*

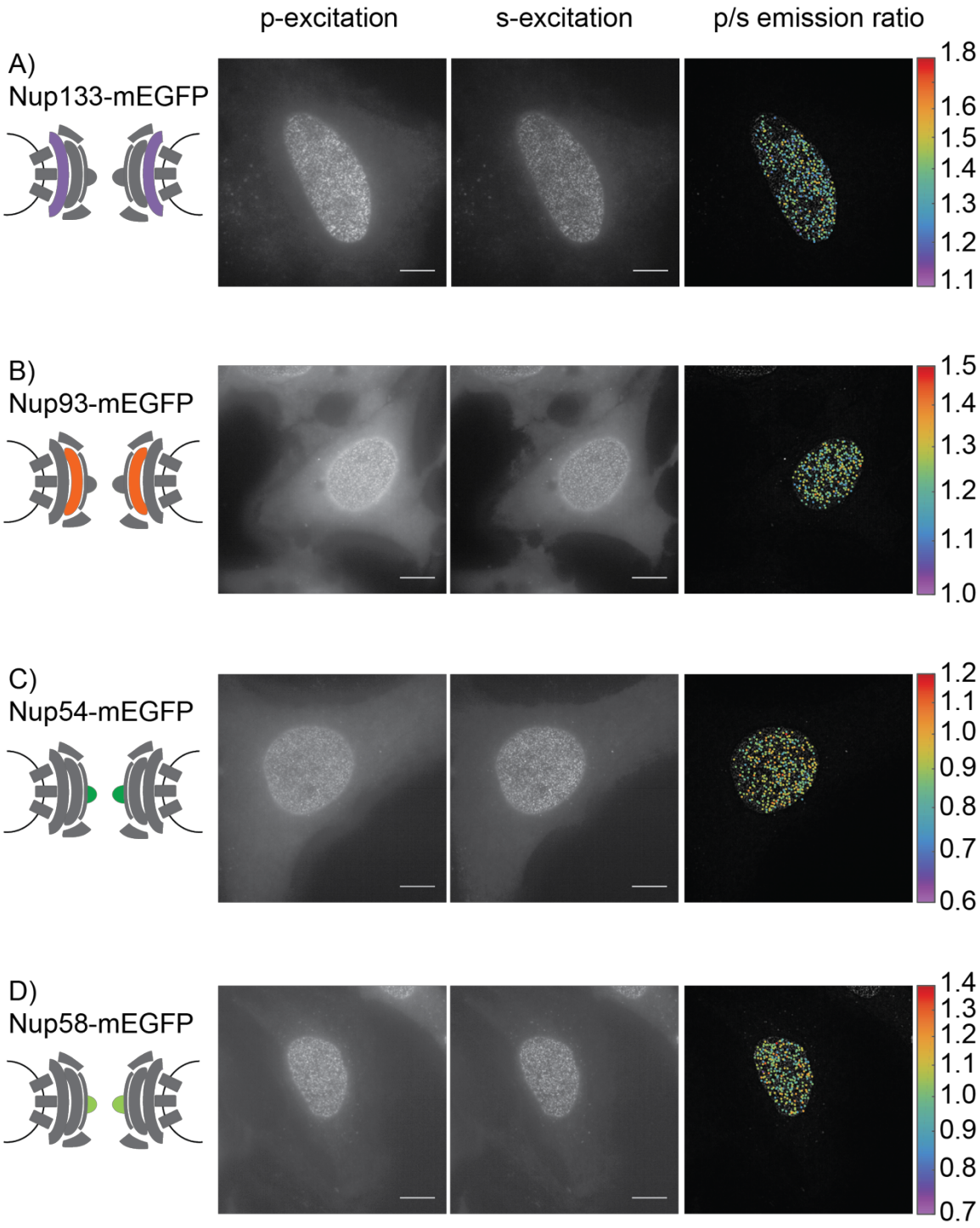
p-excitation
s-excitation
p/s emission ratio
A)
Nup133-mEGFP
1.8
1.6
1.5
1.4
1.3
1.2
1.1
B)
Nup93-mEGFP
1.5
1.4
1.3
1.2
1.1
1.0
C)
Nup54-mEGFP
1.2
1.1
1.0
0.9
0.8
0.7
0.6
D)
Nup58-mEGFP
1.4
1.3
1.2
1.1
1.0
0.9
0.8
0.7

I measured and mapped the *p/s* ratio of Nup-mEGFP fusion proteins across the imaged plane of the NE (Figure 13 A-D, *p/s* emission ratio). There was no observed relationship between *p/s* ratio and location along the nuclear surface, indicating that the measured *p/s* ratios are not due to the overall curvature of the nuclear envelope, but rather due to the orientation of the Nup-mEGFP fusion proteins with respect to the NPCs. All *p/s* ratios are presented on a logarithmic scale to enforce symmetry across the full measurement range.

3.4 Validating the Orientational Measurement: Flexible and Rigid Linkers

I fused the amino-terminal alpha helix of mEGFP to a predicted carboxyl-terminus of an alpha helix in my Nup fusion proteins to form a rigid conjugation between our proteins of interest and the mEGFP. In all cases, I deleted the first 4 amino acids of the mEGFP, which are unresolved in the crystal structure.

If the orientation of the excitation dipole of the mEGFP is held rigidly with respect to my Nups of interest, then changing the length of the alpha helix linker should change the orientation of the excitation dipole relative to the Nup. Specifically, if the link between the two proteins of interest is behaving like an alpha-helix, the addition of each individual amino acid should rotate the mEGFP around the axis of the alpha helix ~103 degrees. Therefore, with each added or removed amino acid the measured *p/s* ratio should shift in a defined manner if the mEGFP is reporting on the orientation of the protein of interest.

As a test that I was able to monitor the orientation of the protein of interest, I inserted different linkers between mEGFP (-5AA) and a test protein of interest (Nup54 after AA 494). I placed either a rigid linker, ala-glu-ala-ala-ala-lys-glu, or a flexible linker, gly-gly-gly-gly-ser-ser-gly, (Chen et al., 2013) between the Nup54 alpha-helix and the mEGFP. I then modulated the length of these linkers, providing linkages of 5, 6, and 7 amino acids to test the effects (Table 1).

TABLE 1: Nup54-mEGFP Fusion Proteins to Test the Ability of mEGFP to Report on the Orientation of the Nup.

Construct Name	Position of mEGFP within Nup	Size of mEGFP Deletion (AAs)	Linker Size (AAs)	Fusion Size (AAs)	Amino Acid Linker Sequence **Nup Sequence in Blue** **Linker Sequence in Red** **mEGFP Sequence in Green**
Nup54-mEGFP494(0)	494	5	5	**0**	**DIKLVAEAAAEELFT**
Nup54-mEGFP494(1)	494	5	6	**1**	**DIKLVAEAAAKEELFT**
Nup54-mEGFP494(2)	494	5	7	**2**	**DIKLVAEAAAKEEELFT**
Nup54-mEGFP494(flex0)	494	5	5	**0**	**DIKLVGGGGSEELFT**
Nup54-mEGFP494(flex1)	494	5	6	**1**	**DIKLVGGGGSSEELFT**
Nup54-mEGFP494(flex2)	494	5	7	**2**	**DIKLVGGGGSSGEELFT**

Rigid Linkers Reveal Addition of a Single Amino Acid Can Shift the p/s Ratio

Each rigid-linker fusion construct was transfected into cells and the *p/s* ratio was measured 48 hours later. Ten cells were imaged, and 50 puncta were identified from each cell and quantified. 300 NPCs were randomly selected for subsequent analysis from the puncta that were shaped like 2-dimensional Gaussians (Figure 12). For all imaging of *p/s* ratios presented going forward, cells were imaged and the data was processed in this manner.

When Nup54-mEGFP494(0) was imaged, it had a *p/s* ratio of 0.946 ± 0.079 (n=300). Nup54-mEGFP494(1), with one extra amino acid in the alpha helix, had a *p/s* ratio of 2.020 ± 0.196 (n=300). Nup54-mEGFP494(2) had a *p/s* ratio of 1.030 ± 0.076 (n=300) (Figure 14). These significant shifts in the *p/s* ratios of the mEGFP with each addition of a single amino acid suggest that the orientation of the mEGFP and its dipole are being rotated with each amino acid and thus, its orientation within the pore is determined by the orientation of the Nup54. In previous work, we used the crystal structure of a fluorescently labelled Nup to interpret these shifts in specific degrees of orientation (Kampmann et al., 2011). This analysis is explored for Nup133 in section 3.4 below. While I do not have enough structural information on the specifics of the structure of the Nup54 to model it as a fusion to mEGFP, the magnitude and significance of the changes in the *p/s* ratio demonstrate that the dipole of the mEGFP is a proxy for the orientation of the Nup54.

Flexible Linkers cause Orientational Sensors to Lose Sensitivity

Whereas the rigid linkers maintained the ability for a single amino acid to cause a shift in polarization of the mEGFP, the addition of amino acids had no effect on the *p/s* ratio with a flexible linker. When Nup54-mEGFP494(flex0) was measured, it had a *p/s* ratio of 1.284 ± 0.100 (n=300). Nup54-mEGFP494(flex1) had a *p/s* ratio of 1.310 ± 0.097 (n=300). Nup54-mEGFP494(flex2) had a *p/s* ratio of 1.428 ± 0.113 (n=300). The reductions in magnitude and significance of the differences in *p/s* ratios upon the use of a flexible linker versus a rigid linker suggest that the mEGFP is no longer held rigidly with respect to the protein of interest and that the *p/s* ratio no longer reports on the orientation of the protein of interest (Figure 14).

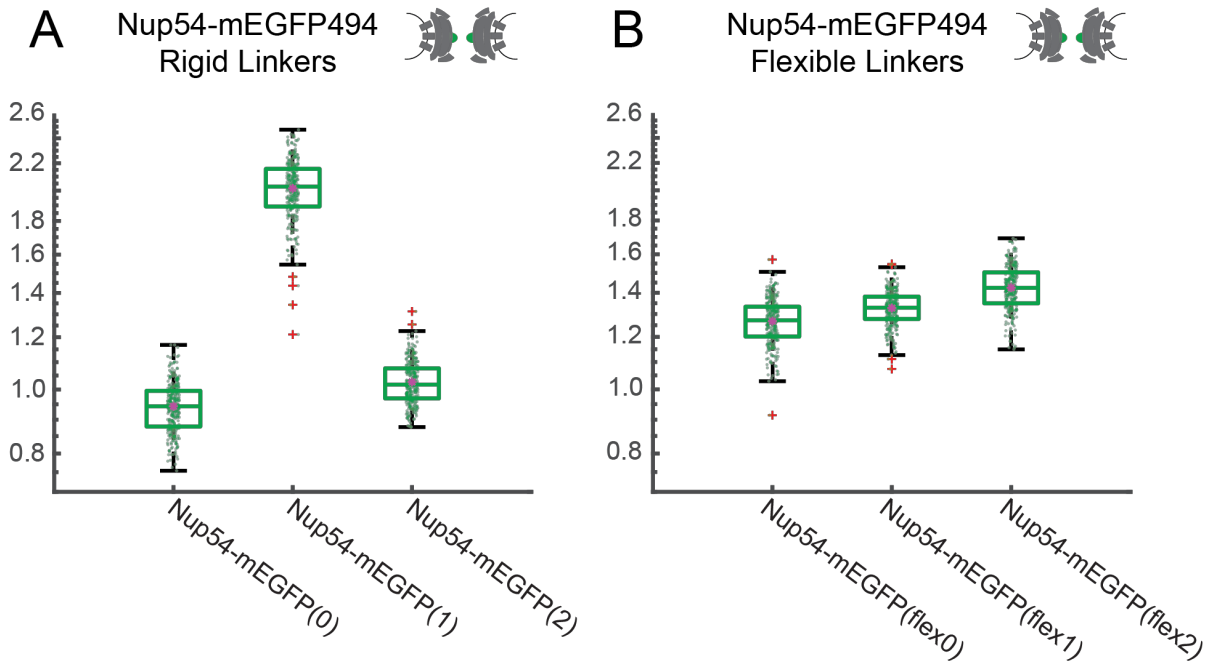

Figure 14. Rigid Linkers Preserve the Ability of mEGFP to Report on the Orientation of Nup54 *in vivo*

The orientation of mEGFP reports on the orientation of the Nup54-mEGFP fusion proteins. Flexible and rigid linkers were inserted between the mEGFP and Nup54. With each additional amino acid in a rigid alpha-helical linker, the GFP should rotate 103° relative to the Nup. Flexible linkers should reduce the rigidity with which the mEGFP is conjugated to the Nup, and therefore eliminate the effect of the addition of a single amino acid. A) Nup54-mEGFP494 fusion proteins with a rigid linker inserted between the Nup54 and the mEGFP. As the linker increased in length by a single amino acid, the *p/s* ratio shifted. B) Nup54-mEGFP494 fusion proteins with a flexible linker inserted between the Nup54 and the mEGFP. As the linker increased in length by a single amino acid, the *p/s* ratio did not shift. *(n=300, boxes indicate quartiles, center bars indicate medians, magenta stars indicate means, red crosses are outliers).*

3.5 Validating the Orientational Measurement: Modelling of Single Amino Acid Changes

As described above, changing the linker length of the alpha helix joining the protein of interest to the mEGFP should change the orientation of the excitation dipole. Crystal structures are available for Nup133 (Berke et al., 2004), and I used the USCF-Chimera software to model the fusion mEGFP to the Nup133. These crystal structures confirmed that the mEGFP fusion portion of the protein should rotate with respect to the Nup protein by ~103 degrees with each additional amino acid (Figure 15).

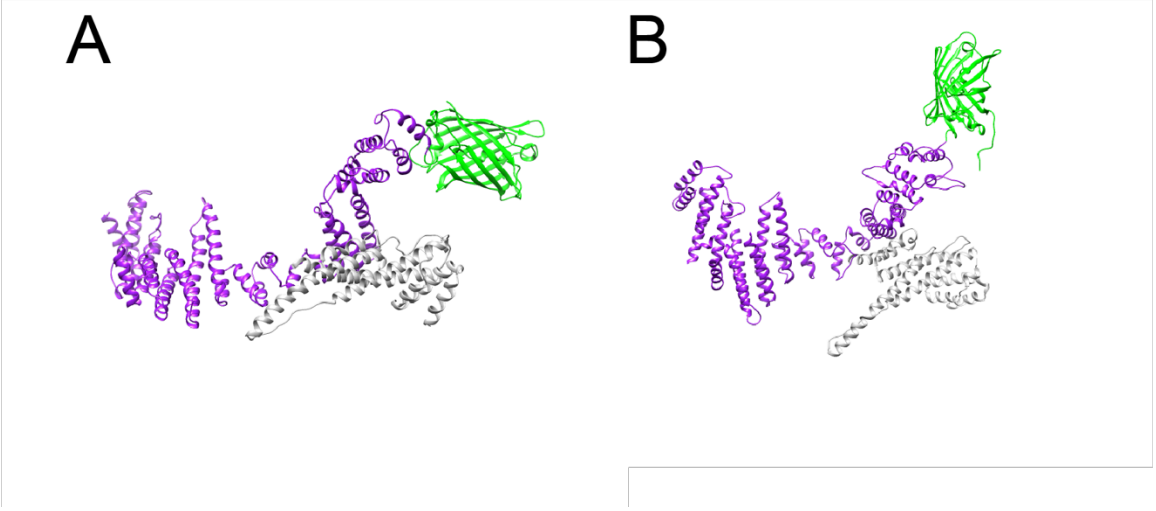

Figure 15. Molecular Models for Nup133-mEGFP Fusion Proteins Show that mEGFP Rotates upon the Addition of a Single Amino Acid

Models were constructed using the Nup133 portion of a crystal structure of a dimer of the C-terminal domains of human Nup133 and Nup107(Berke et al., 2004) and GFP (Elsliger et al., 1999). A) Nup133-mEGFP(-7) B) Nup133-mEGFP(-8).

3.6 Validating the Orientational Measurement: Validating Nup Orientational Sensors

Through the use of flexible and rigid linkers, I was able to show that polarized light microscopy, combined with a fusion protein with rigid conjugation of mEGFP to a Nup of interest, is capable of reporting on the orientation of the Nup. Furthermore, I was able to show that with the addition of a single amino acid, the *p/s* ratios of these fusion proteins experienced a significant orientational shift.

In order to probe the orientations and dynamics of proteins in different rings of the NPC, I built a series of fusion proteins to see whether the orientations of these Nups could be visualized *in vivo*. One potential concern when using the Nup-mEGFP fusion proteins to measure orientation is that the mEGFP itself might affect proper incorporation of the Nups into the NPC or that an aggregate of mEGFP proteins would form. Another concern is that the mEGFP tag might be located in a region of the protein whose structure itself is not rigid with respect to the nuclear-cytoplasmic axis.

I therefore made a series of Nup-mEGFP fusion proteins with different linker lengths for each Nup to test whether the *p/s* ratios of the fusion proteins reported on the orientation of the Nup in question (Table 2).

TABLE 2: Nup-mEGFP Fusion Proteins to Test for Improper Incorporation and Validate Orientational Measurement.

Nup	Construct Name	Position of mEGFP within Nup	Size of mEGFP Deletion (AAs)	Fusion Size (AAs)	Amino Acid Linker Sequence **Nup Sequence in Blue mEGFP Sequence in Green**
Nup133	Nup133_mEGFP(-7a)	Carboxyl-Terminus -2	5	**- 7**	**EYYVQGELFT**
Nup133	Nup133_mEGFP(-7b)	Carboxyl-Terminus -3	4	**- 7**	**EYYVQEELFT**
Nup133	Nup133_mEGFP(-8a)	Carboxyl-Terminus -4	4	**- 8**	**EYYVEELFT**
Nup133	Nup133_mEGFP(-8b)	Carboxyl-Terminus -3	5	**- 8**	**EYYVQELFT**
Nup93	Nup93_mEGFP510(-4)	Carboxyl - Terminus	4	**-4**	**EVLMNGEELFT**
Nup93	Nup93_mEGFP510(-5)	Carboxyl - Terminus	5	**-5**	**EVLMNEELFT**
Nup93	Nup93_mEGFP510(-6)	Carboxyl - Terminus	6	**-6**	**EVLMNELFT**

Nup	Construct Name	Position of mEGFP within Nup	Size of mEGFP Deletion (AAs)	Fusion Size (AAs)	Amino Acid Linker Sequence **Nup Sequence in Blue** **mEGFP Sequence in Green**
Nup54	Nup54_mEGFP494(-4)	494	4	**-4**	**DIKLVGEELFT**
Nup54	Nup54_mEGFP494(-5)	494	5	**-5**	**DIKLVEELFT**
Nup54	Nup54_mEGFP494(-6)	494	6	**-6**	**DIKLVELFT**
Nup54	Nup54_mEGFP510(-4)	510	4	**-4**	**GGVFSGEELFT**
Nup54	Nup54_mEGFP510(-5)	510	5	**-5**	**GGVFSEELFT**
Nup54	Nup54_mEGFP510(-6)	510	6	**-6**	**GGVFSELFT**
Nup58	Nup58_mEGFP412(-4)	412	4	**-4**	**KMFLGGEELFT**
Nup58	Nup58_mEGFP412(-5)	412	5	**-5**	**KMFLGEELFT**
Nup58	Nup58_mEGFP412(-6)	412	6	**-6**	**KMFLGELFT**

Nup133

For Nup133, which is localized to the Y-shaped complex, I imaged four constructs (Table 2). Nup133-mEGFP(-7A) has 3 amino acids removed from Nup133 and 4 amino acids removed from mEGFP, and Nup133-mEGFP(-7B) has 2 amino acids removed from Nup133 and 5 amino acids removed from mEGFP. Nup133-mEGFP(-8A) has 3 amino acids removed from Nup133 and 5 amino acids removed from mEGFP, and Nup133(-8B) has 4 amino acids removed from Nup133 and 4 amino acids removed mEGFP.

The *p/s* ratio of both constructs with a linker length of -7 amino acids was indistinguishable at 0.994 ± 0.101 (n=300) and 1.019 ± 0.095 (n=300) respectively and both constructs with a linker length of -8 amino acids had indistinguishable *p/s* ratios of 1.201 ± 0.116 (n=300) and 1.240 ± 0.118 (n=300) (Figure 16A). Both construct pairs with linkers of the same length therefore demonstrated similar orientations. Additionally, the constructs with different linker lengths were significantly different from each other in *p/s* ratio. The *p/s* ratio is directly reporting the orientation of the dipole of the mEGFP. These results demonstrate that since the linker is rigid, and the orientation of the mEGFP is rotated with the addition of an amino acid, this *p/s* ratio can be used to report the orientation of the Nup.

Because the behaviors of the linkers with equivalent lengths were indistinguishable, going forward I will only use Nup133-mEGFP(-7A) and Nup133-mEGFP(-8A) and refer to them as Nup133-mEGFP(-7) and Nup133-mEGFP(-8) respectively.

Nup93

For Nup93, localized to the adaptor ring of the NPC, the mEGFP was placed at the carboxyl-terminus of the protein (Table 1). Each construct has one fewer amino acid of mEGFP while keeping the Nup93 sequence the same. All constructs were imaged and the *p/s* ratio was calculated for each one (Figure 16B). Nup93-mEGFP(-4) had a *p/s* ratio of 1.309 ± 0.085 (n=300) and Nup93-mEGFP(-5) had an indistinguishable *p/s* ratio of 1.310 ± 0.072 (n=300). The third construct, Nup93-mEGFP(-6), had a *p/s* ratio of 1.185 ± 0.076 (n=300). Although for two of the three constructs there was no observable change in the orientation of the fusion protein with the removal of a single amino acid at the amino end of the mEGFP, the third construct is significantly different. Even though no shift is observed between the first two constructs, there was a definite shift in the mEGFP(-6) construct. A rotation of the mEGFP around the alpha helix may not always generate a rotation of the dipole in a manner that creates a measurable difference in the *p/s* ratio in our system, because our system only reports on the dipole's projection into two planes. Therefore, the evidence that I see a shift with one construct where a single amino acid is deleted is still evidence that the mEGFP is held rigidly with respect to Nup93. Therefore, with this construct, the orientation of the mEGFP is a proxy for the orientation of the Nup93.

Nup54

For Nup54, localized to the inner channel ring of the NPC, the mEGFP was placed in two locations. First, the mEGFP was placed at amino acid 494. Amino acid 494 is the carboxyl-terminus of the alpha helix that has been proposed in the ring

cycle hypothesis to undergo a shift of orientation (Melčák et al., 2007). Second, the mEGFP was placed at the carboxyl-terminus of the structured domain, which is the carboxyl-terminus of the entire protein.

For the fusion protein implicated in a possible diameter shift, where the mEGFP was placed at the end of the alpha helix (Amino Acid Number: 494), the *p/s* ratio shifted as the mEGFP was rotated around protein (Figure 16C). Nup54-mEGFP494(-4) had a *p/s* ratio of 0.820 ± 0.084 (n=300). Nup54-mEGFP494(-5) had an *p/s* ratio of 1.091 ± 0.089 (n=300). The third construct, Nup54-mEGFP494(-6), had a *p/s* ratio of 2.885 ± 0.596 (n=300). Therefore, the Nup54-494-mEGFP fusion proteins were incorporated into the NPC, and the mEGFP was held rigidly with respect to this part of Nup54. The orientation of the mEGFP is a proxy for the orientation of this part of Nup54.

For the construct where the mEGFP was placed at the end of the protein (Amino Acid Number: 510), the ratio did not shift when the length of the amino acid sequence was changed (Figure 16D). Nup54-mEGFP510(-4) had a *p/s* ratio of 1.099 ± 0.094 (n=300). Nup54-mEGFP510(-5) had an *p/s* ratio of 1.035 ± 0.092 (n=300). The third construct, Nup54-mEGFP510(-6), had a *p/s* ratio of 1.030 ± 0.094 (n=300). Because the ratio did not shift with respect to the protein, this result could mean that the protein was not properly incorporated into the NPC. Alternatively, it could mean that this domain is flexible within the endogenous protein and is therefore a poor location for an orientational sensor. Given that the fluorescence was observed at the NPC and this domain is expected to be flexible, it is likely the latter option: it was incorporated but is not a good proxy for orientation. Either way, it

cannot be used as a probe of orientation of Nup54 and I chose not to use this sensor going forward.

Nup58

For Nup58, localized to the inner channel ring of the NPC, the mEGFP was placed after the structured portion of this protein. Nup58 is an FG-Nup that contains two FG-domains, at both the N-terminal and C-terminal ends of the protein. I placed the mEGFP probe at the end of the anchor domain region, which lies in the middle of this protein. The *p/s* ratio of this construct did not shift when the length of the amino acid sequence was changed (Figure 16E). Nup58-mEGFP(-4) had a *p/s* ratio of 1.104 ± 0.093 (n=300). Nup58-mEGFP(-5) had an *p/s* ratio of 1.034 ± 0.095 (n=300). The third construct, Nup58-mEGFP(-6), had a *p/s* ratio of 1.031 ± 0.093 (n=300). Because the ratio did not shift with respect to the protein, this could mean that the protein was not properly incorporated into the NPC. Alternatively, it could mean that this domain was flexible within the endogenous protein and is therefore a poor location for an orientational sensor. I chose not to use this sensor for analysis.

Figure 16. Validation of Orientational Sensors for Nup133, Nup93, Nup 54, and Nup58.

I tested whether the orientation of mEGFP reports on the orientation of Nup-mEGFP fusion proteins by introducing changes in the number of amino acids in the rigid linker and assaying for shifts in the *p/s* ratio. With each additional amino acid in a rigid alpha-helical linker, the GFP should rotate 103° relative to the Nup, resulting in a possible change in the *p/s* ratio, which is evidence for the validity of the fusion protein as a orientational sensor. A) Nup133-mEGFP with the mEGFP at the carboxyl-terminus of the protein with constructs that have different linker lengths. Two pairs of linkers with the same linker length exhibit indistinguishable *p/s* ratios. A change in linker length by a single amino acid changes the measured *p/s* ratio. B) Nup93-mEGFP with the mEGFP at the carboxyl-terminus of the protein with constructs with different linker lengths. One deleted amino acid does not shift the *p/s* ratio, but a subsequent deletion of a single amino changes the measured *p/s* ratio. C) Nup54-mEGFP with the mEGFP at position (Amino Acid: 494). Each subsequent deletion of a single amino acid changes the measured *p/s* ratio. D) Nup54-mEGFP with the mEGFP at position (Amino Acid: 510). Each subsequent deletion of a single amino acid does not alter the measured *p/s* ratio. E) Nup58-mEGFP with the mEGFP at position (Amino Acid: 412). Each subsequent deletion of a single amino acid does not alter the measured *p/s* ratio. *(n=300, boxes indicate quartiles, center bars indicate medians, magenta stars indicate means, red crosses are outliers).*

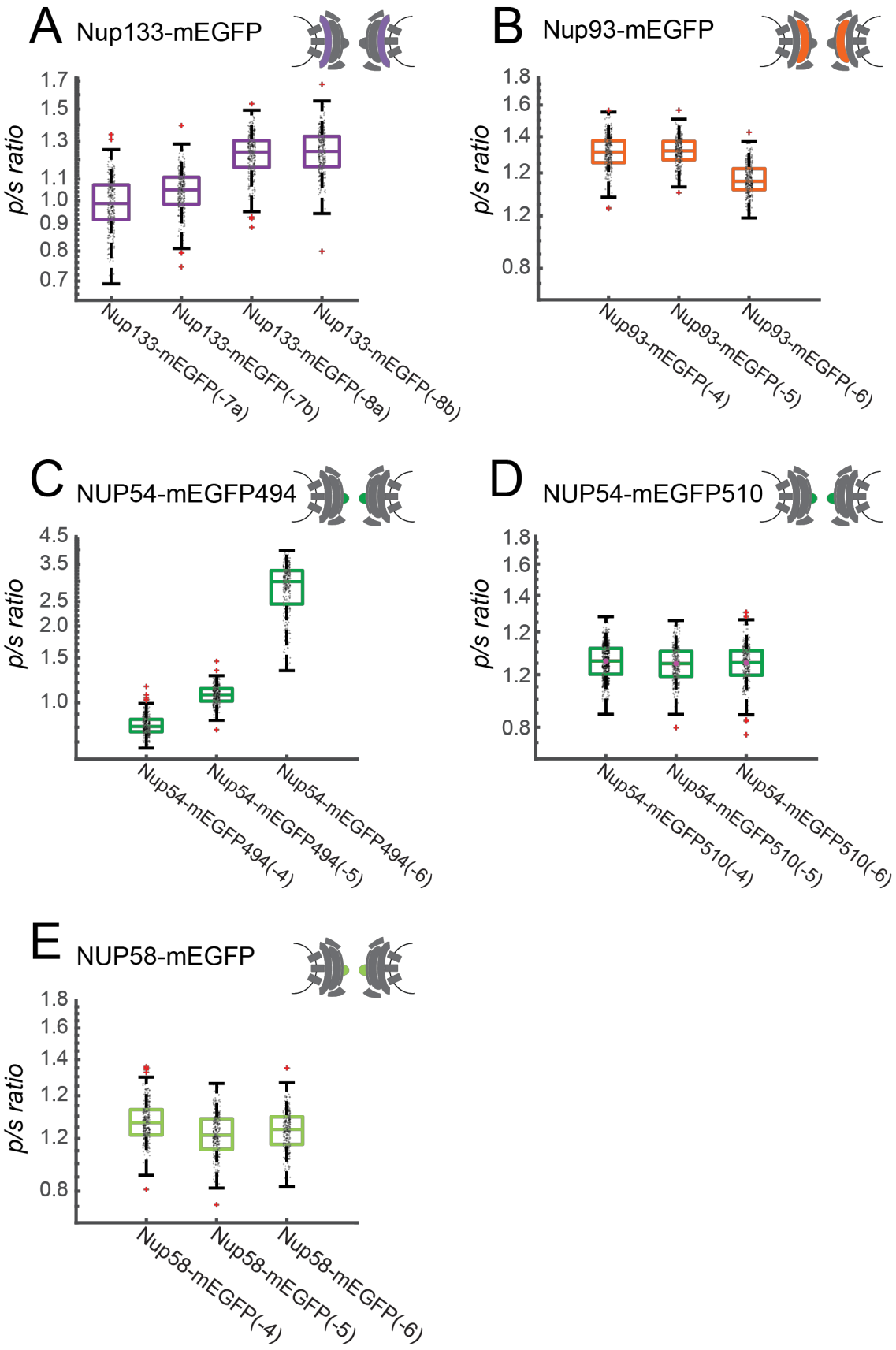
A
Nup133-mEGFP
p/s ratio
1.7
1.5
1.3
1.1
1.0
0.9
0.8
0.7
Nup133-mEGFP(-7a)
Nup133-mEGFP(-7b)
Nup133-mEGFP(-8a)
Nup133-mEGFP(-8b)
B
Nup93-mEGFP
p/s ratio
1.8
1.6
1.4
1.2
1.2
0.8
Nup93-mEGFP(-4)
Nup93-mEGFP(-5)
Nup93-mEGFP(-6)
C
NUP54-mEGFP494
p/s ratio
4.5
3.5
2.5
2.0
1.5
1.0
Nup54-mEGFP494(-4)
Nup54-mEGFP494(-5)
Nup54-mEGFP494(-6)
D
NUP54-mEGFP510
p/s ratio
1.8
1.6
1.4
1.2
1.2
0.8
Nup54-mEGFP510(-4)
Nup54-mEGFP510(-5)
Nup54-mEGFP510(-6)
E
NUP58-mEGFP
p/s ratio
1.8
1.6
1.4
1.2
1.2
0.8
Nup58-mEGFP(-4)
Nup58-mEGFP(-5)
Nup58-mEGFP(-6)

3.6 Fluctuations Over Time

In addition to visualizing the average orientations of each construct, I was interested in observing if the *p/s* ratio fluctuated over time. The shortest possible exposure time on our camera is 5 ms with a delay between each acquisition of 10 ms. Therefore, a new image can be collected every 15 ms. Although some cargo translocate the NPC in few milliseconds (Ribbeck and Görlich, 2001; Sun et al., 2008), a current estimation of dwell time of the pre-ribosome at the yeast NPC is ~90 ms (Delavoie et al., 2019).

To test if I could monitor fluctuations on the time scale of tens of milliseconds, I used the algorithm described above (Figure 12) to take the value of the maximum intensity pixel from the puncta in each raw image and calculate the emission in response to varying the excitation by p and s via the following equation (Figure 17) :

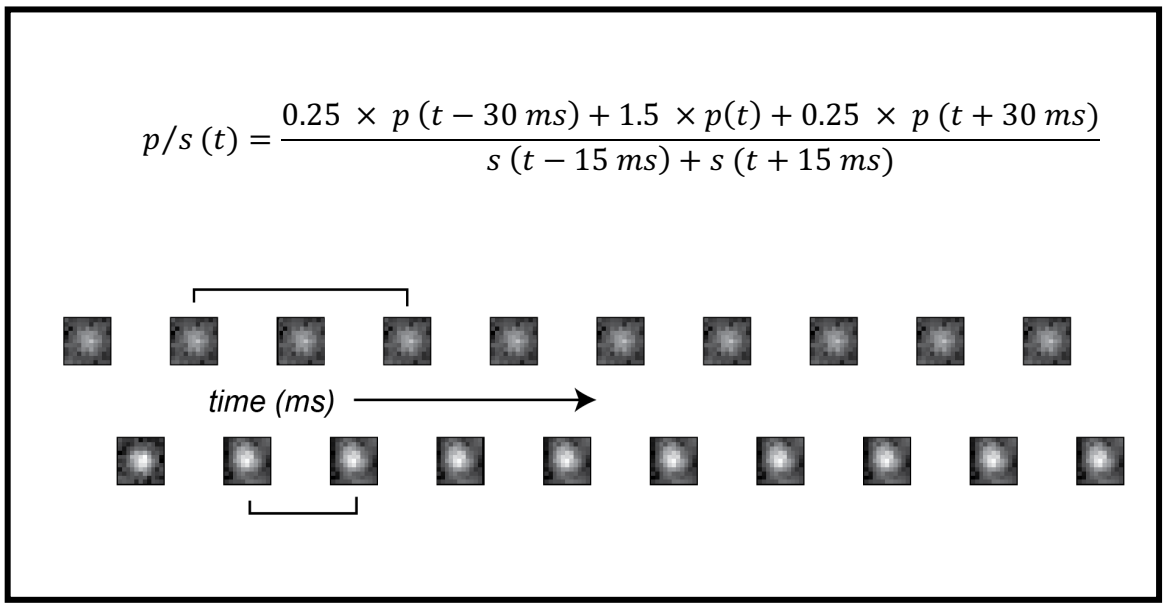

Figure 17. Quantification of Orientational Fluctuation

Images were collected every 15 ms and a sliding window was used to calculate a *p/s* orientation measurement every 30 ms.

The *p/s* ratio over time was calculated and plotted for each orientational sensor (Figure 17). Each line in the graphs represents the *p/s* ratio of an orientational sensor within a single NPC imaged over 210 ms. For each of the plots, these NPC traces are taken from a single cell imaged over time.

In order to quantify the fluctuations in the *p/s* ratio for a specific construct in each cell, I calculated the average change of the log of the emission ratio over time for every time point in every NPC.

$$fluctuations\ per\ cell\ = average(|\Delta \log(p/s\ \ emission\ ratio)/time|)$$

With this metric, I was able to quantify the magnitude of the *p/s* ratio fluctuations in a manner that was insensitive to the distance of the measured *p/s* ratio from 1.

No measured statistical difference was found between the different Nup133 constructs, nor was there a difference between the different Nup54 constructs, nor between the different Nup93 constructs (Figure 18D). However, a grouped test showed that the group of the Nup133 constructs were statistically distinct from the Nup54 constructs with $p < 0.01$ *(Kruskal-Wallis test).* Furthermore, the Nup133 constructs and the Nup54 constructs were both statistically distinct from the Nup93 constructs with $p < 0.001$ *(Kruskal-Wallis test).*

Because the differences in the magnitudes of fluctuations were tied to Nup identity, these differences in the measured fluctuations could be due to inherent differences in the protein flexibilities, or they could be due to the effect of different incorporation rates of the transient transfections into the NPC, leading to different background characteristics. In order to probe deeper into the effect of fluctuations, I sought to find a system with improved signal to noise.

Figure 18. Fluctuations in the *p/s* Ratio.

The *p/s* ratios of the Nup-mEGFP fusion proteins can be measured over time and their dynamics can be quantified. A) The *p/s* ratio is calculated every 30 ms for Nup133-mEGFP constructs with the mEGFP at the carboxyl-terminus of the protein and linkers of different lengths. (n=20, each line represents the *p/s* ratio of a single NPC tracked over time). B) The *p/s* ratio is calculated every 30 ms for Nup54-mEGFP constructs with the mEGFP at the carboxyl-terminus of amino acid 494 and linkers of different lengths. (n=20, each line represents the *p/s* ratio of a single NPC tracked over time). C) The *p/s* ratio is calculated every 30 ms for Nup93-mEGFP constructs with the mEGFP at the carboxyl-terminus of the protein and linkers of different lengths. (n=20, each line represents the *p/s* ratio of a single NPC tracked over time). D) Average fluctuations for all NPCs measured within a cell, each data point represents the average fluctuations in one cell (n=10). *(boxes indicate quartiles, center bars indicate medians, red crosses are outliers; Kruskal-Wallis test, **, p<0.01, ***, p<0.001).*

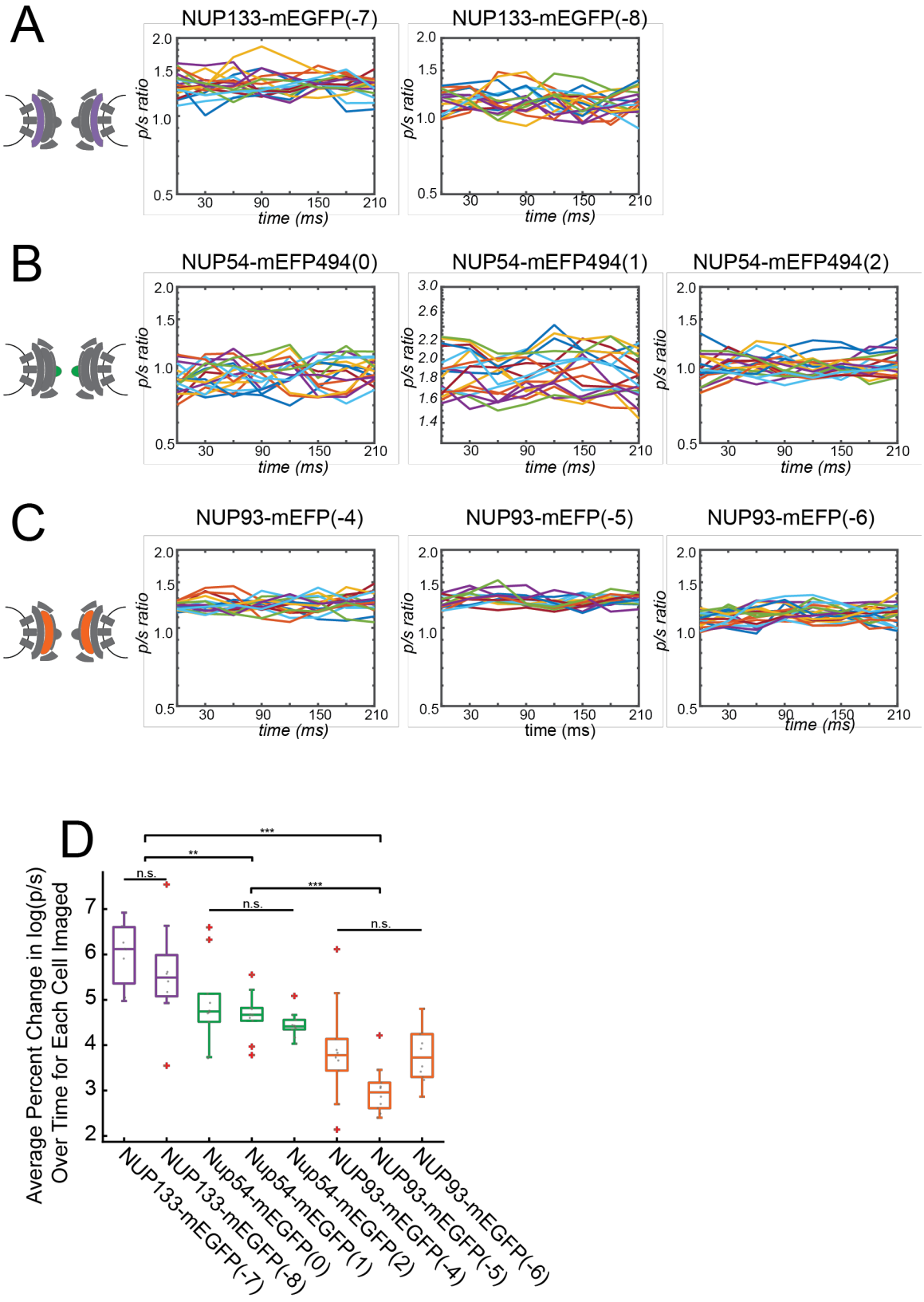
A
NUP133-mEGFP(-7)
NUP133-mEGFP(-8)
B
NUP54-mEFP494(0)
NUP54-mEFP494(1)
NUP54-mEFP494(2)
C
NUP93-mEFP(-4)
NUP93-mEFP(-5)
NUP93-mEFP(-6)
p/s ratio
time (ms)
D
Average Percent Change in log(p/s) Over Time for Each Cell Imaged
n.s.
**
***
NUP133-mEGFP(-7)
NUP133-mEGFP(-8)
Nup54-mEGFP(0)
Nup54-mEGFP(1)
Nup54-mEGFP(2)
NUP93-mEGFP(-4)
NUP93-mEGFP(-5)
NUP93-mEGFP(-6)

3.7 HAP1 CRISPR Cell Lines

I built CRISPR cell lines where all copies of either Nup133 or Nup54 are replaced with the fusion protein sensor equivalent. CRISPR cell lines offered two potential advantages. First, these lines could improve the signal to noise of the recording because now every copy of the Nup would be fused to a mEGFP. Second, replacing all Nup133 or Nup54 proteins with Nup-mEGFP fusion proteins would be a test of whether the presence of the orientational sensor in the Nup had any detectable effects on the function of the NPC. If all of the copies can be replaced without any detectable effects on cell division, it would argue that the addition of the mEGFP does not significantly compromise on the function of the Nups.

I used HAP1 Cells (Horizon Discovery, Cambridge, UK), a fibroblast-like adherent cell line derived from the chronic myelogenous leukemia cell line KBM-7. This cell line was engineered for the creation of gene edited cell lines by the reduction of the chromosomes to haploid. In early passages, almost all chromosomes are haploid, but after ~20 generations many of the chromosomes revert to diploid state. Since the early passages are haploid, the incidence of homozygous clones from a CRISPR gene-editing experiment are higher than most cell lines.

I provided a CRISPR CAS9 protein and guide via transfection along with a rescue gene fragment containing my mEGFP sequence (details in Methods, page 190). The cells were selected for transfection with puromycin and then allowed to recover. After recovery, the cells were sorted via fluorescent activated cell sorting (FACS). Cells expressing mEGFP were selected and grown clonally. These clonal

cell lines were then screened for incorporation of mEGFP into the NPC. If the mEGFP was incorporated into the NPC, the gene region of interest was amplified via PCR to test for homozygosity. I found that approximately 10% of the cell lines tested were homozygous for the mEGFP insertions at the Nup locations.

Cell lines were built in HAP1 cells via homozygous incorporation of the conformational sensors (Table 3). PCR amplification of the gene of interest showed two bands when the lines were heterozygous and one band when the lines were homozygous (Figure 19). These bands were sequenced to verify proper incorporation of the mEGFP. mEGFP expression of the Nup-mEGFP proteins was confirmed via microscopy. In addition, I confirmed that the only band detectable on a western blot probed with an α-mEGFP antibody was a fusion protein that ran at the appropriate molecular weight (Figure 20).

TABLE 3: CRISPR Nup-mEGFP Cell Lines.

Nup	Construct Name	Position of mEGFP within Nup	Number of Amino Acids Removed from mEGFP	Linker Size (AAs)	Fusion Size	Amino Acid Linker Sequence **Nup Sequence in Blue** **Linker Sequence in Red** **mEGFP Sequence in Green**
Nup54	Nup54-mEGFP494(0)	494	5	5	**0**	**DIKLVAEAAAEELFT**
Nup54	Nup54-mEGFP494(1)	494	5	6	**1**	**DIKLVAEAAAKEELFT**
Nup54	Nup54-mEGFP494(2)	494	5	7	**2**	**DIKLVAEAAAKEEELFT**
Nup133	Nup133-mEGFP(-7)	Carboxyl-Terminus-3	4	0	**-7**	**EYYVQEELFT**
Nup133	Nup133-mEGFP(-8)	Carboxyl-Terminus-3	5	0	**-8**	**EYYVQELFT**

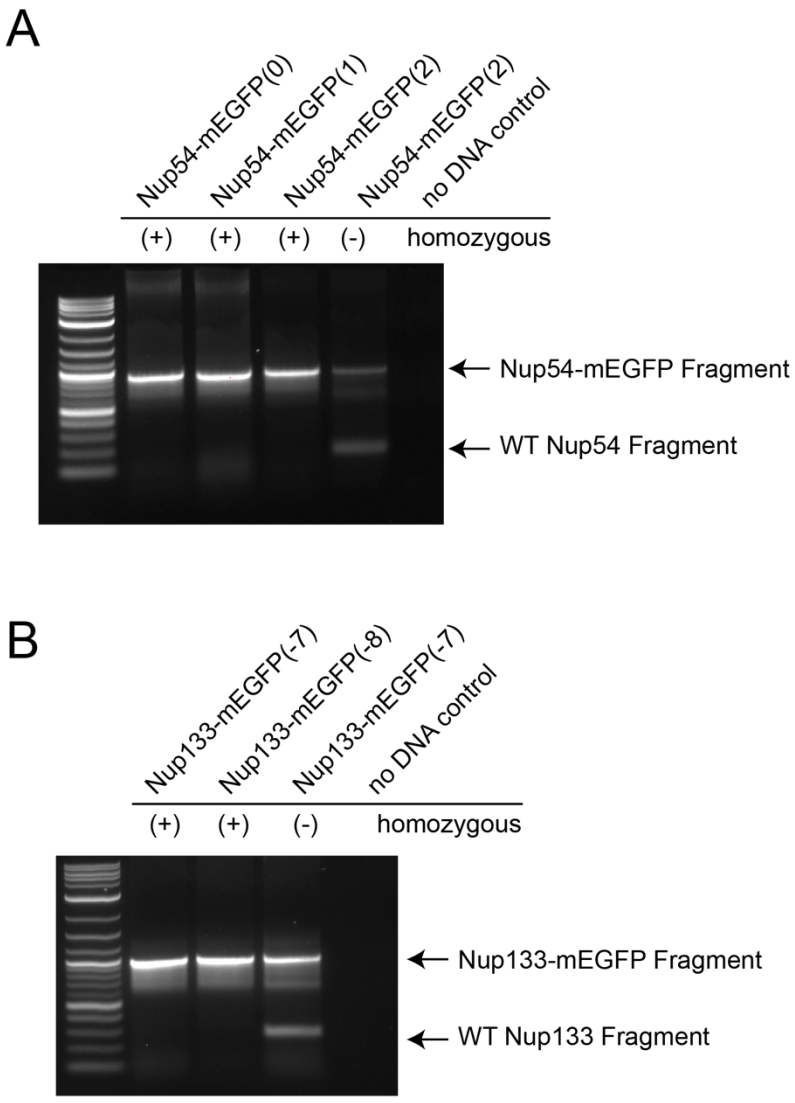

Figure 19. PCR Conformation of Homozygous Incorporation of Fusion Proteins

PCR amplification of the A) Nup54 and B) Nup133 region reveal one band when the Nup-mEGFP region is homozygous for mEGFP incorporation and two bands when the region is heterozygous. The bands were sequenced to verify proper incorporation of the mEGFP.

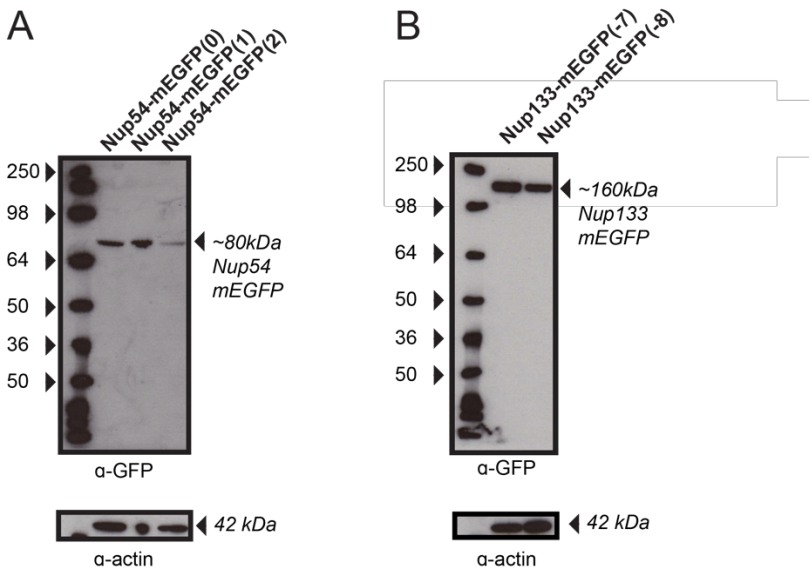

Figure 20. Western Blot Confirms that the mEGFP Expressed is the Nup-mEGFP Fusion Protein

Western blot probed for α-GFP detects A) Nup54 and B) Nup133 fusion proteins as expected. The blots were stripped of α-GFP and probed with α-actin to confirm protein loading.

3.8 Orientational Measurements in HAP1 CRISPR Lines

The ability of the fusion proteins in the CRISPR cell lines to perform the function of orientational sensors was ascertained by measuring their *p/s* orientations and seeing if they behaved similarly to the transiently transfected sensors. All cell lines presented showed normal morphology and normal rates of growth, suggesting there were no significant effects of replacing the endogenous Nups with an equivalent with an orientation sensor.

Nup133

The Nup133-mEGFP CRISPR cell lines all expressed Nup133-mEGFP fusion proteins and could be imaged under pol-TIRF microscopy. With the CRISPR cell lines, the *p/s* ratios of the fusion proteins could be calculated. The Nup133-mEGFP(-7) CRISPR cell line had a *p/s* ratio of 0.869 ± 0.075 (n=300), compared to the transiently transfected Nup133-mEGFP(-7) construct, which had a *p/s* ratio of 1.155 ± 0.089 (Figure 20B). The Nup133-mEGFP(-8) CRISPR cell line had a *p/s* ratio of 1.0383 ± 0.086 (n=300), compared to the transiently transfected Nup133-mEGFP(-8) construct, which had a *p/s* ratio of 1.281 ± 0.099. The magnitude of the *p/s* ratios were not the same for the transient transfections in HeLa cells and the stable expression with CRISPR/Cas9 in the Hap1 cells, for reasons discussed below. However, the same variation in the length of the linker, from -7 amino acids to -8, had the same effect on decreasing in *p/s* orientation.

Nup54

The Nup54-mEGFP CRISPR cell lines all expressed Nup54-mEGFP fusion proteins and could be imaged under pol-TIRF microscopy. With the CRISPR cell lines, the *p/s* ratios of the fusion proteins could be calculated. The CRISPR cell lines had similar *p/s* ratios as their transiently-transfected equivalents (Figure 20A). The Nup54-mEGFP494(0) cell line had a measured *p/s* ratio of 0.813 ± 0.086 (n=300), the Nup54-mEGFP494(1) had a measured *p/s* ratio of 1.889 ± 0.188 (n=300), and the Nup54-mEGFP494(2) had a measured *p/s* ratio of 0.986 ± 0.102 (n=300). As described above, the magnitude of the *p/s* ratio is not identical for conformational reporters expressed transiently in HeLa cells and stably expressed in Hap1 cells. This may be due to a confluence of different reasons, as discussed below. However, varying the length of the spacer between the Nup and conformational sensors had a corresponding equivalent effect on *p/s* ratio when assayed in the transiently transfected cells or when assayed in the cells stably expressing the reporter as a replacement for the endogenous protein.

Total Intensity of NPCs in CRISPR Cell Lines

Various factors could affect the absolute value of the *p/s* ratio. The differences in the mean *p/s* ratios might be because of different signal to noise ratios. In general, there is more noise in the *p*-polarized images, which may be why all of the CRISPR cell lines exhibit lower *p/s* ratios than their transiently transfected equivalents. Another possible contributor to the difference in *p/s* ratio might be the height of the fluorophore above the cover slip.

Unfortunately, the HAP1 cell line positions its nuclei higher from the coverslip than the HeLa cells. There may be different optical properties when imaging deeper into the sample. This effect is a function of the efficacy of photon capture as well as various aberrations introduced in objectives that have a high numerical aperture. Because the intensity of the excitation laser decreases exponentially into the sample in TIRF microscopy, the measured intensity of these cells was less than that of the transiently transfected lines, even though one might have expected a higher intensity since all copies of the Nup are tagged (Figure 21A and 21C). I measured total NPC emission by calculating $p + 2 \times s$.

For all transient transfections of Nup-133, no measured statistical differences in intensity were found between the constructs of different linker lengths, indicating that a similar number of Nup133-mEGFP proteins were incorporated in the NPC for each linker length for each Nup133 fusion proteins.

The CRISPR Nup133 cell lines exhibit similar total emission to that of the transient transfections (Figure 21C). This result suggests that more of the Nup133-mEGFP proteins are being incorporated into the NPC in the CRISPR cell lines, because even though these constructs are farther away from the coverslip, similar intensities are measured.

Two of the CRISPR Nup54 cell lines do not show a statistical difference in their total NPC intensities, Nup54-mEGFP494(0) and Nup54-mEGFP(1). Notably, a significantly lower intensity was measured for one specific reporter, the Nup54-494-mEGFP(2) in the CRISPR lines. Coupled with the lower intensity of protein levels, as assayed by Western (Figure 20), this result suggests that in the CRISPR cell line,

the conformational reporter may not be as efficiently incorporated into the NPC as the native protein nor the other conformational sensors for Nup54. Interestingly, the *p/s* ratio of this construct was around 1, which might indicate that it is not being held with a distinct orientation relative to NPC, because most of the transient transfections that I imaged that did not experience shifts with the addition of a single amino acid had *p/s* ratios of around 1 (and unconstrained, cytoplasmic mEGFP has a *p/s* ratio of 1). Thus, this specific conformational reporter may be downregulated or it may not be properly incorporated into the nuclear pore. Therefore, I did not proceed with this construct or its transiently transfected equivalent.

Signal to Noise of CRISPR Cell Lines

Although the Nup133-mEGFP CRISPR cell lines were similar in total intensity, they did exhibit higher signal to noise (Figure 21D). The signal to noise was calculated as the summed intensity from the highest intensity pixel of a NPC (p_{max} + 2 x s_{max}) divided by the summed intensity from the lowest intensity pixel within a radius of 6 pixels (p_{min} + 2 x s_{min}).

Although the Nup54-mEGFP CRISPR cell lines did not show brighter intensities at the nuclear pores, they did exhibit better signal to noise. The signal to noise was calculated as the summed intensity from the highest intensity pixel of a NPC (p_{max} + 2 x s_{max}) divided by the summed intensity from the lowest intensity pixel within a radius of 6 pixels (p_{min} + 2 x s_{min}). The signal to noise of all CRISPR lines was significantly higher than that of the transient transfections (Figure 22B and 22D), indicating that they may be useful for characterizing the orientational fluctuations over time of the Nup54.

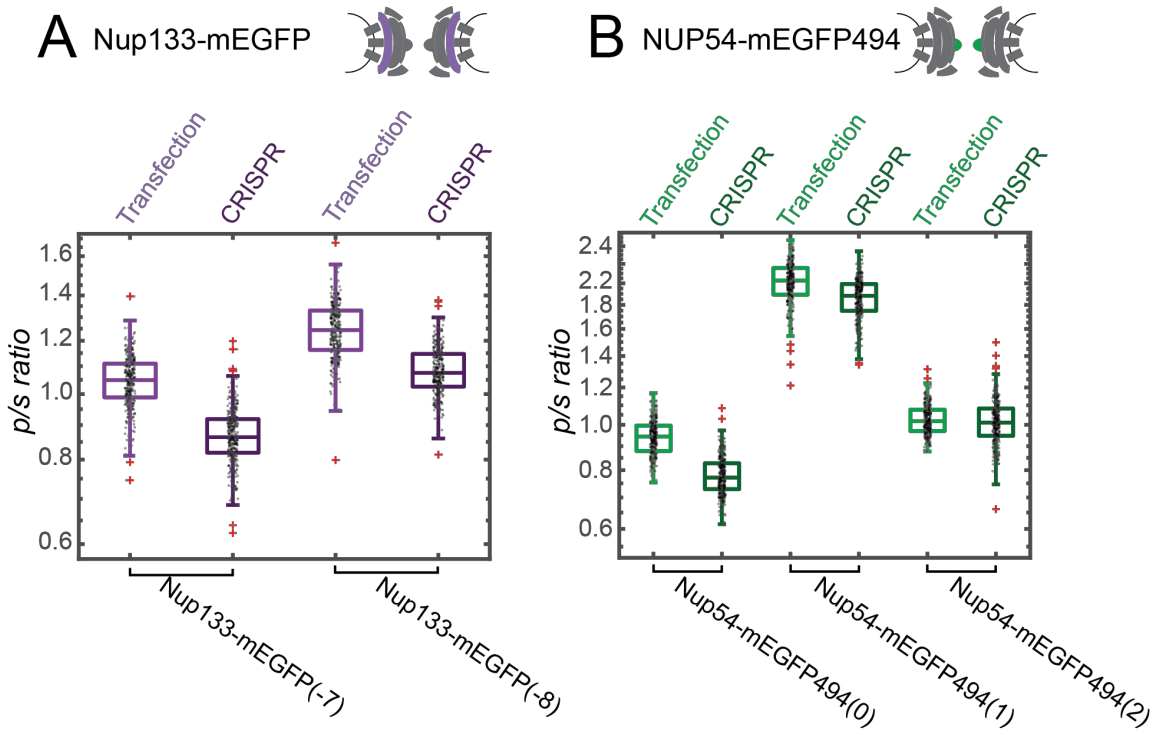

Figure 21. *p/s* Ratio Measurements of CRISPR Cell Lines Correspond to Transient Transfection of the Equivalent Orientational Sensors.

A) Nup133-mEGFP with the mEGFP at the carboxyl-terminus of Nup133. The deletion of a single amino acid changes the measured *p/s* ratio, and the CRISPR cell lines mimic the trend that the orientations of the transient transfections show. B) For Nup54-mEGFP, each subsequent insertion of a single amino acid changes the measured *p/s* ratio, and the CRISPR cell lines mimic the orientations of the transient transfections. *(n=300, boxes indicate quartiles, center bars indicate medians, magenta stars indicate means, red crosses are outliers).*

Figure 22. Total intensities and signal to noise of CRISPR cell lines versus Transient Transfections.

A) Nup54-mEGFP with the mEGFP at position AA494. Total intensities (p_{max} + 2 x s_{max}) of individual NPCs in transient transfections and CRISPR cell lines. B) Nup54-mEGFP with the mEGFP at position (Amino Acid: 494). Signal to noise (p_{max} + 2 x s_{max})/ (p_{min} + 2 x s_{min}) of individual NPCs of transient transfections and CRISPR cell lines. C) Nup133-mEGFP with the mEGFP at carboxyl terminus. Total intensities (p_{max} + 2 x s_{max}) of individual NPCs of transient transfections and CRISPR cell lines. D) Nup133-mEGFP with the mEGFP at carboxyl terminus. Signal to noise (p_{max} + 2 x s_{max})/ (p_{min} + 2 x s_{min}) of individual NPCs of transient transfections and CRISPR cell lines. *(n=150, boxes indicate quartiles, center bars indicate medians, magenta stars indicate means, red crosses are outliers).*

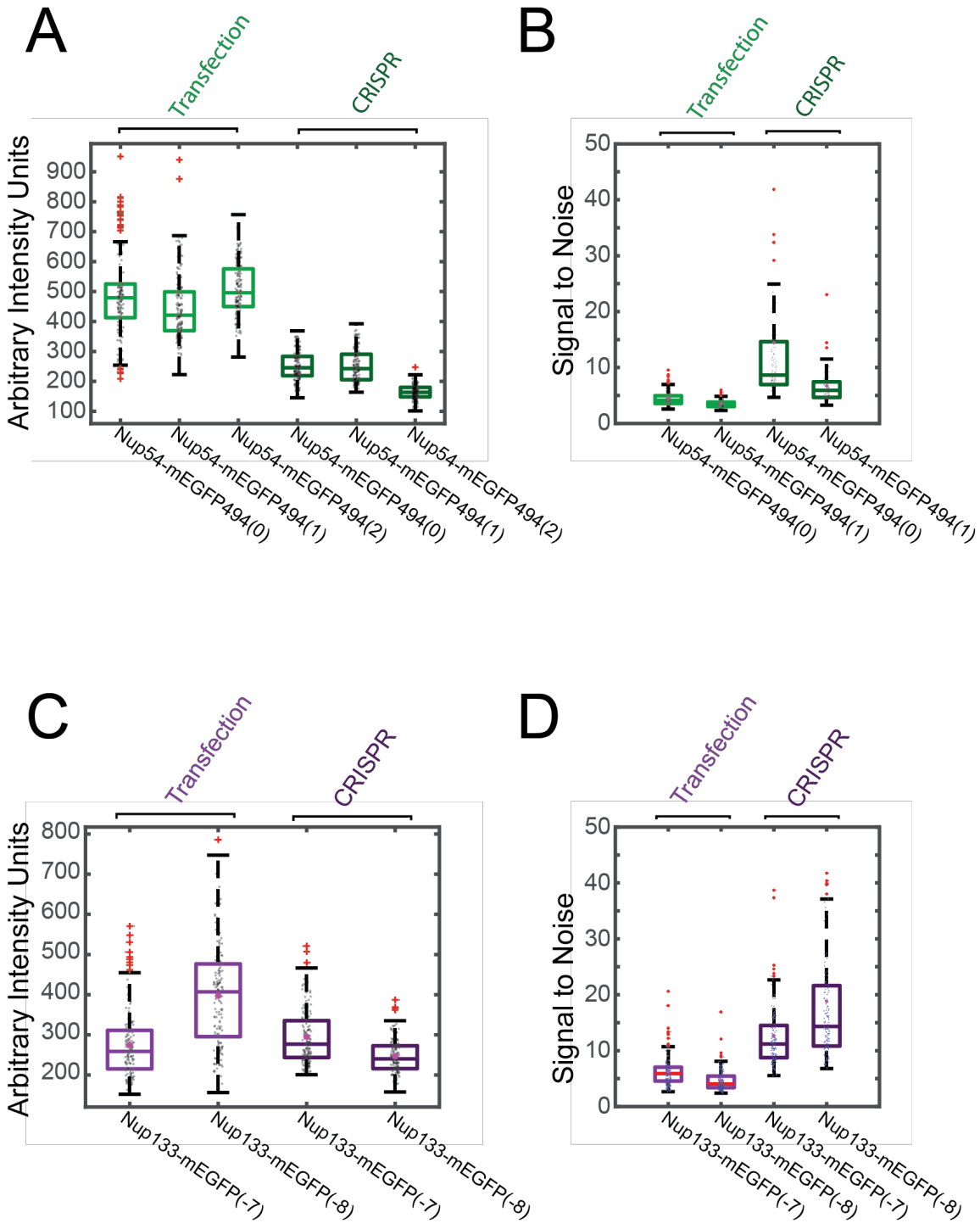
A
Transfection
CRISPR
Arbitrary Intensity Units
900
800
700
600
500
400
300
200
100
Nup54-mEGFP494(0)
Nup54-mEGFP494(1)
Nup54-mEGFP494(2)
Nup54-mEGFP494(0)
Nup54-mEGFP494(1)
Nup54-mEGFP494(2)
B
Transfection
CRISPR
Signal to Noise
50
40
30
20
10
0
Nup54-mEGFP494(0)
Nup54-mEGFP494(1)
Nup54-mEGFP494(0)
Nup54-mEGFP494(1)
C
Transfection
CRISPR
Arbitrary Intensity Units
800
700
600
500
400
300
200
Nup133-mEGFP(-7)
Nup133-mEGFP(-8)
Nup133-mEGFP(-7)
Nup133-mEGFP(-8)
D
Transfection
CRISPR
Signal to Noise
50
40
30
20
10
0
Nup133-mEGFP(-7)
Nup133-mEGFP(-8)
Nup133-mEGFP(-7)
Nup133-mEGFP(-8)

3.9 *p/s* Fluctuations in *p/s* ratio in HAP1 CRISPR Cell Lines

With the improved signal to noise of the CRISPR cell lines, I was interested to see if I could more accurately measure the fluctuations in the orientations over time.

With the same metric as before (page 75), I calculated the variance in the *p/s* ratio again. There was no significant difference between the CRISPR cell lines for both Nup133 and Nup54 (Figure 21), suggesting that both of these domains exhibit similar dynamics at the level of detection of my technique. The magnitude of the fluctuations was greater than or equal to the fluctuations measured in the transient transfections. This method of quantifying the magnitude fluctuations is useful for probing how the behaviors of these domains change under different physiological conditions.

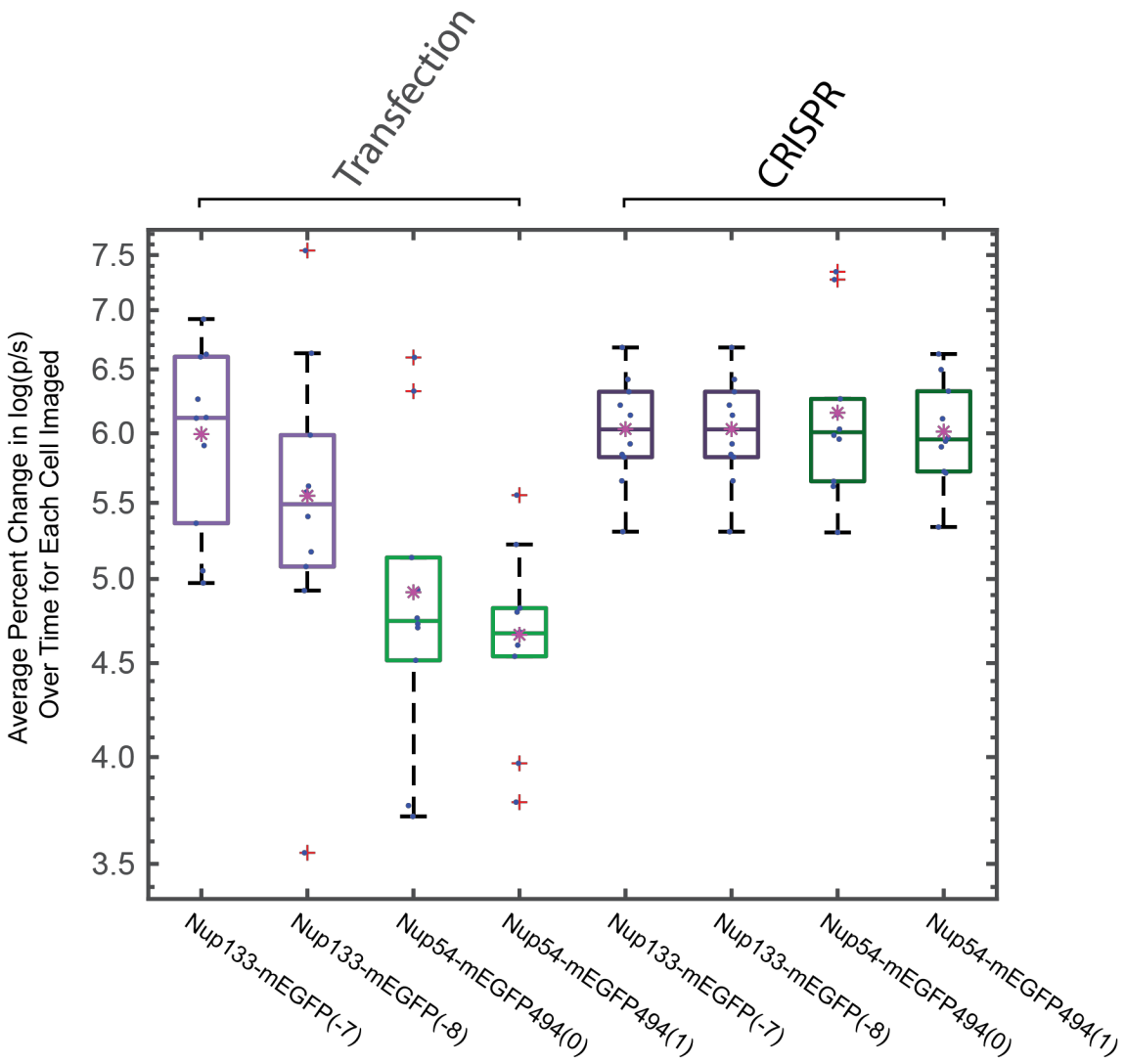

Figure 23. Fluctuations in Orientation over time in CRISPR Cell Lines versus Transient Transfections.

Average fluctuations for all NPCs measured within a cell, each data point represents the average fluctuations in one cell. *(boxes indicate quartiles, center bars indicate medians, red crosses are outliers)*

CHAPTER 4: NPC CONFORMATIONAL SENSORS REVEAL THAT THE CONFORMATION OF THE NPC CHANGES IN DIFFERENT TRANSPORT CONDITIONS

As seen in Chapter 3, I have built and validated sensors that report on the orientations of Nups *in vivo*. In the following chapter, I will describe how I proceeded to measure the orientations and dynamics of the Nups under different transport conditions with these tools.

The conditions that I used to perturb transport include starvation. Starvation has previously been shown in yeast to reduce transport. Here I used a light-activated transport cargo to demonstrate that starvation has a similar effect in mammalian cells. A second perturbation I used was treatment with DN Ran, which attenuated the karyopherin-driven cargo translocation through the NPC. A third perturbation was the removal of cytosol via digitonin permeabilization and a fourth was the removal of cargo complexes via the addition of exogenous Ran-GTP to the nuclear periphery. The orientations of the constructs were also measured after the FG-Nups were crosslinked with wheat germ agglutinin (WGA).

Under these different transport states, Nup54-mEGFP, a member of the inner ring of the NPC, underwent a reorganization upon perturbing the transport of cargo. The other Nups tested, Nup133 and Nup93, did not exhibit this behavior.

In order to test whether these alterations in orientation were associated with any changes in the organization of the FG-Nups within the lumen of the NPC, I performed a FRET-assay to test whether the distances between the FG-Nup ‘finger’ domains of Nup62 were altered after starvation. Preliminary measurements suggest

that these domains are closer to each other under conditions of starvation, suggesting that the of the lumen NPC also experiences a reorganization after starvation.

4.1 NPC Perturbation 1: Starvation

In yeast, it is known that starvation inhibits NLS-driven cargo import (Stochaj et al., 2000). Starvation causes a reduction in the nuclear accumulation of NLS-tagged GFP, as the GFP can slowly diffuse out of the NPC and is not reaccumulated because kap-mediated nuclear import is attenuated.

When cells are starved, many of their intracellular process are altered, including rates of gene expression and growth. One might expect that the flux of NLS-driven transport through the NPC would be reduced and local regulation of the NPC would be altered after starvation. I was interested to see if under the condition of nutrient starvation, there would be any alterations to the orientations and dynamics of my conformational sensors.

Cells were grown in complete media (CM, Dulbecco's Modifed Eagle Media + 10 % FBS) and orientational measurements were taken 48 hours post transfection. Starved cells were placed in Hank's Buffered Salt Serum (HBSS, with Calcium and Magnesium) for 24 hours before imaging to ascertain whether there were any changes in NPC orientational order.

Import Rates in Starved Cells

Although it is known in yeast that the NLS-mEGFP cargo does not localize to the nucleus when yeast cells are placed in HBSS, the effects of HBSS on mammalian NLS-driven nuclear import is uncharacterized to my knowledge.

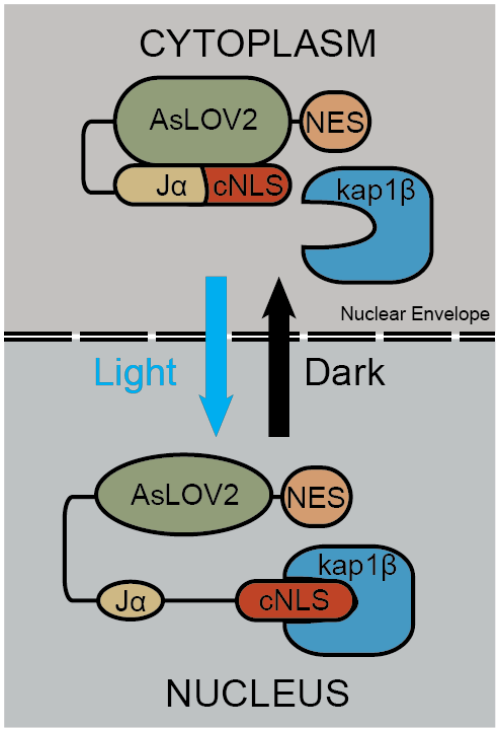

Figure 24. Schematic of Light Activated Nuclear Shuttle (LANS)

The NLS domain of the LANS construct normally masked by the AsLOV2 domain and the protein remains predominantly in the cytosol. Upon stimulation with blue light, the NLS is unmasked and the construct translocates into the NPC. *Figure Adapted from* (Yumerefendi et al., 2015)

To test if there was any difference in the ability of my cells to undergo kap-mediated import post starvation, I tested the import rates of a light-activated nuclear shuttle (LANS) (Yumerefendi et al., 2015) This fluorescent LANS construct is composed of an mCherry fluorescent protein conjugated to a weak NES and a stronger NLS that is normally obscured by the Light Oxygen Voltage (AsLOV2) domain of photoropin1 from *Avena sativa*. In the dark, the LOV2 domain adopts a closed conformation that sterically blocks the NLS motif and exposes the NES. Therefore, in unstressed cells,

this construct is excluded from the nucleus when not exposed to blue light (Figure 24). Once the LOV2 domain is activated with blue light, the C-terminus of the protein unfolds and reveals an NLS which can then interact with kaps and drive the protein to be imported into the cell nucleus. Light inducible nuclear shuttles have been used to control both the localization and activity of proteins in mammalian cells, yeast, and *C. elegans* (Niopek et al., 2014; Yumerefendi et al., 2015).

HeLa cells were transfected with mCherry-LANS 48 hours prior to imaging. Starved cells were placed in HBSS 24 hours prior to imaging, while control cells were kept in CM. Both conditions were imaged with 594 excitation laser (5mW, 200ms) at 20s intervals for 30 minutes. After 2 minutes of imaging, the construct was activated with a 488 nm laser (3mW, 2s exposures, every 20 s). The activating pulses continued for thirteen minutes, and then cells were imaged through a 15 minute recovery period. These imaging conditions were optimized for maximal cell health and cargo translocation with Brennan Carman (SURF Student, 2018). Six cells were imaged for each condition.

Compared to most cells in CM, the cells in HBSS exhibited lower rates of nuclear trafficking of mCherry-LANS (Figure 25A). Notably, the Nuclear/Cytoplasmic ratio of cargo in starved cells was lower than the cells in CM from the onset, suggesting that import and export were affected asymmetrically by the starvation, and import might be more affected then export. Overall, a smaller fraction of cargo was recruited into the nucleus with blue light activation, but the time course of this recruitment remained largely unaffected (Figure 25B).

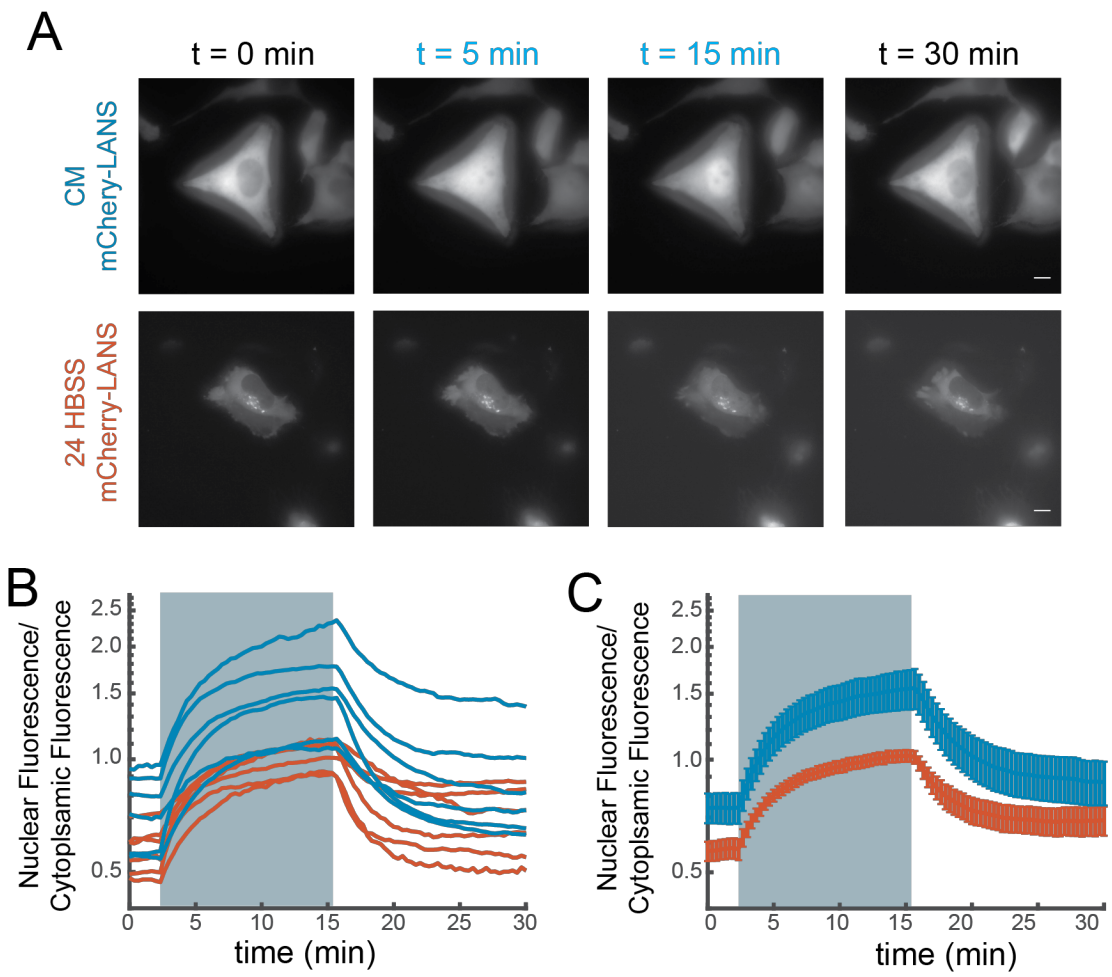

Figure 25. LANS Imaging Confirms that Nuclear-Cytoplasmic Transport is Altered in Starved Cells.

A) Representative images for light activation and reversion for HeLa cells in complete media (CM) and HBSS for 24 hours. *(Scale bar = 10 μm).* B) The change in the ratio of nuclear/cytoplasmic fluorescence in HeLa cells in CM (blue) and HBSS (red). The shaded region represents the time of blue light LANS activation. C) The average change in the ratio of nuclear/cytoplasmic fluorescence in HeLa cells in CM (blue) and HBSS (red) (n=6, mean reported ± SEM with error bars). The shaded region represents the time of blue light LANS activation. Note: bright areas in cytosol were excluded from analysis.

Karyopherin Content at NPCs

I was interested to see if the attenuated nuclear import was related to a different local concentration of karyopherins at the NPC after starvation. Using an antibody to kap1β, I quantified the amount of karyopherin detectable at each NPC using quantitative immunofluorescence. I wrote and applied an imaging processing algorithm (MATLAB) that detected individual NPCs and then measured the maximum intensity pixel for each NPC. There was an increase in kap1β present at the NPC of the starved cells compared to the fed cells (*p<0.001,* Figure 26). These results suggest that there is a change to the local characteristics of the NPCs when cells are starved that may lead to the decreased rates of cargo transport seen with the LANS construct.

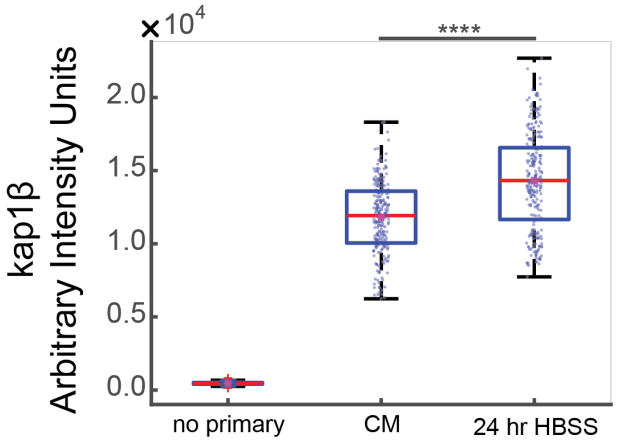

Figure 26. Kap1β Localization to the NPC Increases after Starvation.

Immunofluorescence microscopy of HeLa cells, stained with α-kap1β. Ten cells were imaged and 100 NPCs were selected from each these 10 cells with an automated algorithm. Each data point is plotted. (*blue boxes indicate quartiles, red bars indicate medians, magenta stars indicate means, red marks are outliers, Wilcoxon-Mann-Whitney, **** p<0.0001).*

Starvation Changes Orientation of Nups in HeLa Cells

Nup 133

Neither Nup133-mEGFP(-7) nor Nup133-mEGFP(-8) exhibited an orientational shift when starved.

Nup133-mEGFP(-7) has a *p/s* ratio of 1.281 ± 0.101 (n=300) in CM. When cells expressing this construct were starved for 24 hours in HBSS, the *p/s* ratio was 1.283 ± 0.107 (n=300). Nup133-mEGFP(-8) has a *p/s* ratio of 1.104 ± 0.079 (n=300) in CM. When starved for 24 hours in HBSS, the *p/s* ratio was 1.107 ± 0.083 (n=300). The *p/s* ratios of both constructs showed no statistically significant change after 24 hours in HBSS (Wilcoxon-Mann-Whitney, $p > 0.05$, Figure 27).

These results are consistent with the NPC retaining its orientation relative to the coverslip, meaning that the nuclear envelope is not itself becoming distorted.

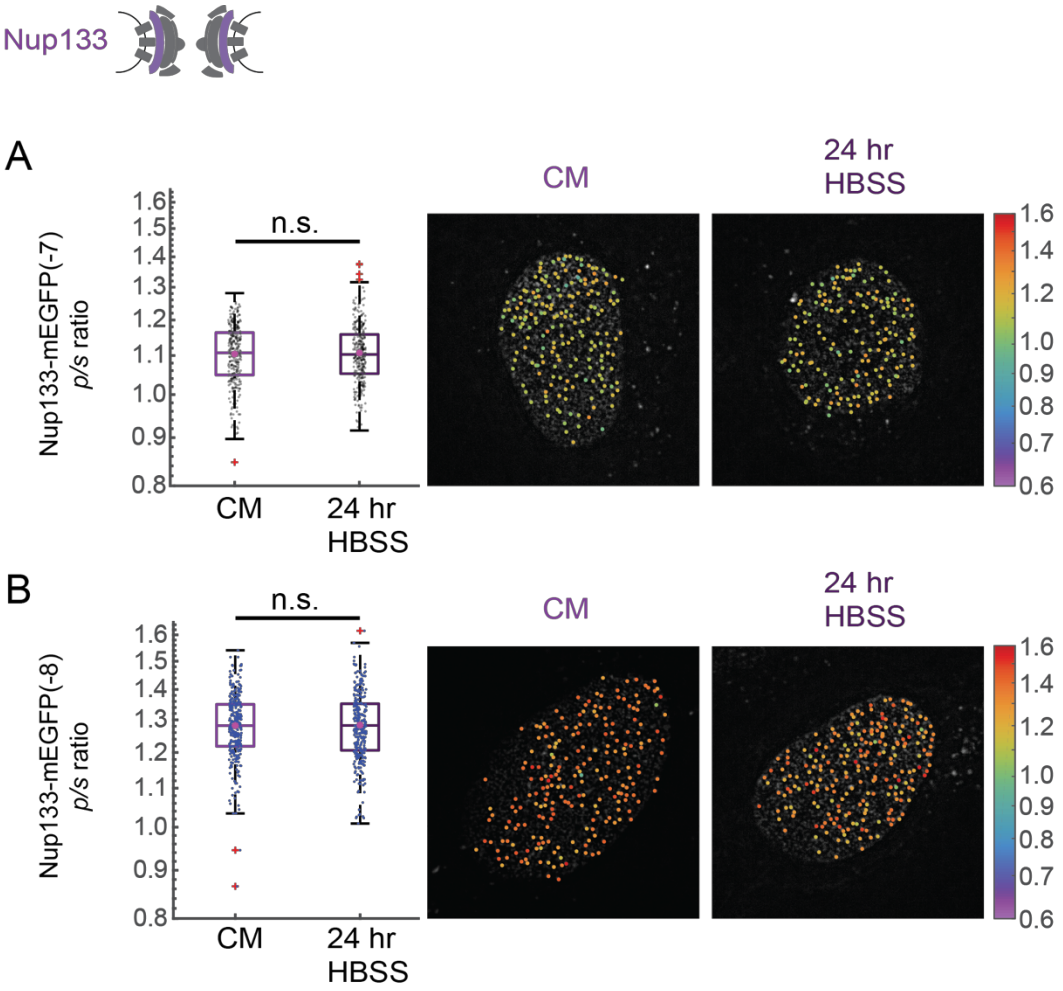

Figure 27. Nup133-mEGFP Fusion Proteins Do Not Shift in Orientation after Starvation.

After starvation, the *p/s* ratio of A) Nup133-mEGFP(-7) and B) Nup133-mEGFP(-8) were not statistically different (Wilcoxon-Mann-Whitney, n.s. no significance $p>0.05$). HeLa cells were imaged 48 hours post transfection. Cells were maintained in CM or starved for 24 hours in HBSS prior to imaging. *(n=300 NPCs, 10 cells, boxes indicate quartiles, center bars indicate medians, magenta stars indicate means, red marks are outliers)*. Representative images of cells are shown for cells in CM or HBSS, the color of the dot represents the *p/s* ratio of the NPC upon which it is superimposed.

Nup54

The orientation of both Nup54-mEGFP fusion proteins were shifted post-starvation, as measured with the *p/s* ratio.

The *p/s* ratio of Nup54-mEGFP494(0) was 0.990 ± 0.085 (n=300) before starvation and 0.863 ± 0.090 (n=300) after starvation. The *p/s* ratio of Nup54-mEGFP494(1) was 2.009 ± 0.197 (n=300) before starvation and was 1.868 ± 0.260 (n=300) after starvation. Both of these results were statistically significant (Wilcoxon-Mann-Whitney, $p < 0.0001$, Figure 28).

This shift in the *p/s* emission ratio after starvation reflects a shift in orientation of Nup54 with respect to the NPC, because the *p/s* ratios of Nup133 did not undergo a shift so the NPC as a whole is not changing orientation relative to the coverslip. The observed shift in orientation of the Nup54 fusion protein with respect to the NPC is consistent with a reorganization of the NPC inner ring post-starvation.

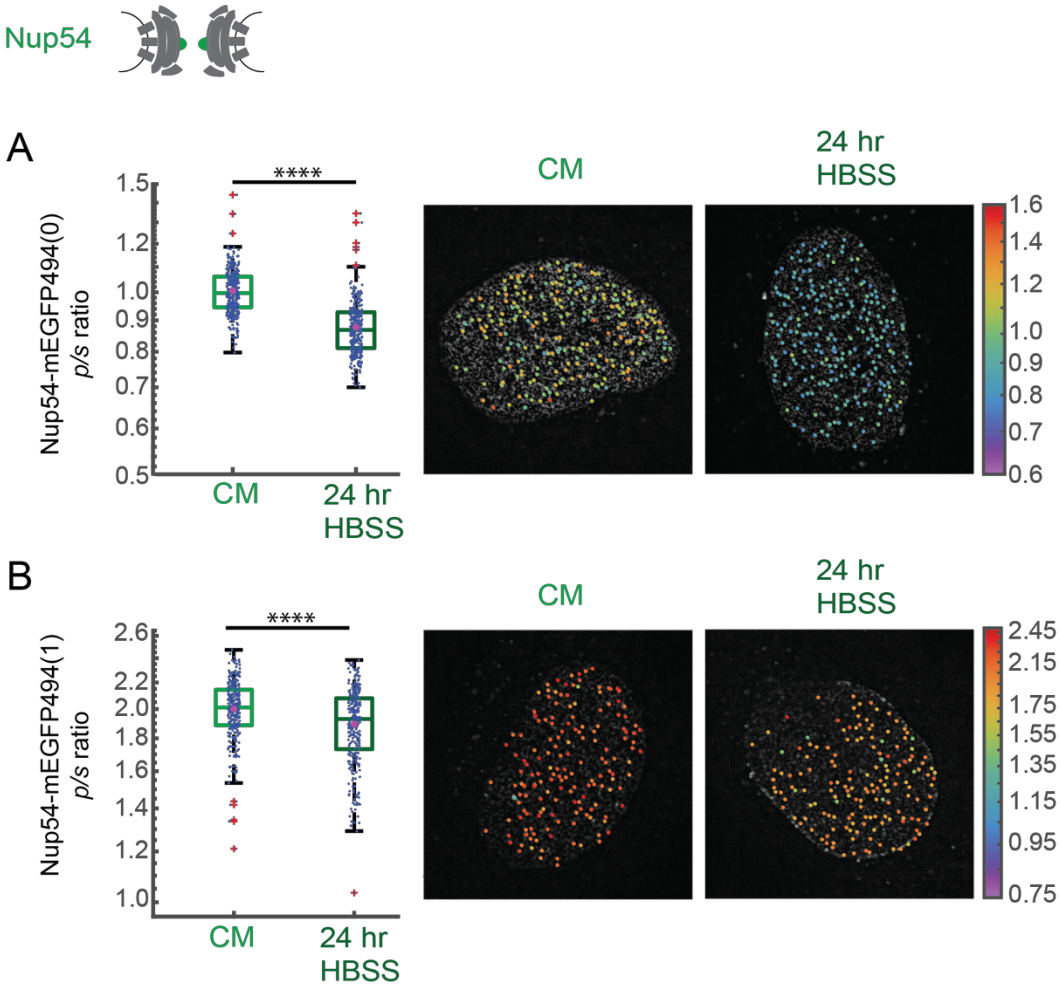

Figure 28. Nup54-mEGFP Fusion Proteins Shift in Orientation after Starvation.

After starvation, the *p/s* ratio of A) Nup54-mEGFP494(0) and B) Nup54-mEGFP494(1) were significantly different (Wilcoxon-Mann-Whitney, **** $p<0.0001$). HeLa cells were imaged 48 hours post transfection. Cells were maintained in CM or starved for 24 hours in HBSS prior to imaging. *(n=300 NPCs, 10 cells, boxes indicate quartiles, center bars indicate medians, magenta stars indicate means, red marks are outliers)*. Representative images of cells are shown for cells in CM or HBSS, the color of the dot represents the *p/s* ratio of the NPC upon which it is superimposed.

Nup93

For the Nup93-mEGFP(-4) construct, the pre-starvation *p/s* ratio was 1.303 ± 0.85. After starvation, the *p/s* ratio was 1.315 ± 0.97 (n=300). There was no statistical difference between these measurements (Wilcoxon-Mann-Whitney, $p > 0.05$, Figure 29).

The other Nup93 constructs exhibited slight orientational shifts after starvation. For the Nup93-mEGFP(-5) construct, the pre-starvation *p/s* ratio was 1.308 ± 0.072, (n=300). After starvation, the *p/s* ratio was 1.279 ± 0.117. The difference between these measurements was statistically significant (Wilcoxon-Mann-Whitney, $p < 0.01$, Figure 29).

For the final construct, Nup93-mEGFP(-6), the pre-starvation *p/s* ratio was 1.179 ± 0.075 (n=300). After starvation, this *p/s* ratio became 1.205 ± 0.0844 (n=300). This difference in *p/s* ratio was also statistically significant (Wilcoxon-Mann-Whitney, $p < 0.0001$, Figure 29).

Nup93 sits between the outer scaffold ring (including Nup133) and the inner channel ring of the NPC. Thus, the slight changes in orientation I observe under conditions of starvation might be this protein complex buffering a conformational change by the inner channel Nups, including Nup54.

Figure 29. Nup93-mEGFP Fusion Proteins Exhibit a Slight Shift in Orientation after Starvation.

Under starvation conditions, the *p/s* ratio did not shift for A) Nup93-mEGFP(-4) (Wilcoxon-Mann-Whitney, n.s. no significance $p > 0.05$), the *p/s* ratio shifted slightly for B) Nup93-mEGFP(-5) (Wilcoxon-Mann-Whitney, ** $p < 0.01$), and Nup93-mEGFP(-6) (Wilcoxon-Mann-Whitney, **** $p > 0.0001$). HeLa cells were imaged 48 hours post transfection. Cells were kept in CM or starved for 24 hours in HBSS *(n=300 NPCs, 10 cells, boxes indicate quartiles, center bars indicate medians, magenta stars indicate means, red marks are outliers)*. Representative images of cells are shown for cells in CM or HBSS, the color of the dot represents the *p/s* ratio of the NPC upon which it is superimposed.

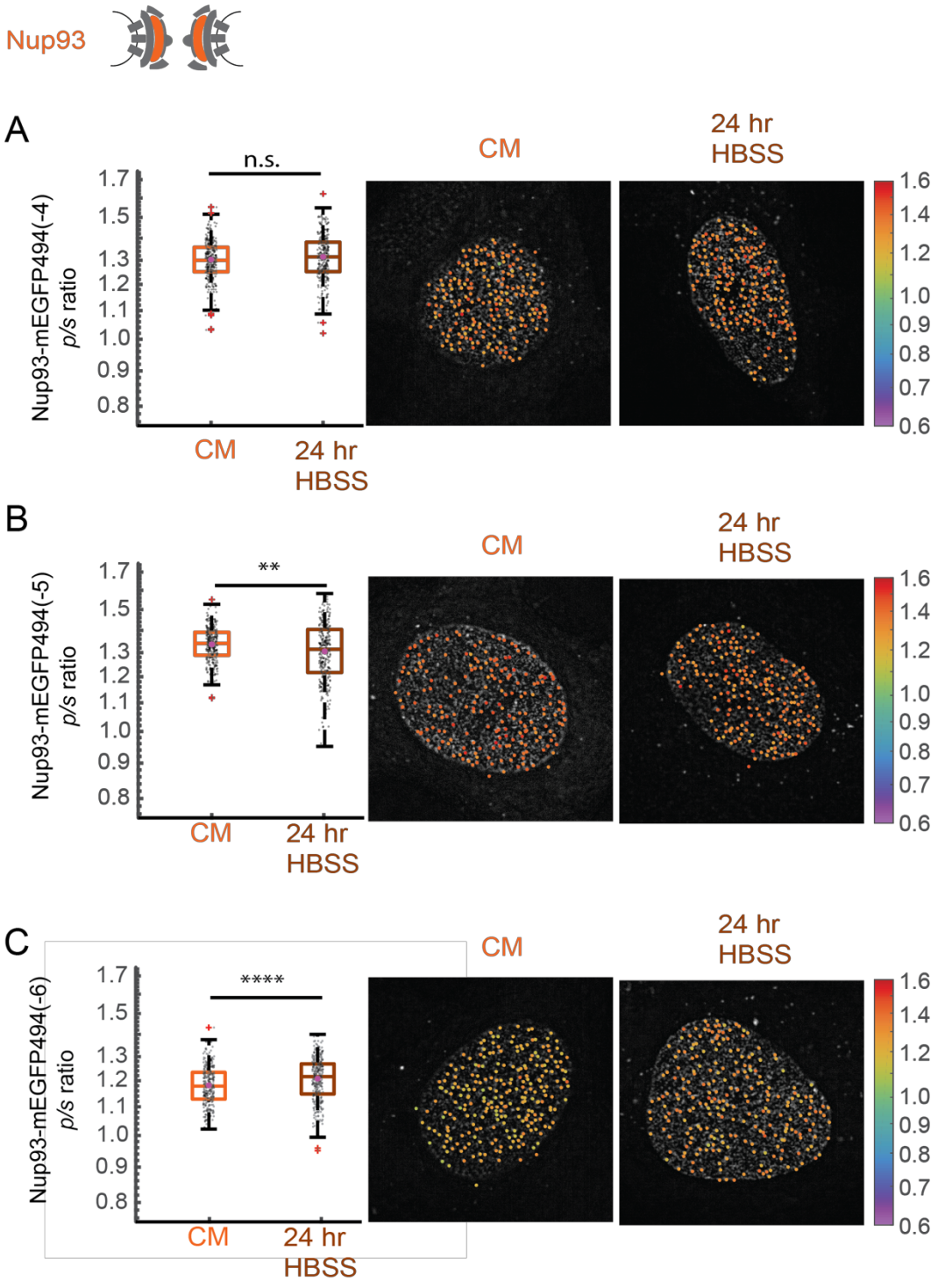
Nup93
A
n.s.
CM
24 hr HBSS
Nup93-mEGFP494(-4) p/s ratio
1.7
1.5
1.3
1.2
1.1
1.0
0.9
0.8
CM
24 hr HBSS
1.6
1.4
1.2
1.0
0.9
0.8
0.7
0.6
B
**
CM
24 hr HBSS
Nup93-mEGFP494(-5) p/s ratio
1.7
1.5
1.3
1.2
1.1
1.0
0.9
0.8
CM
24 hr HBSS
1.6
1.4
1.2
1.0
0.9
0.8
0.7
0.6
C
****
CM
24 hr HBSS
Nup93-mEGFP494(-6) p/s ratio
1.7
1.5
1.3
1.2
1.1
1.0
0.9
0.8
CM
24 hr HBSS
1.6
1.4
1.2
1.0
0.9
0.8
0.7
0.6

Starvation Changes Orientation of Nups in HAP1 CRISPR Cells

The CRISPR cell lines were starved for 24 hours under HBSS. The results of this experiment mimicked the results of the transiently transfected lines.

Nup133

The Nup133-mEGFP(-7) constructs did not exhibit a statistically significant change in orientation upon starvation (Wilcoxon-Mann-Whitney, $p > 0.05$, Figure 30A). Before starvation, the *p/s* ratio was 0.868 ± 0.078 (n=300) and after starvation the *p/s* ratio was 0.865 ± 0.067 (n=300). Similarly to the transiently transfected construct, the orientation of Nup133 did not exhibit a measurable shift after starvation.

Nup54

The Nup54 constructs exhibited a statistically significant change in orientation relative to the NPC (Figure 30B). The mean of the *p/s* ratio shifted from 0.759 ± 0.060 (n=300) before starvation to 0.729 ± 0.065 (n=300) after starvation (Wilcoxon-Mann-Whitney, $p < 0.0001$). The orientation of this construct shifted in the same direction as the transient transfection, which shifted from 0.990 ± 0.085 (n=300) before starvation to 0.863 ± 0.090 (n=300) after starvation (Figure 28). The similar direction of this shift suggests that the NPCs of the Hap1 CRISPR cells are behaving in a similar manner to the transient transfections, and changing orientation in the same direction. This result suggests that the mEGFP tagged Nups are not hindered from experiencing this orientational shift when both copies of the endogenous protein is replaced with a fluorescently labeled one.

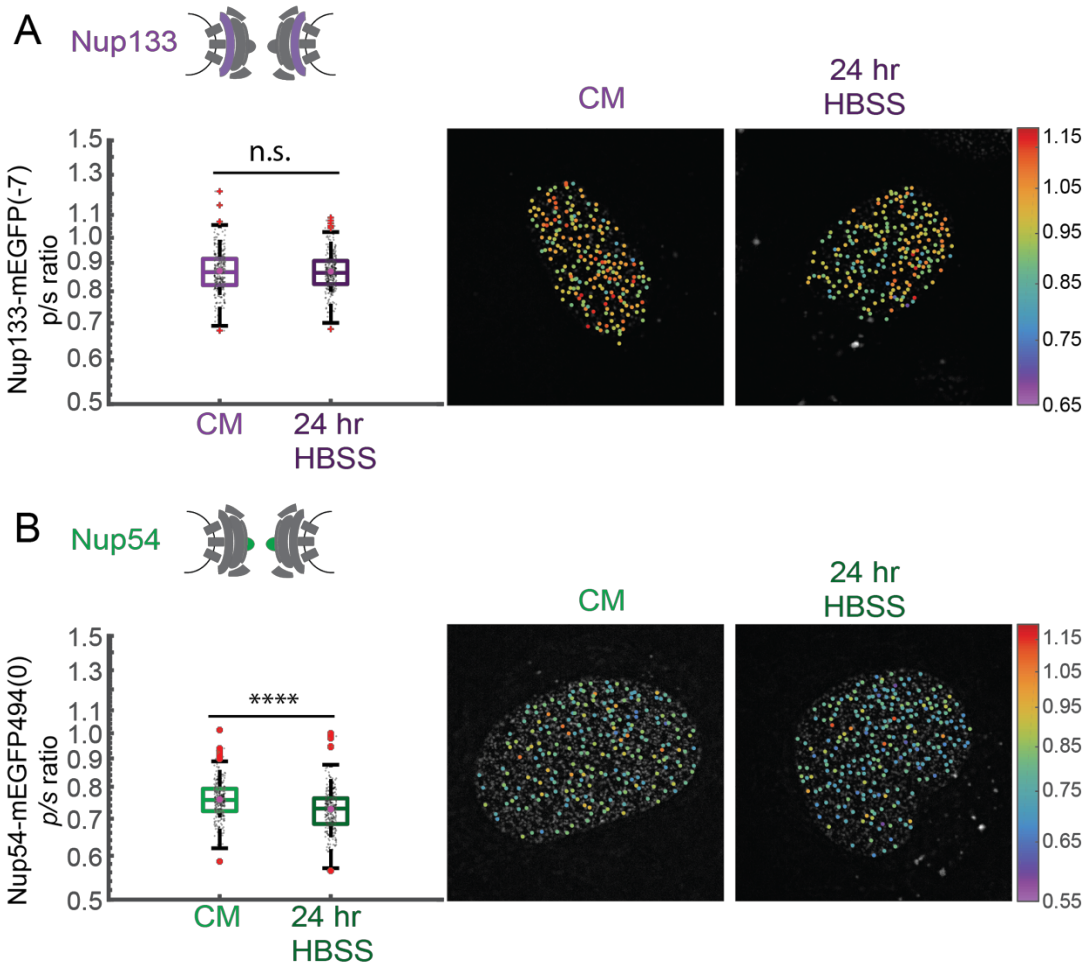

Figure 30. Nup54 Experiences Different Orientation After Starvation in the HAP1 CRISPR Cell Line

Under starvation conditions, A) The *p/s* ratio of Nup133-mEGFP(-7) did not shift (Wilcoxon-Mann-Whitney, ns=no significance $p > 0.05$). B) The *p/s* ratio of Nup54-mEGFP494(0) did shift (Wilcoxon-Mann-Whitney, **** $p < 0.0001$). HAP1 cells were kept in CM or starved for 24 hours in HBSS *(n=300 NPCs, 10 cells, boxes indicate quartiles, center bars indicate medians, magenta stars indicate means, red marks are outliers)*. Representative images of cells are shown for cells in CM or HBSS, the color of the dot represents the *p/s* ratio of the NPC upon which it is superimposed.

The results from the starvation experiments, both from the transient transfection and CRISPR cell line, suggest that under the altered physiological state of starvation, the inner ring of the NPC experiences a change in orientation of its components. Notably, it appears that the Nup133 does not experience a change of orientation. Any shift by Nup93 might be because this ring needs to be flexible to accommodate a conformational change by the inner channel Nups, including Nup54.

4.2 NPC Perturbation 2: Dominant Negative Ran

In order to disrupt active nuclear import and export, a dominant negative Ran (DN-Ran) protein was expressed in cells also expressing our conformational sensors. Ran is a GTPase that mediates active nuclear import and export (Moore, 1998). As summarized in Chapter 1 (page 7-9), Ran undergoes GTP hydrolysis upon reaching the cytosol. This hydrolysis causes a conformational change that causes the RanGTP-kap1β export complex to dissociate from the NPCs. The kap1β is thus released into the cytosol to interact with cargo and mediate NLS-driven cargo translocation and the Ran-gradient is maintained.

The Ran-Q69L mutant is unable to perform GTP hydrolysis, resulting in a blockage of Ran-dependent import and export (Bischoff, 1994). Thus, the Ran-Q69L is a dominant negative mutant. The inability to perform GTP hydrolysis leads to an increased accumulation of kaps at the NPC because they are unable to undock from the FG-Nups upon reentry into the cytosol (Hughes, 1994). When expressed in cells, RanQ69L blocks NLS-mediated cargo translocation. Notably, DN-RanQ69L is still capable of cargo import, but as it cannot perform hydrolysis, it cannot dissociate from the cytoplasmic face of the NPC (Schwoebel et al., 1998). This inability to dissociate leads to a sequestration of kap1β, resulting in a decreased pool of kaps available for cargo to bind to in the cytosol.

The Ran-T24L mutation is in the nucleotide binding pocket of the protein and reduces the ability to bind GTP. Mutations at this site are known to inhibit the NES-associated export of proteins when injected into the nucleus (Richards et al., 1997), but there have been contradictory studies as to whether mutations at this

location prevent import of NLS-tagged cargos (Carey et al., 1996; Dasso et al., 1994; Kornbluth et al., 1994; Palacios et al., 1996; Richards et al., 1997; Weis et al., 1996).

In order to characterize these DN-Ran proteins in my system, I tested the ability of cells expressing these constructs to transport the LANS construct upon stimulation with blue light.

Validation of DN-RAN Constructs

I transiently expressed the DN-RAN proteins conjugated to mTagBFP, a monomeric blue fluorescent protein and imaged them 24 hours post transfection. The BFP-RanQ69L protein was localized to the NPCs (note the punctate spots on the nucleus in Figure 31, left), while the BFP-RanT24N fusion protein exhibited a diffuse distribution in the nucleus (Figure 31, right).

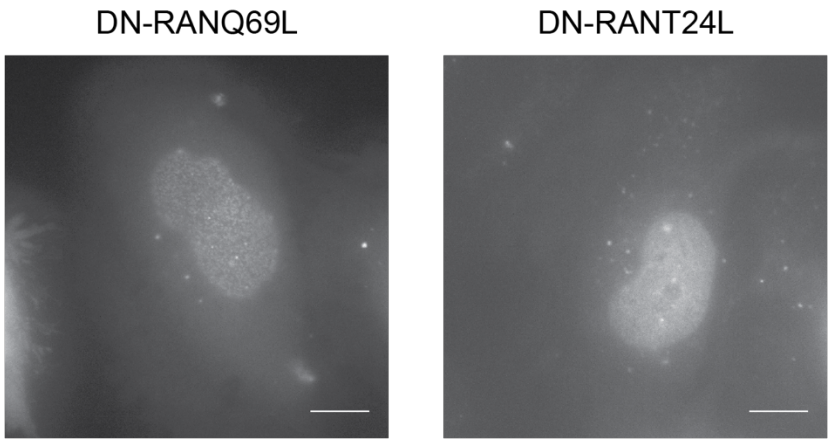

Figure 31. HeLa Cells Express DN-RAN-BFP constructs.

Cells were imaged 16 hours post transfection. DN-RanQ69L showed a punctate localization to the nucleus while DN-RANT24L showed a more diffuse localization to the nucleus. *(Scale Bar = 10 μm).*

To characterize the effect of the DN-RAN proteins, the intensity of kap1β at the NPCs was measured by quantitative IF in cells expressing fluorescent dominant-negative Ran proteins. In order to confirm transfection of the DN-Ran constructs in cells, I replaced the BFP protein (which has no published antibody) with an mCherry, and confirmed mCherry expression via immuno fluorescence.

When compared with the wild-type cells, there was much higher signal at the NPCs of cells that had been transfected with the mCherry-DN-Ran constructs, indicating that there was more kap1β localized to the NPCs for both of the constructs (Wilcoxon-Mann-Whitney, $p > 0.0001$, Figure 32). Because DN-Ran should block the kap1β from dissociating from the pore, these results confirmed that the dominant negative was acting upon our cells.

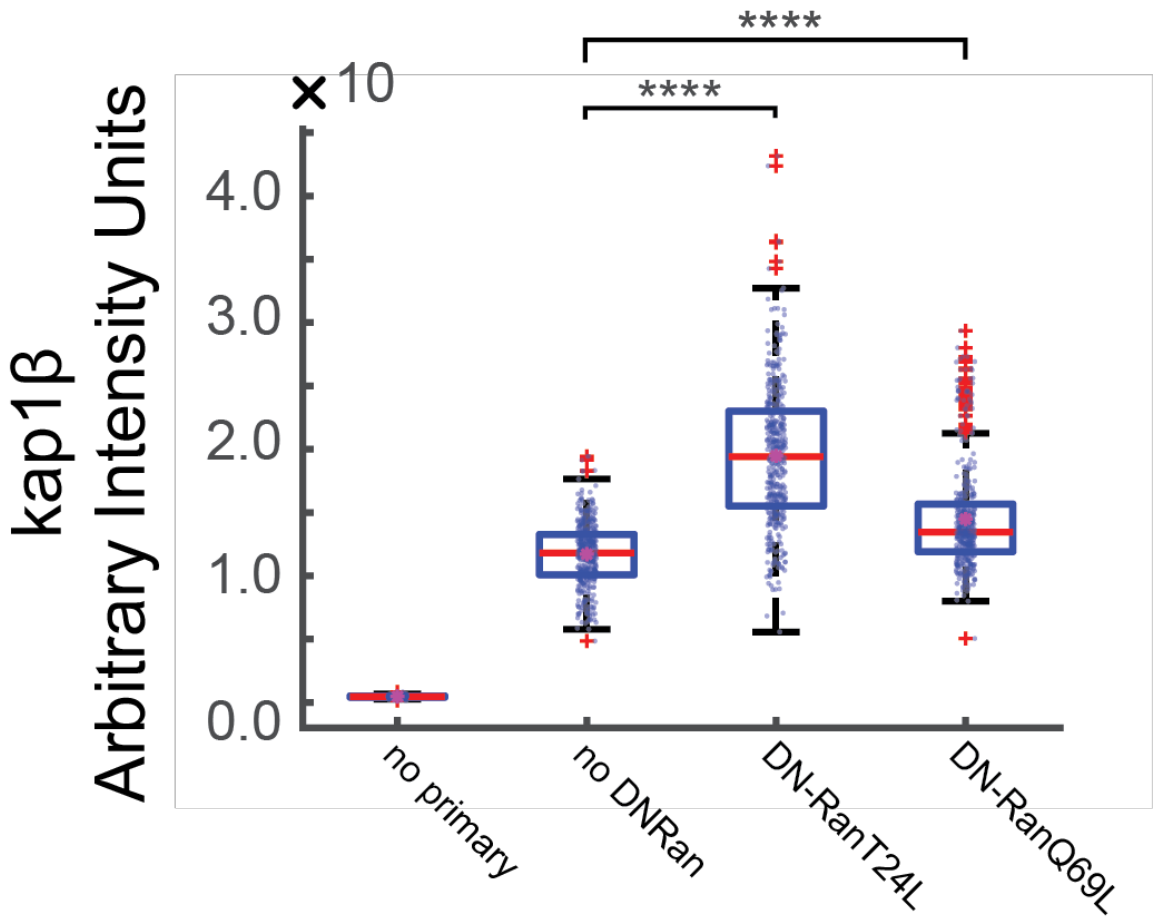

Figure 32. Kap1β localization to the NPC Changes after DN-Ran Transfection.

Immunofluorescence microscopy of HeLa cells, stained with α-kap1β. Ten cells were imaged. DN-Ran expression was confirmed and 100 NPCs were selected from each of 10 cells via an automated algorithm. Each data point is plotted. (Wilcoxon-Mann-Whitney, **** $p < 0.0001$).

The ability of the dominant-Ran transfected cells to transport the LANS construct were measured in transiently transfected HeLa cells. For both BFP-DN-RanT24L and BFP-DN-RanQ69L, a reduction in the nuclear exclusion of the construct was observed (Figure 33B-C). The rate and relative amount of import upon stimulation with blue light was also greatly attenuated with the transfection of the dominant negative.

Figure 33. Transient Expression of Ran Proteins that either Cannot Hydrolyze GTP or Cannot Bind GTP Reduces Nuclear Cytoplasmic Transport.

Nuclear-cytoplasmic transport was assayed by the LANS (light activated nuclear shuttle). A) Representative images for light activation and reversion for HeLa cells without transfection, with 16 hr transfection of BFP-DN-RanQ69L, and with 16 hr transfection of BFP-DN-RanT24L. *(Scale Bar = 10 μm).* B) The change in the ratio of nuclear/cytoplasmic fluorescence in control cells and cells expressing BFP-DN-Ran. The shaded region represents the time of blue light LANS activation. Each line represents a single cell (n=6). C) The average change nuclear/cytoplasmic fluorescence in HeLa cells in control cells and cells expressing BFP-DN-Ran (n=6, mean reported ± SEM with error bars). The shaded region represents the time of blue light LANS activation.

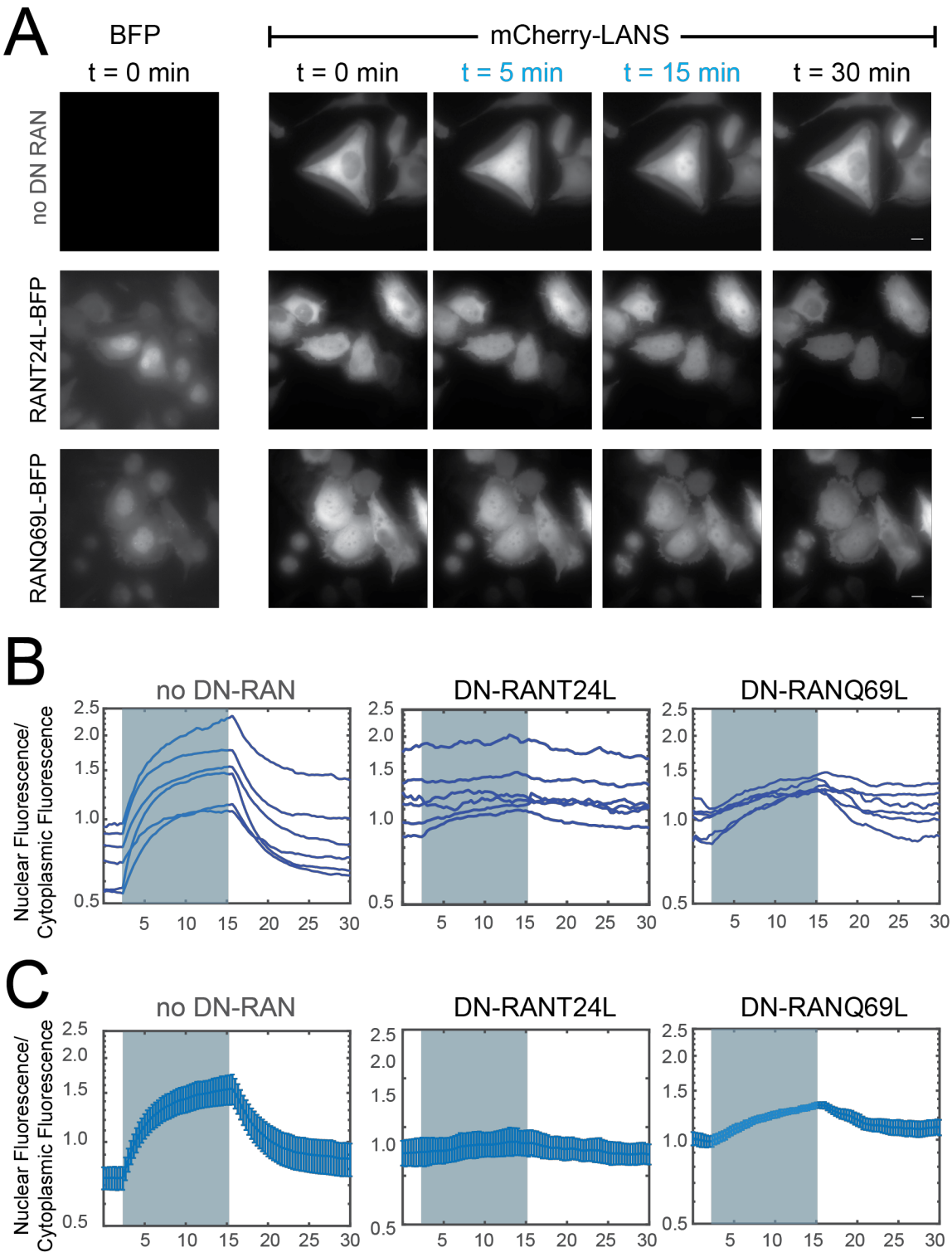
A
BFP
t = 0 min
mCherry-LANS
t = 0 min
t = 5 min
t = 15 min
t = 30 min
no DN RAN
RANT24L-BFP
RANQ69L-BFP
B
no DN-RAN
DN-RANT24L
DN-RANQ69L
Nuclear Fluorescence/
Cytoplasmic Fluorescence
2.5
2.0
1.5
1.0
0.5
5
10
15
20
25
30
C
no DN-RAN
DN-RANT24L
DN-RANQ69L
Nuclear Fluorescence/
Cytoplasmic Fluorescence

Nup54 Shifts Orientation after DN-Ran Transfection

When HeLa cells expressing the Nup orientational sensors were transfected with the DN-Ran, the Nup54-mEGFP sensors shifted in orientation, while the Nup133-mEGFP sensors did not.

Nup133

The Nup133-mEGFP(-7) construct was transfected and allowed to express for 48 hours. At 48 hours post-transfection, the BFP-DN-Ran constructs were transfected into the same cells. The cells that expressed both the Nup133-mEGFP(-7) and the BFP-DN-Ran were imaged 16 hours later (Figure 34). There was no orientation shift detected for cells that expressed the Nup133-mEGFP(-7). The cells that were not expressing a DN-Ran had a *p/s* ratio of 1.101 ± 0.078. The cells expressing DNRanT24L-BFP had a *p/s* ratio of 1.120 ± 0.090. The cells expressing DNRanQ69L had a *p/s* ratio of 1.09 ±0.091. No statistical difference was measured (Wilcoxon-Mann-Whitney, $p>0.05$).

Figure 34. Nup133-mEGFP(-7) Fusion Proteins Do Not Shift in Orientation after Transfection with DN-Ran.

After transfection with DN-Ran constructs, the *p/s* ratio did not shift for Nup133-mEGFP(-7) (Wilcoxon-Mann-Whitney, ns=no significance $p>0.05$). Cells were imaged 64 hours post transfection with Nup133-mEGFP(-7) and 16 hours post transfection with the DN-Ran *(n=300 NPCs, 10 cells, boxes indicate quartiles, center bars indicate medians, magenta stars indicate means, red marks are outliers,)*. Representative images of cells are shown for cells with transfection of DN-Ran, the color of the dot represents the *p/s* ratio of the NPC upon which it is superimposed.


Nup133

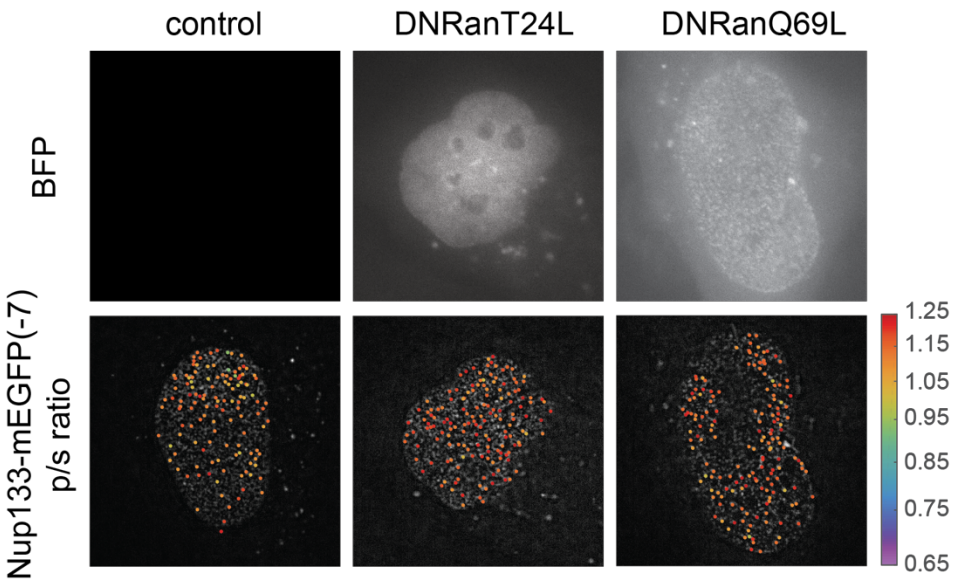
control
DNRanT24L
DNRanQ69L
BFP
Nup133-mEGFP(-7)
p/s ratio
1.25
1.15
1.05
0.95
0.85
0.75
0.65

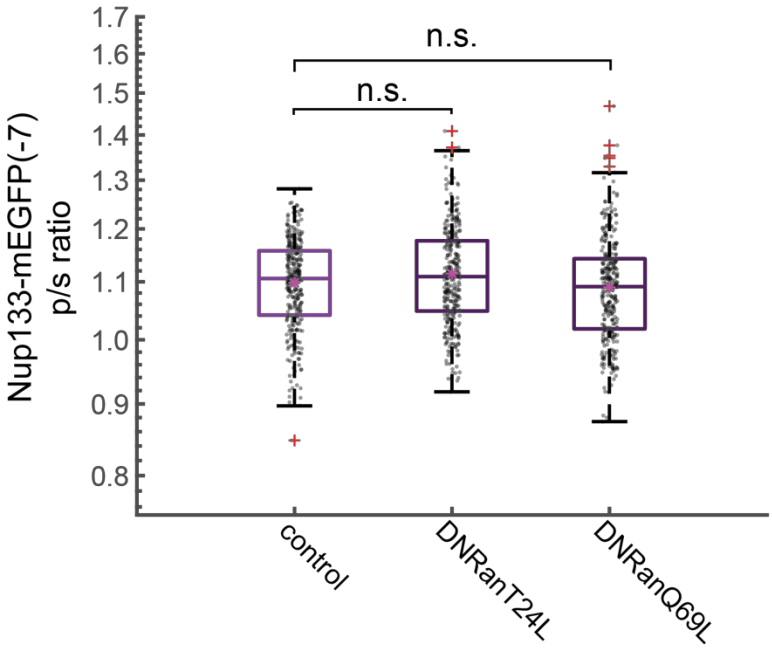
n.s.
n.s.
Nup133-mEGFP(-7)
p/s ratio
1.7
1.6
1.5
1.4
1.3
1.2
1.1
1.0
0.9
0.8
control
DNRanT24L
DNRanQ69L

Nup54

The Nup54-mEGFP494(0) construct was transfected and allowed to express for 48 hours. 24 hours post-transfection, the BFPDN-Ran constructs were transfected into the same cells. The cells that expressed both the Nup54-mEGFP494(0) and the BFP-DN-Ran were imaged 16 hours later (Figure 35) and *p/s* ratios were calculated. The Nup54-mEGFP(-5)-r5 construct that was not expressing the dominant-negative Ran had a *p/s* ratio of 0.946 ± 0.079 (n=300). The Nup54-mEGFP494(0) construct that was expressing the RanT24L had a *p/s* ratio of 1.024 ± 0.145 (n=300) and the Nup54-mEGFP494(0) construct that was expressing the RanQ69L construct had a *p/s* ratio of 1.059 ± 0.103 (n=300). These differences in *p/s* ratio were statistically significant (Wilcoxon-Mann-Whitney, $p < 0.0001$).

Figure 35. Nup54-mEGFP(0) Fusion Proteins Shift in Orientation after Transfection with DN-Ran.

After transfection with DN-Ran constructs, the *p/s* ratio shifts for Nup54-mEGFP(0) (Wilcoxon-Mann-Whitney, **** $p < 0.0001$). Cells were imaged 64 hours post transfection with Nup54-mEGFP(0) and 16 hours post transfection with the DN-Ran *(n=300 NPCs, 10 cells, blue boxes indicate quartiles, red bars indicate medians, magenta stars indicate means, red marks are outliers,)*. Representative images of cells are shown for cells with transfection of DN-Ran, the color of the dot represents the *p/s* ratio of the NPC upon which it is superimposed.

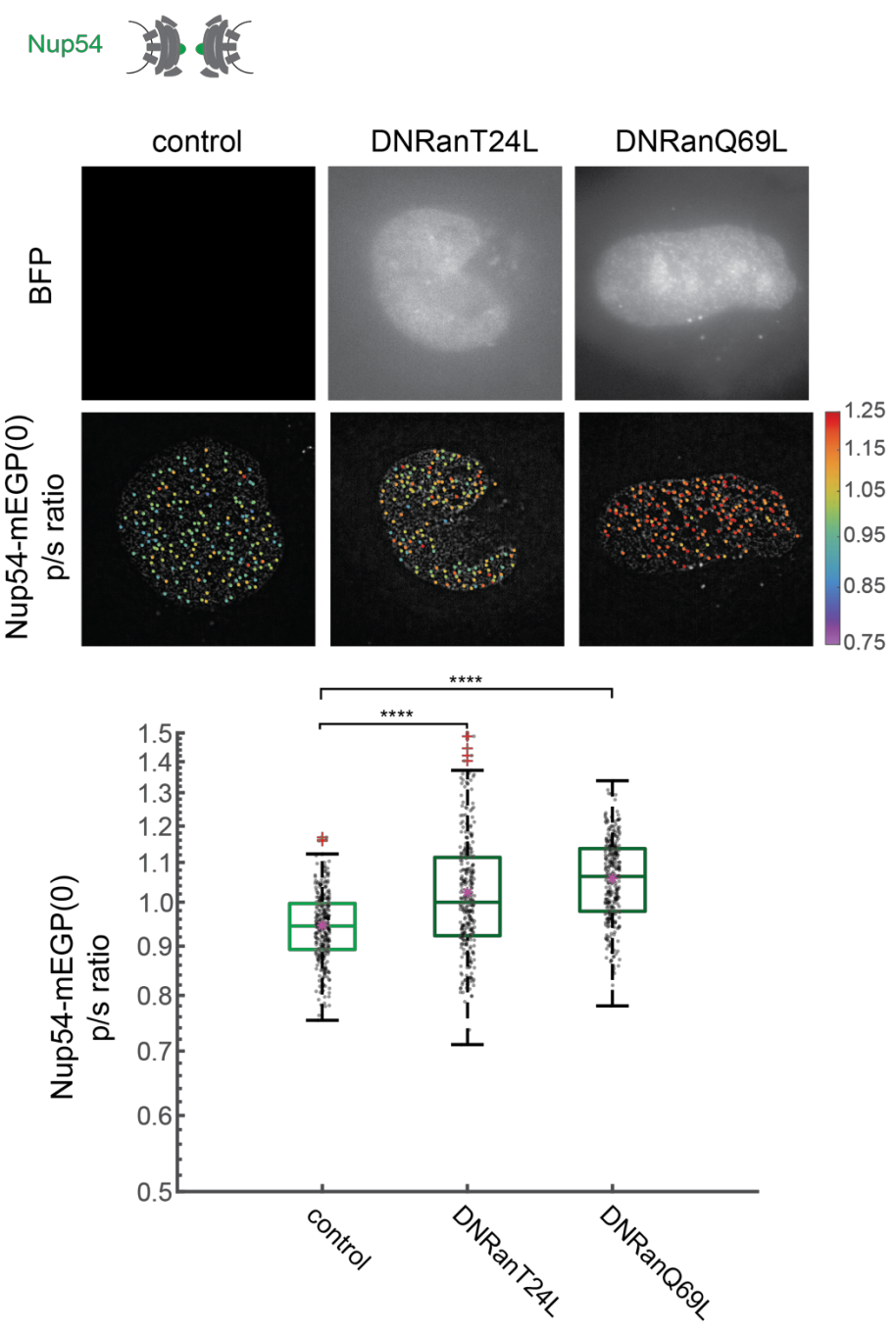
Nup54
control
DNRanT24L
DNRanQ69L
BFP
Nup54-mEGP(0)
p/s ratio
1.25
1.15
1.05
0.95
0.85
0.75
****
****
1.5
1.4
1.3
1.2
1.1
1.0
0.9
0.8
0.7
0.6
0.5
Nup54-mEGP(0)
p/s ratio
control
DNRanT24L
DNRanQ69L

The results of the dominant negative experiments suggest that after NLS-driven cargo transport is halted, the inner channel ring of the NPC experiences a rearrangement of its components. Nup133 does not appear to undergo a rearrangement under these conditions.

Fluctuations in Nups After DN-Ran Transfection

After treatment with DN-Ran, the fluctuations in the Nup54(0) construct decreased for the DN-RanQ69L construct, but not for the DN-RanT24L (Figure 36). No changes were observed for the Nup133(-8) construct. This decrease in fluctuations is coincident with a decrease in transport (Figure 33).

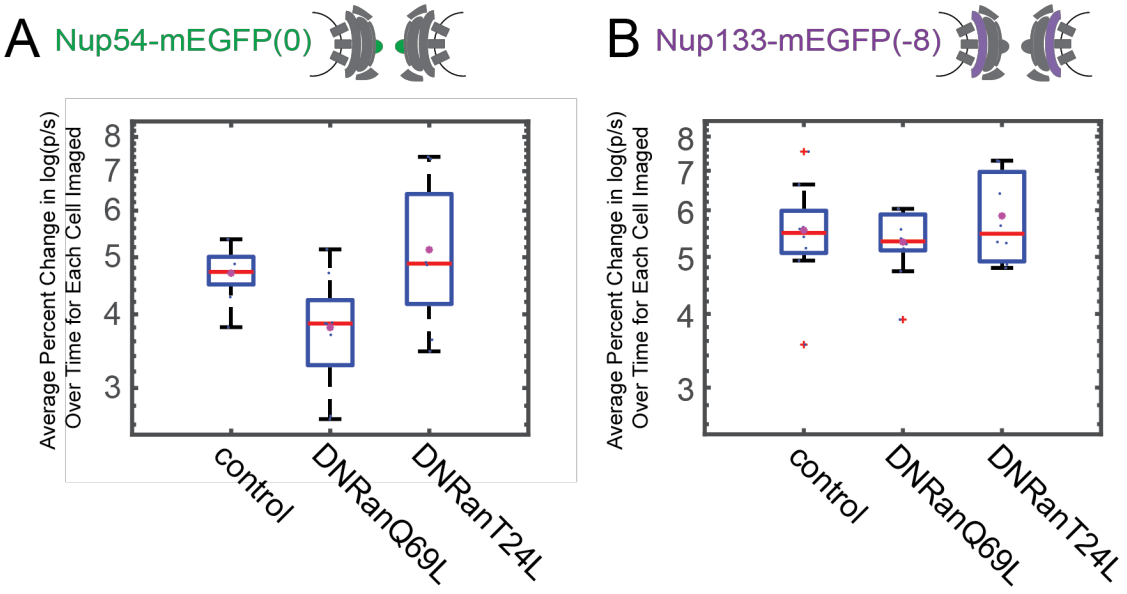

Figure 36. The Fluctuations in the *p/s* ratio of Nup54-mEGFP(0) Fusion Proteins are Attenuated when Transport is Reduced by DN-RanQ69L.

After transfection with DN-Ran constructs, the fluctuations over time of the *p/s* ratio of Nup54-mEGFP(0) were attenuated, but the fluctuations over time of the *p/s* ratio for the Nup133-mEGFP were not attenuated. Cells were imaged 16 hours post transfection with the DN-Ran *(n=10 cells, blue boxes indicate quartiles, red bars indicate medians, magenta stars indicate means, red marks are outliers)*.

4.3 NPC Perturbation 3: Cytosol Removal

Digitonin permeabilization is a technique that allows for the permeabilization of the plasma membrane but leaves the nuclear membrane intact (Adam et al., 1992; Cassany and Gerace, 2008). Digitonin is a detergent that primarily interacts with cholesterol. Because cholesterol is present at a higher concentration in the plasma membrane than the nuclear envelope, it is possible to incubate cells with a concentration of digitonin that maintains the integrity of the nuclear envelope while permeabilizing the plasma membrane. With this technique, one can then wash out the cytosol and introduce various import or export factors, cargoes, inhibitors, and metabolites directly to the nuclear periphery.

In order to verify that I am observing selective permeabilization of the plasma membrane while maintaining the integrity of the nuclear membrane, I used R-phycoerythrin (Santa Cruz), a red fluorescent protein produced by red algae that is approximately ~250 KDa in size. This fluorescent protein serves as a control for cell and nuclear permeability. When cells are not permeabilized, the R-phycoerythrin is excluded from the cytoplasm. When cell are permeabilized but the nucleus is intact, the R-phycoerythrin is excluded from only from the nucleus but freely explores the space peripheral to the nucleus. When both the plasma membrane and the nuclear envelope are permeabilized, the R-phycoerythrin can enter the nuclear space and forms a bright accumulation in the nuclear space (Figure 37).

The integrity of the nuclear membrane of all cells which were digitonin permeabilized was verified at the end of the experiment by addition of R-phycoerythrin.

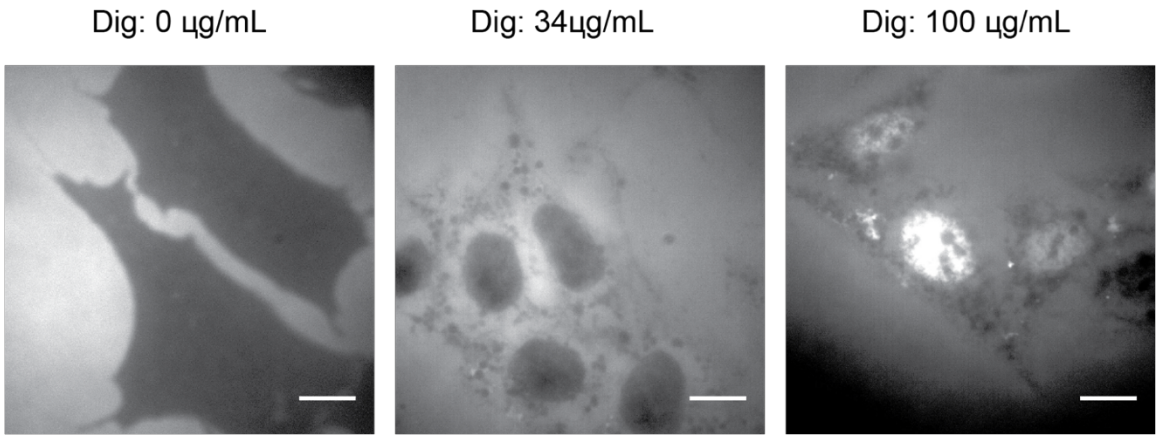

Figure 37. Digitonin Permeabilization State can be Monitored with R-phycoerythrin.

Cells were imaged after digitonin permeabilization protocol with 0 ug/mL, 34 ug/mL, and 100 ug/mL digitonin. *(Scale Bar = 10 μm).*

Conformational Sensors for Nups do not Change Orientation after Cytosol Removal

The first test performed with digitonin permeabilization was cytosol removal. Cells were imaged post-permeabilization in a 37°C transport buffer that was maintained at osmotic equilibrium (details in Methods, page 177). In this state, the nuclei should maintain integrity throughout the imaging session. For a cell be included in the analysis, the integrity of the nuclear envelope was assayed by imaging with the addition of R-phycoerythrin at the end of the imaging session. Kaps that are associated with the NPCs at the time of permeabilization should remain associated with the NPCs because the loss of cytosol means there are no cytosolic factors to trigger their dissociation from the NPC. Without cytoplasmic factors, the Ran recycling system that provides the potential energy for the transport of cargo will be broken, and NLS-driven cargo transport will cease.

Using the CRISPR Nup133-mEGFP(-7) cell line, I permeabilized the cells and observed no statistical difference in orientation (Figure 38A). Nup-mEGFP(-7) had a *p/s* ratio of 0.876 ± 0.075 (n=300) in unpermeabilized cells and a *p/s* ratio of 0.886 ± 0.087 (n=300) in permeabilized cells. Nup54-mEGFP(0) had a *p/s* ratio of 0.793 ± 0.075 (n=300) in unpermeabilized cells and a *p/s* ratio of 0.790 ± 0.085 (n=300) in permeabilized cells. Neither difference was statistically significant (Wilcoxon-Mann-Whitney, $p > 0.05$, Figure 38).

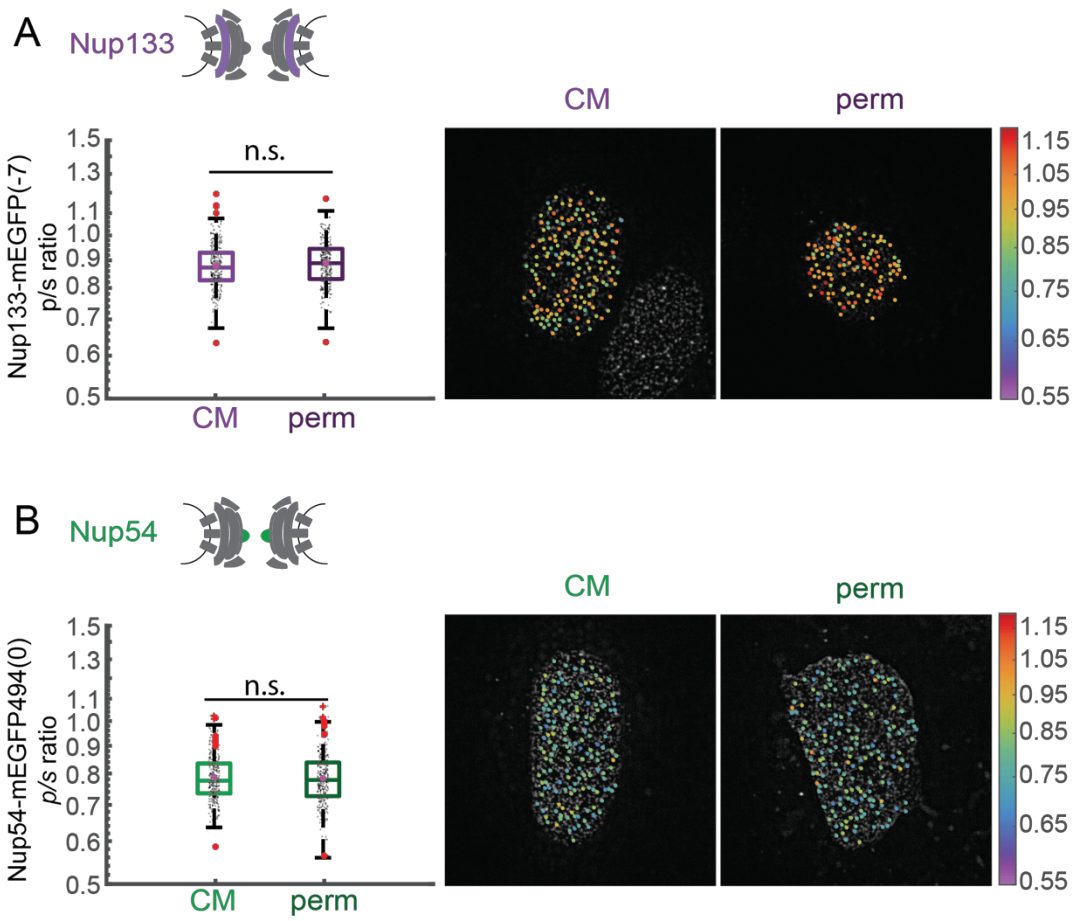

Figure 38. After Removal of Cytosol, No Conformational Change was Observed in Nup133 or Nup54.

After cells were permeabilized with digitonin and cytosol was removed, neither the A) Nup133-mEGFP(-7) nor the B) Nup54(0) construct experienced a shift in orientation (Wilcoxon-Mann-Whitney, n.s. no significance p>0.05). *(n=300 NPCs, 10 cells, blue boxes indicate quartiles, red bars indicate medians, magenta stars indicate means, red marks are outliers)*. The color of the dot represents the *p/s* ratio of the NPC upon which it is superimposed.

4.5. Cargo Perturbation 5: Cargo Removal (Ran-GTP)

Ran-GTP Added to the Nuclear Periphery Causes Disassociation of Kap1β

After permeabilization, much of the cargo remains conjugated to the NPC. I transiently transfected kap1β-mCherry to serve as a proxy for cargo. Once cells are permeabilized, kap1β-mCherry remains associated with the nuclear envelope for over 60 min (Figure 39, top). If Ran-GTP is introduced to the nuclear periphery, the NPC will lose directionality and all cargo will dissociate from the NPC. I purified Ran, and loaded it with GTP, and then introduced Ran-GTP to the nuclear periphery in order to cause cargo dissociation (Figure 39, bottom).

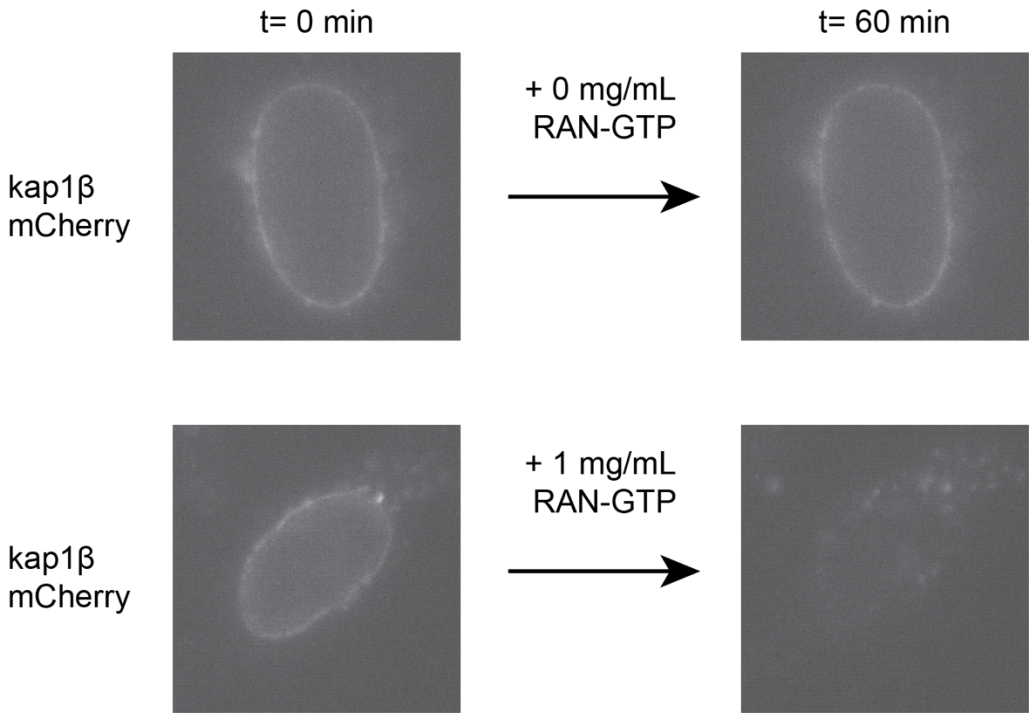

Figure 39. Ran-GTP leads to the disassociation of cargo complexes from the NPCs.

Cells were permeabilized and incubated with 1 mg/mL Ran-GTP. After 1 hour, cells were imaged. mCherry signal at the nuclear periphery was reduced, showing a decrease in the cargo content at the nuclear envelope.

Removing Cargo Causes Nup54 to Change Orientation

Cells transiently transfected with Nup133-mEGFP(-8), and Nup54-mEGFP(0) were permeabilized and incubated with Ran-GTP. Before incubation with Ran-GTP, Nup133-mEGFP(-8) had a *p/s* ratio of 1.259 ± 0.080 (n=70), after the incubation Nup133-mEGFP(-8) had a *p/s* ratio of 1.289 ± 0.100 (n=70). There was no significant difference (Figure 40A, Wilcoxon-Mann-Whitney, $p > 0.05$).

In contrast, the *p/s* ratio of Nup54-mEGFP494(0) decreased. Before incubation with Ran-GTP, Nup54-mEGFP494(0) had a *p/s* ratio of 0.908 ± 0.062 (n=70), after the incubation Nup54-mEGFP494(0) had a *p/s* ratio of 0.864 ± 0.070 (n=70). This difference was significant (Figure 40B, Wilcoxon-Mann-Whitney, $p < 0.0001$).

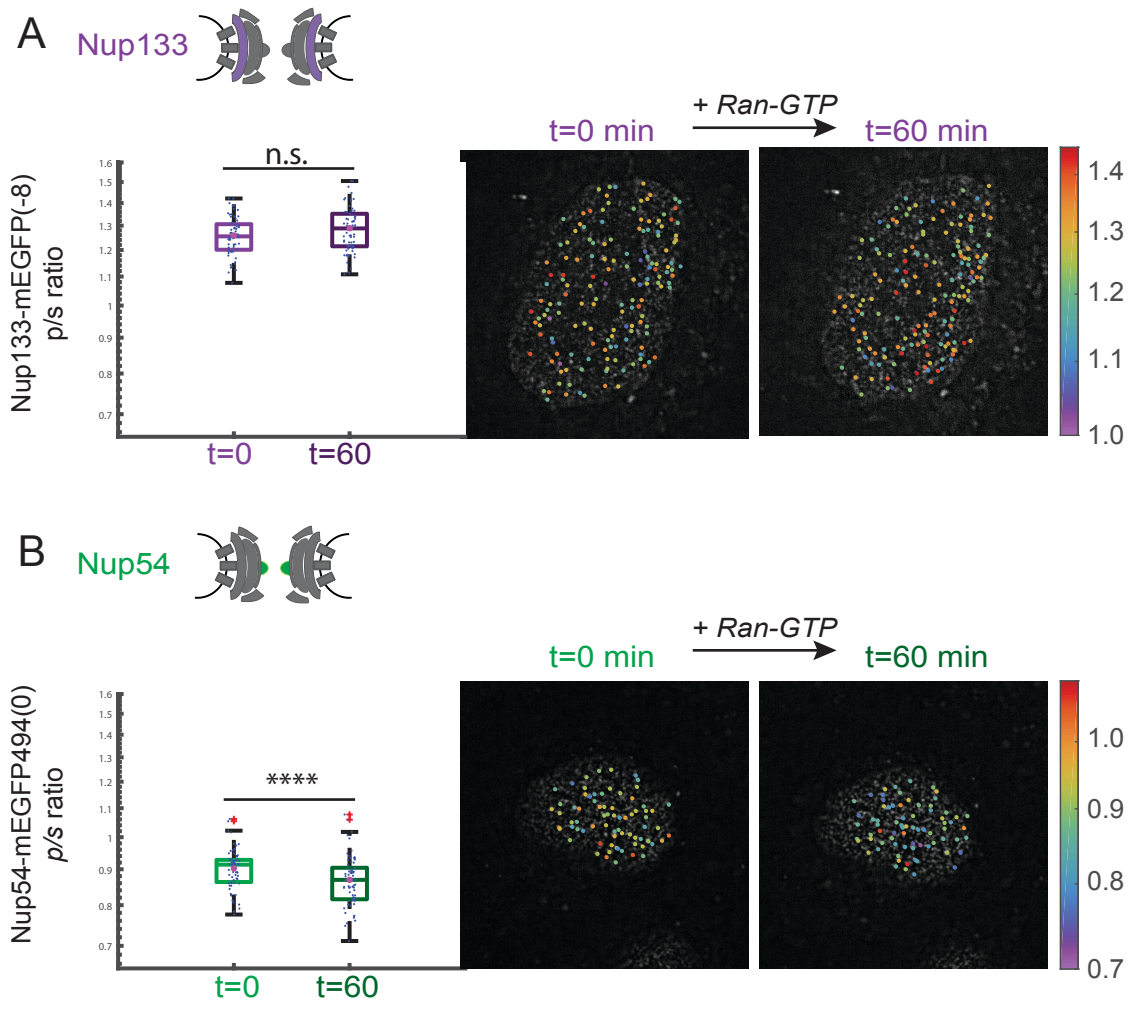

Figure 40. Dissociation of Cargo Complexes Induces a Shift in the *p/s* Orientation of Nup54

After removal of cargo, A) The *p/s* ratio of Nup133-mEGFP(-7) did not shift (Wilcoxon-Mann-Whitney, ns=no significance $p > 0.05$). B) The *p/s* ratio of Nup54-mEGFP494(0) did shift (Wilcoxon-Mann-Whitney, **** $p < 0.0001$). Cells were permeabilized and imaged (t = 0 min), and then incubated with 1 mg/mL Ran-GTP. After 1 hour, cells were imaged again (t = 60 min). *(n=70 NPCs, 1 cell, blue boxes indicate quartiles, red bars indicate medians, magenta stars indicate means, red marks are outliers)*. Images of cells are shown for cells before and after cargo removal, the color of the dot represents the *p/s* ratio of the NPC upon which it is superimposed.

4.6. Cargo Perturbation 6: FG-Nup Crosslinking with WGA

The FG-domains of Nup62 and Nup54 are modified by O-linked glycosyl groups. O-linked glycosyl groups bind to wheat germ agglutinin (WGA). After WGA binds, cargo can still bind to the NPC, but transport is inhibited (Finlay et al., 1987; Shulga et al., 1996). Previously, our lab has observed altered dynamics in the FG-Nup domains proximal to the O-linked glycosyl groups dynamics of Nup54 and Nup62 after the binding of WGA (Atkinson et al., 2013). When I permeabilize cells and add fluorescently-tagged WGA to the exterior of cells, I observe WGA accumulation near the NPCs (Figure 41).

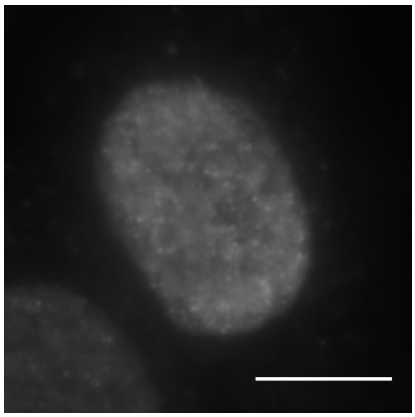

Figure 41. WGA Associates with the Nuclear Envelope

Cells were imaged after digitonin permeabilization and incubation with 2 mg/mL WGA (5% labeled with Alexa647). *(Scale Bar = 10 μm).*

FG-Nup Crosslinking Causes Nup54 to Change Orientation

Using the CRISPR Nup133-mEGPF(-7) cell line, I permeabilized the cells and then incubated them with WGA. In unincubated cells, Nup133-mEGFP(-7) has a *p/s* ratio of 0.916 ± 0.85 (n=300). In cells that were incubated with WGA, Nup133-mEGFP(-7) has a *p/s* ratio of 0.909 ± 0.080 (n=300). There was no observed statistical differences in these *p/s* ratios (Figure 42A, Wilcoxon-Mann-Whitney, $p > 0.05$). In unincubated cells, Nup54-mEGFP(0) has a *p/s* ratio of 0.787 ± 0.083 (n=300). In cells that were incubated with WGA, Nup54-mEGFP(0) has a *p/s* ratio of 0.840 ± 0.080 (n=300). This increase was observed to be statistically significant (Figure 42B, Wilcoxon-Mann-Whitney, $p < 0.0001$).

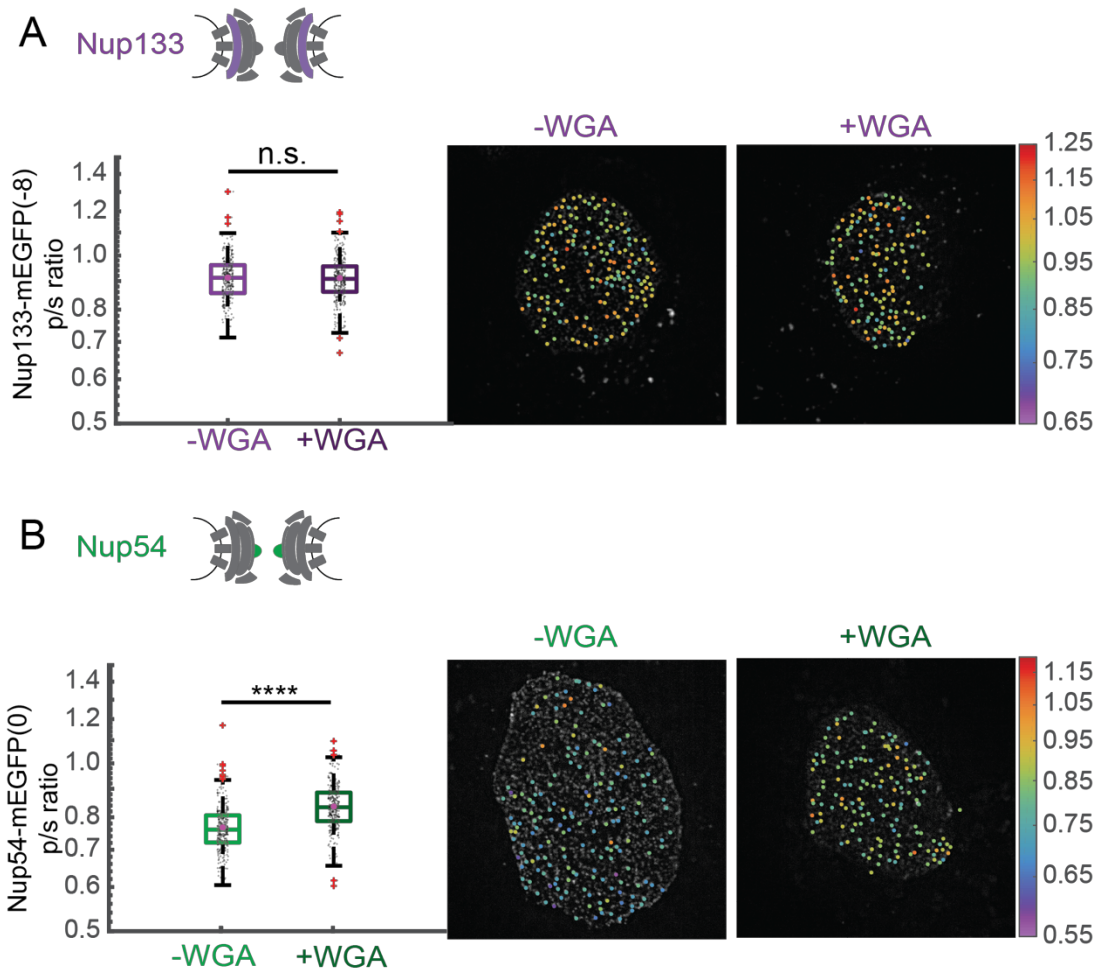

Figure 42. WGA Crosslinking Induces Conformational Change in Nup54 in Hap1 Cells

After WGA crosslinking, A) The *p/s* ratio of Nup133-mEGFP(-7) did not shift (Wilcoxon-Mann-Whitney, ns=no significance $p > 0.05$). B) The *p/s* ratio of Nup54-mEGFP494(0) did shift (Wilcoxon-Mann-Whitney, **** $p < 0.0001$). Cells were permeabilized and incubated with 2 mg/mL WGA. After 15 minutes, cells were imaged *(n=300 NPCs, 10 cells, blue boxes indicate quartiles, red bars indicate medians, magenta stars indicate means, red marks are outliers)*. Representative images of cells are shown for cells without WGA or with WGA, the color of the dot represents the *p/s* ratio of the NPC upon which it is superimposed.

4.7 Nup62 'finger' Domain is Also Reorganized upon Starvation

In order to test if the orientational shifts in Nup54 I observed caused a spatial reorganization of the Nup62 complex, I attempted to measure the proximity of the 'finger' regions of Nup62 (Amino Acid: 290). This region has been proposed to be an elongated region that can interact with a loosely structured region of Nup54 that is between the coiled-coiled anchor and the flexible FG domain (Chug et al., 2015; Solmaz et al., 2013).

I attempted to measure proximity of these regions in individual NPCs with Förster resonance energy transfer (FRET). FRET is a technique that can be used to measure the proximity of two fluorophores (usually used over distances of 1-10nm). When two fluorophores with overlapping donor emission and acceptor excitation spectra come very close to each other, a nonradiative energy transfer can occur from donor to acceptor.

FRET results in a suppressed emission in the donor wavelength. If then the acceptor is photobleached, it will no longer be able to accept the energy transfer, and the donor emission will increase.

I placed FRET sensors (mEGFP and mCherry) in the 'finger' regions of Nup62 region and co-transfected both sensors into HeLa cells (Figure 43A). I measured FRET with acceptor photobleaching and quantified FRET efficiency as:

$$FRET_{eff} = \frac{\left(I_{post} - I_{pre}\right)}{I_{post}}$$

Where I_{post} is the fluorescence intensity of the donor after acceptor photobleaching and I_{pre} is the intensity of the donor before acceptor photobleaching. The FRET efficiency is considered positive when $I_{post} > I_{pre}$. I co-transfected cells with Nup62-mEGFP and Nup62-mCherry and images were processed via an automated algorithm (MATLAB).

Cells that were starved in HBSS for 24 hours, which reduces import (Figure 25), exhibited increased FRET between Nup62 'finger' domains (Figure 43B) over cells that were kept in CM. 37% of the NPCs measured in starved cells exhibited positive FRET, while only 15% of the NPCs measured in the cells in CM exhibited positive FRET.

Figure 43. FRET between Nup62 'Finger' Domains Increases after Starvation

Under starvation conditions, FRET increased between Nup62 'finger' domains. A) Cartoon of Nup62 FRET probe labelling scheme. B) FRET efficiency for HeLa cells were imaged 48 hours post transfection. Cells were kept in CM or starved for 24 hours in HBSS *(n=300 NPCs, 10 cells, blue boxes indicate quartiles, red bars indicate medians, magenta stars indicate means, red marks are outliers, **** p<0.0001, Wilcoxon-Mann-Whitney)*.

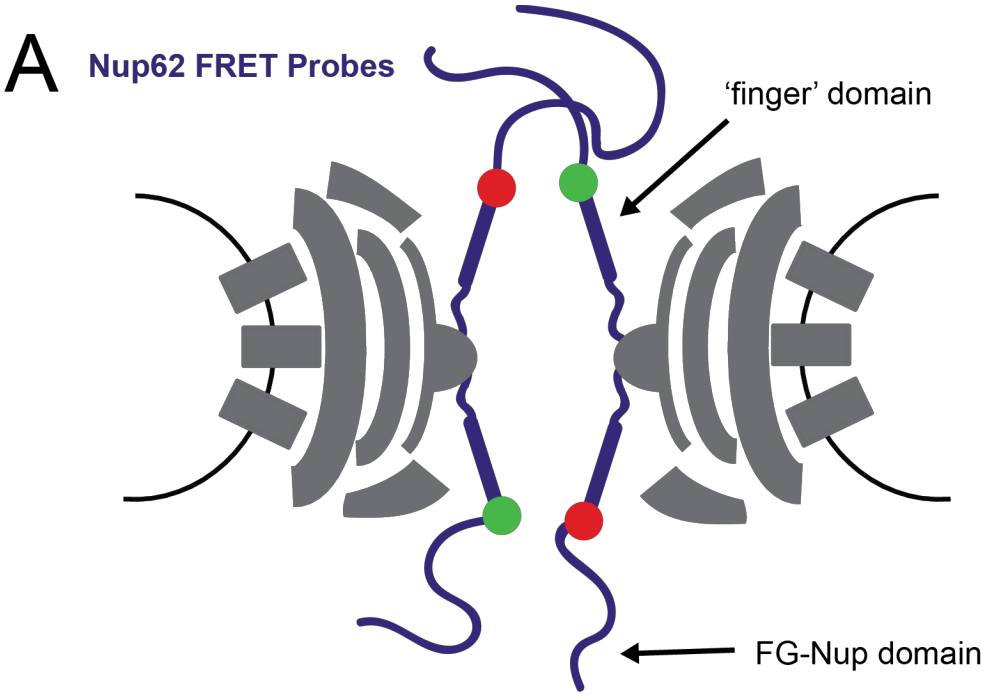
A
Nup62 FRET Probes
'finger' domain
FG-Nup domain

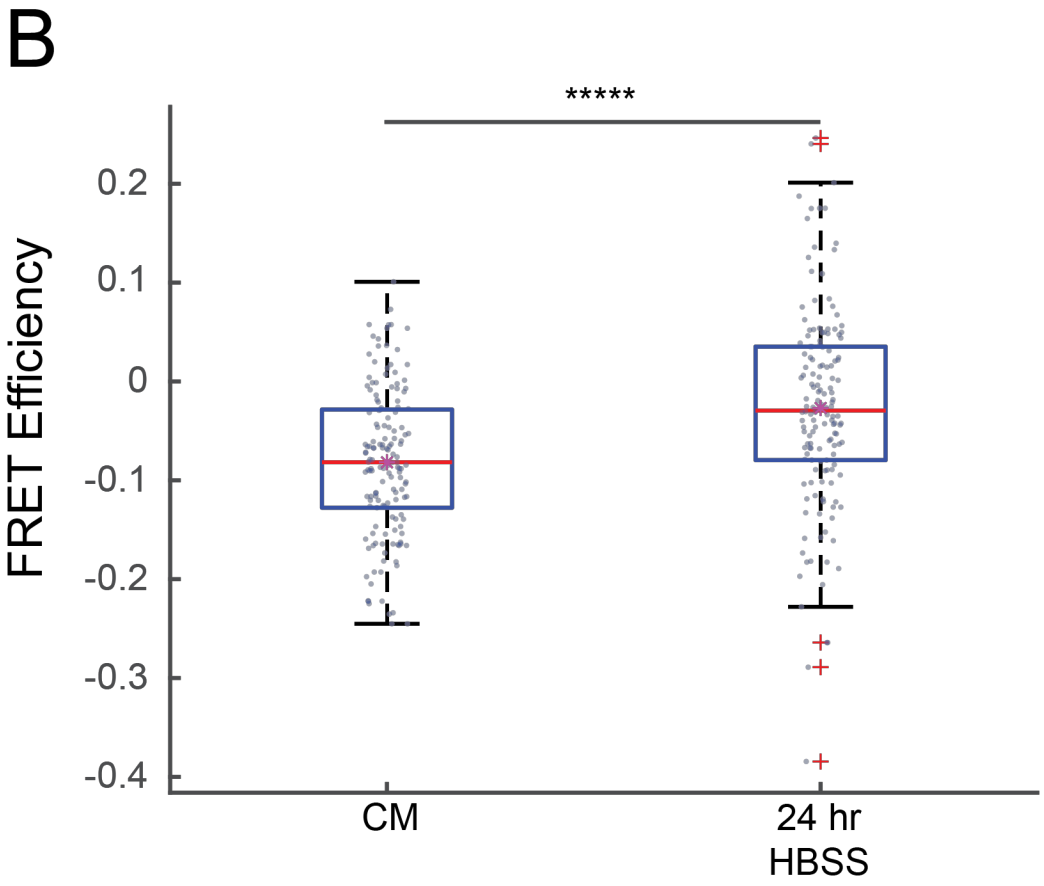
B
*****
FRET Efficiency
0.2
0.1
0
-0.1
-0.2
-0.3
-0.4
CM
24 hr
HBSS

CHAPTER 5: FUTURE DIRECTIONS AND IMPLICATIONS

As I summarized in the introduction, the NPC serves as an important coordinator of cellular gene expression and a defender against foreign and pathogenic agents in the cell. This massive cellular machine, sized over 125 MDa in humans, has been challenging to approach with traditional cell biology and imaging techniques due to the complexity of its interactions with different cellular components and the fact that all of these interactions occur beneath the resolution and time scale of most modern microscopy. In my attempt to gain an understanding of the organization and function of the NPC, I have developed and applied new technologies in computational modeling and in fluorescence microscopy.

Overall, my research has underscored how studying cellular machinery in its native environment can lead to new insights. For example, only when I modelled the FG-Nups in the context of the entire NPC and quantified the anisotropy of the filaments in the context of an intact NPC in living cells did behaviors such as the longer persistence length of filaments close to the center of the pore emerge. Likewise, the change in conformation of Nup54 after starvation as Chapter 4 only became apparent after perturbing cargo *in vivo*.

In this final chapter, I will begin by evaluating the relevance of this work to our current understanding of the NPC's function inside of cells. Secondly, I will outline the immediate future directions of the research described in the previous chapters. Finally, I will describe how polarization microscopy can be applied to other biological

systems and how the versatility of the technique could be greatly advanced through some basic technological improvements.

5.1 Discussion Part I: Coarse-Grained Modelling

Selective transport across the nuclear envelope through the NPC is an essential part of eukaryotic life. Although models have been proposed to explain this phenomenon, distinguishing between these models has proved challenging in part because they have been articulated in qualitative terms, precluding validation or refutation by experimental evidence. Our understanding of the mechanism of transport will benefit from better understanding of the dynamics of filaments within the NPC.

The selective phase and the reduction of dimensionality models both predict that filaments form a mesh-like barrier. The competition or entropic exclusion model has less stringent requirements for movements of the filaments. The Brownian ratchet model (Simon et al., 1992; Mincer and Simon, 2011) requires that the filaments themselves translocate the pore; since it is posited that cargo translocates while bound to the same one or few FG-Nups, those FG-Nups must also translocate. Therefore, the observation of translocation of simulated filaments across the NPC within a biologically realistic model of the FG-Nups was of particular interest.

The Coarse-Grained Model Predicts Experimental Observables

Our model of the yeast NPC predicts experimental observables that may be relevant for resolving between the models of transport. The simulated FG-Nup filaments, as assayed by autocorrelation functions, were shown to exhibit properties

similar to FG-Nups *in vivo*, as assayed by anisotropy (Atkinson *et al.*, 2013). Nup116 and Nup159 showed a decrease in orientational rigidity along their length both *in vivo* and in our computational model. In the simulation, this decrease occurred regardless of the simulated strength of the FG-FG bond. In contrast, the experimentally observed orientational freedom of Nup57 (and its mammalian homologue) decreased much less along its length. This experimentally observed behavior of Nup57 was recapitulated in this model for FG-FG bond strengths of FG4, FG5, and FG6. However, in the absence of FG-FG bonds, the orientational freedom was predicted to decrease along the length. The dependence of the behavior of this FG-Nup on FG-FG bonding underscores the influence the local environment can have on these behaviors. Either way, the different behaviors of these simulated Nups recapitulate their distinct behaviors *in vivo* and illustrate the capability of our model to reproduce behaviors of the filamentous FG-Nups. In Atkinson *et al.*, the differences in the orientational freedoms of different Nups were attributed to their anchor's location along the nucleo-cytoplasmic axis. For example, Nup57 is anchored in the middle of the channel and is relatively short. Therefore, its tip does not experience the orientational freedom of extending out of the pore as frequently as the tips of Nup116 and Nup159, which are longer and more peripherally anchored. As shown in our data, the nematic order is much higher in the interior of the NPC, so filaments located there will have less decay in their autocorrelation functions.

Signatures of Transport Models Emerge in our Coarse-Grained Simulation

Signatures of existing qualitative models of transport through the NPC emerge during this simulation. When FG-FG binding is strong, a gel reminiscent of the selective phase model forms. When the FG-FG off rate is low, the FG-Nups form a dynamic barrier reminiscent of the entropic exclusion model. Therefore, our model enables a more quantitative formulation by which to distinguish between qualitative models. By correlating the model parameter space with signatures of qualitative models, prediction of experimental observables through simulation becomes possible.

The strongest FG-FG binding condition (FG4) increased the density of FG-Nups within the lumen of the NPC and decreased nematic order, meaning that when the filaments were more cross-linked and in a mesh-like condition; they were less aligned and showed less order. The central channel was also less pronounced in these simulations. These results differ from earlier work by Moussavi-Baygi *et al.,* where the authors increased the densities of FG-motifs on their filaments and found that this modification was not sufficient to create a channel-filling hydrogel (Moussavi-Baygi *et al.*, 2011). The construction of our model differs from the 2011 Moussavi-Baygi model in several key respects: our model is a 3D model instead of a 2D model, our filaments are based on the actual protein sequences of yeast FG-Nups, with heterogeneity in length, binding site locations, and anchor positions.

Faster FG-FG off rates yielded more dynamic filaments with a very low degree of cross-linking. These less stable FG-FG interactions showed little statistical

difference from the absence of FG-FG interactions (FG_{off}). These weaker bonds demonstrated a decrease in the density of FG-Nups located within the lumen of the pore and an increase in nematic order. Less cross-linking was therefore seen to result in a more ordered liquid-crystal like state and a central channel of decreased density relative to the rest of the pore lumen. The simulations of Tagliazucchi *et al*. produced a similar central channel, which they attributed to electrostatic interactions; however, I observe a similar channel within the lumen that develops in the absence of any electrostatic interactions simply due to the arrangement and polymer-like properties of the FG-Nup filaments. In recent simulations, the electrostatic content of the FG-Nup amino acid sequence has been predicted to affect the FG-Nup distribution by preventing the aggregation of FG-Nups and ensuring that FG-Nups are evenly distributed and free to move by Brownian motion (Peyro et al., 2015a). Although I do not explicitly model electrostatic forces, I have calibrated our simulations such that the end-to-end distances match previously modeled NSP1 that did incorporate the electrostatic and hydrophobic interactions (see Methods). Thus, our simulations implicitly incorporate the effects of these charges. However, coarse-grained modeling that indicates that charges are not homogenously distributed in the NPC (Tagliazucchi et al., 2013) and reports of the strong effect of heterogeneous charge and hydrophobicity in a polymer-coated nanopore (Huang and Szleifer, 2017), suggesting a possible effect of non-uniform charge distribution on the FG-Nup dynamics. I look forward to explicitly incorporating charge in future simulations, to determine what effect it might have on our filament dynamics and filament interactions with specific and non-specific cargo.

The actual FG-FG off rate in the biological context of the NPC is not known. A quantitative measure of this off rate might help to address the amount of crosslinking within the NPC. To the extent that recent experimental evidence points to an increased nematic order within the NPC (Atkinson *et al.*, 2013), one can speculate, based on our results, that this evidence favors an FG-Nup organization that is relatively not cross-linked. The results point to the need for more *in vivo* work to further elucidate FG-Nup dynamics, which these results suggest could ultimately lead to differentiation between competing models of the mechanism of selective transport and its relation to FG-Nup behavior. The population of FG-FG binding sites is heterogeneous, including four main groups: FxFG, FG, GLFG, and PxFG (where x is any amino acid), and differing binding strengths between different repeats has been reported in the literature (Xu and Powers, 2013). The difference between the FG-repeat types remains an unexplored parameter in this model, although the ability to modulate binding strengths between different types of FG-sites independently is encoded in the model and can be explored in future simulations.

Simulated FG-Nups are Highly Mobile at the Timescale of Cargo Translocation

The translocation of FG-Nups in our simulation occurred at rates of milliseconds, consistent with the rate of cargo transport, and at frequencies high enough to account for transport, consistent with a Brownian ratchet model. Although our model agrees with another model that predicts quasi-stable structures of the FG-Nup filaments at the timescale of nanoseconds (Gamini et al., 2014), our model also suggests that these filaments are highly mobile at longer timescales. Our simulation is consistent with a model that suggests that FG-Nups are subject to rapid Brownian

motion, with fast local rearrangements on the order of microseconds (Moussavi-Baygi and Mofrad, 2016; Mincer and Simon, 2011) and slower larger scale rearrangements on the order of milliseconds. Furthermore, our results are inconsistent with the results that suggest that the filaments are relatively stable and form a gel-like meshwork (Zahn et al., 2016b). Our results suggest that the Nups are highly flexible, experiencing Brownian motion, regardless of the degree of FG-Nup cross-linking and mesh formation within the pore. Our model's prediction of the ubiquity of FG-Nups translocating the NPC on timescales similar to that of cargo transport is significant and will hopefully stimulate and guide future experiments.

5.2 Discussion Part II: Orientational Sensors

Although the various structural techniques applied to study the NPC scaffold, such as AFM on single NPCs in isolated nuclear membranes, cryo-EM of NPCs, and crystallography of Nup fragments have been informative in learning about the biochemical makeup of the NPC, none of these techniques allow for monitoring the dynamics of Nups *in vivo* on the timescale of cargo transport. In order to begin to study the dynamics of these proteins *in vivo*, I have developed and validated a technique using polarized-total internal reflection microscopy (pol-TIRFM).

Building Orientational Sensors

Using this technique, I have been able to monitor the orientations of Nups *in vivo*. I have measured the dynamics of various nuclear pore proteins, including Nup54, a scaffold protein that is part of the inner ring, as well as Nup93 and Nup133, proteins that are part of different structural rings. This imaging technique allows me to measure the dynamics of many NPCs (100+ NPCs) in parallel within a single cell.

I built conformational sensors by rigidly conjugating mEGFP to these Nups. These conformational sensors allowed for the monitoring of the conformations and dynamics of the various rings of the NPC *in vivo*. By characterizing the orientational sensors by individually validating that the mEGFP can rotate with respect to the Nup with an addition of a single amino acid, I have established a protocol for validating the use of mEGFP to monitor the orientation of a protein of interest *in vivo* at the level of single NPCs. This technique is similar to a technique previously used in our lab where wide-field polarization microscopy was used to measure the anisotropy of

Nups and these anisotropy measurements revealed the orientation of scaffold Nups with respect to the NPC assembly (Kampmann et al., 2011). I have expanded the technique to be able to measure the dynamics and orientations of Nups within single NPCs and show how some Nups change orientation within a single NPC shift after perturbation of the transport state.

My results are consistent with large-scale conformational changes to the inner ring in response to changes in the transport state, suggesting that this part of the NPC experiences conformational changes in response to cargo translocation. These conformational changes provide new evidence that the scaffold of the NPC may be a dynamic gate that can regulate nuclear trafficking. Since these conformational changes were observed in relationship to the cargo-state of the NPC, it is suggestive that perhaps the NPC structure as a whole is modulated by the cargo load and identity. Whether this modulation in conformation serves as a mechanism for regulation or is a byproduct of transport remains to be investigated.

Starvation

Under conditions of starvation, the orientation of my Nup54 conformational sensor shifted in both the transient transfection and the CRISPR cell line, while the other Nups did not undergo any detectable alterations. Although the effect of starvation on the mammalian NPC is not well characterized, I observed obvious alterations to the efficacy of the NLS and NES signal sequences of the Light Activated Nuclear Shuttle (LANS) construct. In the non-light induced state, the LANS construct was more effectively excluded from the nucleus, as demonstrated by a

lower ratio of nuclear to cytosolic signal. This lower ratio indicates that the LANS construct is able to be transported out of the nucleus, but is less frequently imported into the nucleus. After the light-induced conformational change, the cargo was less efficiently trafficked into the NPC. These results together suggest that starvation might selectively inhibit import into the NPC. In addition, the rates of import into the nucleus are reduced upon light activation of the LANS construct compared to the rates in a cell with complete media, indicating that the NLS-driven import system is working less efficiently. In addition, by quantitative immunofluorescence I observed a slight but statistically significant change in the amount of kap1β localized to the NPC, indicating that the kap load associated with the NPC might be altered. The kaps are capable of interacting with the FG-domains of the inner channel ring Nups, Nup54, Nup62, and Nup58.

The inner channel ring Nup54-mEGFP fusion proteins shifted in orientation after starvation to a degree detectable by my method. The Nup93 only exhibited slight shifts in orientation and the Nup133 fusion proteins did not exhibit any discernable shifts in orientation upon the same starvation. These results suggest that Nup54 experiences a significantly greater rearrangement than Nup93 or Nup133. Additionally, the lack of evidence of a strong Nup93 or Nup133 orientational shift suggests that the movement is confined to certain domains of the NPC and is not due to a global stress-response from the entire NPC or the crenulation of the nuclear envelope.

Dominant Negative Ran

Transfection with a dominant negative Ran also saw an attenuation of NLS/NES-mediated cargo transport. In the transiently transfected HeLa cells, I observed a less efficient nuclear exclusion of the LANs construct in the dark and a lower rate of import after stimulation with blue-light. I also observed an accumulation of kap1β at the NPCs in fixed cells after transfection with the dominant negative Q69L, indicating that the export complex of kap1β-RanGTP is unable to undergo hydrolysis by Ran-GAP and is therefore unable to dissociate from the NPC. This creates a locally high concentration of export complexes bound to the NPC. Under these conditions, the Nup54 construct underwent a conformational shift while the Nup133 construct appeared unperturbed. The conformational change in Nup54 may be due to the higher concentration of kaps at the NPC, where they may be able to instigate a conformational change in the NPC.

Cytosol Removal

When the HAP1 CRISPR cells were permeabilized and the cytosol was removed, there was no change in the *p/s* ratio of either the Nup133 or the Nup54 conformational sensors, suggesting that removing cytosol alone is not sufficient to drive this conformational change. The removal of cytosol does not cause import complexes to dissociate from the NPC. In order to remove these import complexes, an exogenous Ran-GTP protein must be introduced to the nuclear periphery. The lack of a shift in *p/s* orientation suggests that I have arrested the NPCs in whatever transport states they were in pre-permeabilization.

With the digitonin permeabilization system, I will proceed to manipulate the nuclear periphery and add back transport factors to determine if exogenous transport factors can induce this conformational change.

Ran-GTP Treatment

With the addition of Ran-GTP to cells expressing mCherry-kap1, I was able to directly visualize the cargo complexes disassociating from the nuclear periphery. After the addition I saw that the *p/s* ratio of Nup54 shifted, but the *p/s* ratio of Nup133 did not experience an orientational shift. This result strongly suggests the removal of cargo induces a conformational change in the inner channel ring of the NPC, suggesting that kaps themselves might serve as a gating mechanism for the NPC.

WGA Treatment

Permeabilized cells were incubated with lectin wheat germ agglutinin (WGA), which allows cargo binding but prevents transport (Finlay et al., 1987; Shulga et al., 1996). The WGA is hypothesized to interact with O-linked glycosyl groups and cause crosslinking and immobilization of the FG domains of Nup62, Nup214, Nup153, and Nup54.

Previously, our lab used fluorescence anisotropy to measure the orientational freedom of different domains of the FG-Nups. Using this technique, I observed that after incubation with WGA, the FG-domains of Nup62 and Nup54 that sat close to the O-linked glycosyl groups experienced an increase in their disorder, indicating that their organization was altered after WGA crosslinking.

When the CRISPR cell lines containing the conformational sensors were permeabilized and incubated with WGA, the *p/s* ratio of the Nup54 conformational sensor shifted, but the *p/s* ratio of Nup133 conformational sensor did not experience an orientational shift. Interestingly, my orientation sensor in Nup54 is located on the opposite side of the structured, coiled-coil region of Nup54 from the putative O-linked glycosylation sites, indicating that binding in the O-linked glycosylation region has the potential to act a distance (Figure 44).

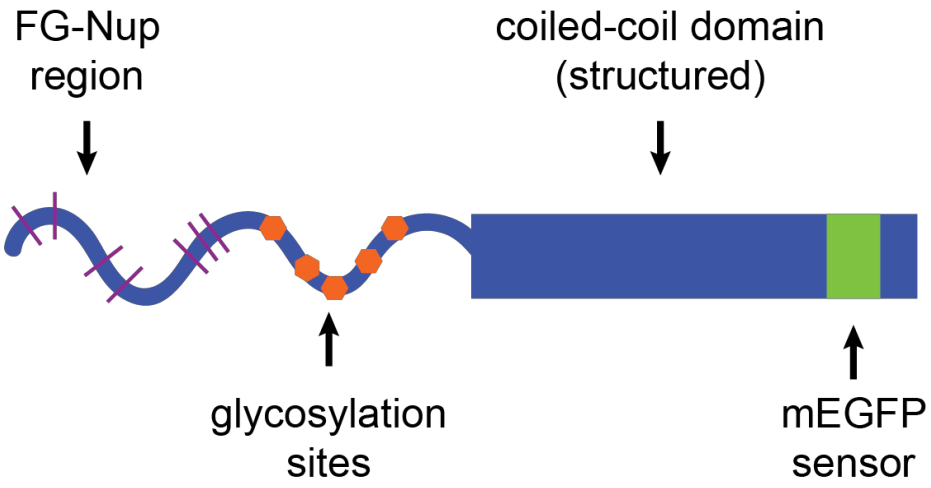

Figure 44. Nup54-mEGFP494 Schematic Showing Putative Glycosylation Sites.

FG-Repeats are shown as purple marks and putative glycosylation sites are shown as orange hexagons. The coiled-coil domain is shown as a rectangle and the mEGFP incorporation site is mapped out along its length.

The sites of O-linked glycosylation in Nups are upregulated under conditions of oxidative stress, indicating that this region may be potentially a site of regulation (Crampton et al., 2009; Kodiha et al., 2009). In mammalian NPCs, the lumen of the NPC contains a region known as the “glyco-belt,” wherein several of the inner ring Nups are subject to a large number of possible glycosylation events. The physiological significance of this region is not known. However, these residues have the potential to be enzymatically deglycosylated and potentially phosphorylated. These glycosylated residues could compose a more dense region of the NPC or a region with altered biochemical properties that could serve as a location of regulation for nuclear-cytoplasmic trafficking.

FRET Measurements Suggest Reorganization of Nup62 FG-Domain after Starvation

Förster resonance energy transfer (FRET) is a technique whereby the distance of two fluorophores can be measured. The efficiency of the energy transfer from the donor chromophore to the acceptor chromophore is inversely proportional to the sixth power of the distance between the two, making FRET much more efficient when the two are close together. For fluorescent proteins, the range of distance where FRET can occur is typically under 10 nm. When I tagged Nup62 at two locations within its FG region, I was able to show differential FRET efficiencies before and after starvation as measured through acceptor bleaching. This differential FRET suggests that the Nup62 ‘finger’ domains reorganize after starvation, which suggests that this orientational shift at Nup54 results in a constriction and dilation of the transport channel.

Acceptor bleaching is an irreversible measurement and cannot be visualized over time. In the future, I hope to monitor FRET within an NPC over time using polarized light microscopy (Piston and Rizzo, 2008; Rizzo and Piston, 2005). Since the orientational diffusion of mEGFP is slow with respect to its time in its excitation state, the excitation of mEGFP results in highly polarized emission. The strength of this polarization will be even stronger since our mEGFP is conjugated to a larger protein. If FRET occurs, the emitted light will be less polarized. Using this technique, I should be able to monitor the degree of FRET of these probes over time to ascertain the timescale of this reorganization of the Nup62 'finger' domains

Flexibility in the NPC

By monitoring the *p/s* orientation over time, I have been able to monitor the dynamics of the NPC over time *in vivo.* For decades, there has been evidence that components of the NPC might be flexible. Cryo-EM has demonstrated that the NPC can experience a range of structural variation (Akey, 1995). By applying cryo-ET to transport-competent, intact NPCs, distinct structures were obtained in the presence and absence of the central plug/transporter, suggesting that the addition of transport factors in the NPC leads to structural rearrangements to the NPC scaffold (Beck, Science 2004). The plasticity of the NPC was also observed with cryo-electron tomography in intact *Dictyostelium* nuclei (Beck et al., 2007). More recently, cryo-electron tomography in conjunction with sub-tomogram averaging has allowed for the resolution of individual protein domains of the NPC and has shown that the arrangement of these domains is altered in cells where transport is reduced (Eibauer et al., 2015).

The technique of fluorescence polarization microscopy developed in a series of papers by our lab provides the first tools to directly observe the orientations and orientational dynamics of Nups in living cells. By expanding this technique into pol-TIRF, I have developed the first tools to directly observe the orientational dynamics of Nups within a single NPC and to track these dynamics over time with different cargo conditions.

By combining these tools with other imaging techniques and with microscopy to image cargo translocation over time, I plan to use the tools developed in this thesis to image the effect of cargo translocation on the dynamics of individual NPCs. With these combinations of techniques, I should be able to gain insight into the conformational changes and dynamics experienced by different Nups during the transport of large cargos.

5.3 Future Directions:

Possible mechanisms for the NPC conformational changes observed in this study include the binding of cargo complexes and the flux of cargo, especially large cargo. Alternatively, changing the quantities and identities of the kap complexes occupying the NPC lumen could provide regulatory cues that drive this conformational change

Cargo Translocation

Using the digitonin permeabilization system, NLS-driven cargo import can be reconstituted (Moore and Blobel, 1993). The simplest nuclear import assay involves digitonin permeabilization of the cell and then incubation of these cells with NLS-cargo, cytosol (which supplies the transport factors), an ATP-regenerating system, and GTP (Cassany and Gerace, 2008).

With my current pol-TIRF experimental set up, I will be able to simultaneously monitor the location of a fluorescent cargo molecule and the orientations of my conformational sensors. Therefore, I should be able to see whether the conformations of these proteins change upon the binding and translocation of specific cargos.

In particular, one could visualize whether the orientations of these proteins changes with large cargos. One specific large cargo readily available in our lab is the 26S proteasome. The dimensions of this complex are 20 nm x 45 nm and evidence exists that this complex does not disassociate to enter the nucleus in yeast (Pack et al., 2014) Other potential large cargos include fluorescent beads of specific sizes

conjugated to NLS tags or viruses that can be engineered with precise size and number of NLS tags.

Test Individual Kaps

As described above, cargo transport can be reconstituted with only added NLS-tagged cargo, cytosol, and energy. To study the specific components of the import machinery, the cytosol can be replaced with a mix of recombinant import factors. For example, NLS-tagged cargo can be reconstituted with kap1B, importin 1-alpha, NTF2, Ran, and energy (Cassany and Gerace, 2008). I have begun the purification of these proteins and plan to introduce titrate these proteins in the nuclear periphery to determine if any one of them individually can cause a change in the NPC organization. By using endogenous concentrations of purified proteins, I may be able to ascertain whether one of these proteins serves as a molecular “key” to induce this conformational change in the NPC.

5.4 Applications of Polarization Microscopy:

Most forms of super-resolution microscopy provide information only on the location of a fluorescent protein or biomolecule chemically conjugated to a fluorescent dye.

Fluorescence polarization microscopy provides the means to probe the organization and dynamics of biomolecules in cells. Polarization microscopy provides information about the orientation and freedom of movement of proteins. In the following sections, I will provide a description of how this technique can be improved and utilized to provide information that spatial localization microscopy cannot provide.

Fluorescence Anisotropy

Fluorescence anisotropy is a measurement of how much polarization is maintained within a population of fluorescent molecules. Fluorescence polarization microscopy has previously been used by our group to measure the dynamics of different Nups and domains within Nups to determine how flexible these Nups are in their orientations. In these previous studies, the fluorescence anisotropy was also used to determine the fixed orientation of Nup133, characterizing the orientation of this protein relative to the rest of the NPC.

Using our pol-TIRF set up, I have begun to monitor a proteolytic cleavage that occurs during HIV1-virion assembly. This work has been done in collaboration with Kate Bredbenner, a Rockefeller University graduate student. Our lab pioneered the use of TIRF microscopy to study the assembly of HIV1-virions on the surface of cells. Using fluorescently-tagged derivatives of Gag, the major structural component of HIV1, we are able to visualize the formation of single virions on the plasma membrane (Jouvenet et al., 2006, 2008). Visualizing this process has allowed us to characterize the recruitment of the cellular machinery necessary for viral budding (Bleck et al., 2014; Johnson et al., 2018; Jouvenet et al., 2011). By monitoring the orientation of fluorescently-tagged Gag, we were able to monitor the change in orientation as the virion formed and underwent membrane scission (Johnson et al., 2019).

An important step in HIV1-virion assembly is the action of an HIV protease that cleaves the Gag component into its constituent proteins. Without this cleavage

event, the virion is not infective (Kohl et al., 1988; Loeb et al., 1989). Protease cleavage is necessary for the creation of an infective virion, but the virion will still bud with an inactive protease (Göttlinger et al., 1989). Although it is known that this cleavage event occurs at the cell membrane, and not in the cytosol (Kaplan et al., 1994), the timing of this event relative to virion scission remains uncharacterized.

Using pol-TIRF microscopy, I have begun to determine the timing of this protease cleavage event. Both active and mutant proteases can assemble viruses on the surface of the cell. The virion-like particles that form show a clear difference in anisotropy based on whether they were assembled with an active or mutant protease. In addition, I have begun to track virion assembly *in vivo*. Using pol-TIRF, I have been able to monitor *in vivo* when protease cleavage occurs and have begun to time this cleavage with respect to the other viral assembly events and virion scission.

Technical Improvements: Polarization Microscopy

The technique of pol-TIRFM could also be immediately useful for many *in vitro* TIRF experiments, because many TIRF experiments are performed with molecules bound to the coverslip at defined angles. Furthermore, the user could use DNA origami to print “mounts” for the biomolecules at different, precise angles relative to the coverslip. Using such conjugation techniques, the user could measure the orientation of a substrate relative to a motor or vice versa. Likewise, the orientation of a domain of a particular motor or enzyme could measured relative to the rest of the protein, while that protein is in an active state.

In order to examine the orientations of molecules that do not share an axis of symmetry with the imaging system, having a microscope that would be able to modulate and respond to the read out of one fluorescent protein or a population of fluorescent proteins, and adapt the polarization of its beam such that the axis of illumination was relative to this protein would be a useful tool. This tool would be able to measure the fluctuations of this protein from its mean and would also be able to measure the changes in orientation of a differently tagged fluorescent biomolecule relative to this protein of interest.

One current limitation to fully utilizing the technique of fluorescence polarization microscopy are the types of fluorescent labels available. Currently, the only way to conjugate a fluorescent molecule to the protein of interest is by conjugating the amino terminus of a fluorescent protein that has a highly structured amino terminus (such as GFP) to the carboxyl terminus of the protein of interest. This conjugation is to ensure that the fluorescent dipole moment is held in a fixed manner with respect to the protein of interest. As demonstrated by this study, this conjugation does not always result in a rigid linkage, even when the protein of interest is predicted to be alpha-helical at its carboxyl terminus. Additionally, many proteins of interest or regions of interest inside of proteins are not alpha-helical, and it would be advantageous to be able to tag these domains as well.

No current method of conjugating a protein in mammalian cells to a fluorescent dye is capable of forming chemical bonds that do not rotate around a covalent linkage, except for the FlAsH/ReAsH Tetracysteine-based protein detection system (Griffin et al., 1998). Under this system, the biarsenical labelling reagents

FlAsH-EDT2 and ReAsH-EDT2 become fluorescent when they bind to a recombinant proteins containing the teracysteine motif of Cys-Cys-Pro-Gly-Cys-Cys, which can be expressed in any exposed region of the protein of interest. The FlAsH binds to the amino acids, forming two covalent linkages and a full fluorophore. Although our lab has previously been able to tag Nups using this tool in yeast, we have not been able to get sufficient signal at the NPC to be able to visualize any of our Nups with this method in mammalian cells. We have also been unable to tag other cytosolic factors with this method in mammalian cell culture, which leads us to believe that this system is not an efficient method of attaining the signal necessary to perform polarization measurements.

However, if a more efficient way of tagging proteins or other biomolecules with a dye molecule that has two covalent linkages, one could study the dynamics of proteins that cannot be rigidly tagged with GFP. Additionally, if a small covalent linkage could be created to stably incorporate a fluorescent dye in an orientationally confined way, it would be possible to visualize the orientational dynamics of protein domains without perturbing the dynamics of the protein with a bulky fluorescent protein.

The ability to tag proteins with smaller orientationally confined fluorescent tags would open a lot of options for monitoring the dynamics of proteins. In particular, being able to tag the same protein with two different fluorescent molecules could enable the testing of intermolecular protein dynamics by measuring the relative polarization of one fluorophore with respect to the other.

Further development of orientationally confined fluorescent tags will be a useful advance for the field. Even in the absence of such labels, polarization microscopy is a powerful tool for monitoring the organization and dynamics of proteins *in vivo* and *in vitro* while allowing the proteins to dynamically respond to their environment and perform work.

CHAPTER 6: Materials and Methods:

Part 1: Coarse-Grained Computational Modelling

This Section describes methods for Chapter 2. The following methods are adapted from my recent publication (Pulupa et al., 2017).

Dynamics of FG-Nup filament segments

The dynamics of each FG-Nup are modeled using the pairwise agent interaction with rational superposition (PAIRS) model (Alberts, 2009). The positions and orientations of these filament segments make up the coarse-grained degrees of freedom, thereby encompassing and eliminating the solvent degrees of freedom.

When any two FG-repeat sites collide, they can bind if they are not already bound to other FG sites. The strength of the bond formed is modulated by increasing or decreasing the off rate of the FG–FG bond, a parameter of the simulation. The off rate is stochastic, and is expressed as the number of bonds dissociated per second. Varying the FG–FG off rate over several orders of magnitude modulates FG–FG cross-linking, which allows the investigation of the influence of cross-linking on filament dynamics and flexibilities.

Filament segments experience five forces: (1) PAIRS forces that are responsible for ensuring that the FG-Nup behaves like a flexible filament, (2) repulsion forces resulting from interactions with the pore geometry, (3) adhesion forces between segments “bound” to each other, (4) repulsion forces resulting from collisions with other filament segments, and (5) Brownian forces. The forces between “bound” segments and the interactions with pore geometry are new to this

iteration of our model; however, the PAIRS forces, repulsion forces, and Brownian forces remain unchanged from the previous model (Mincer and Simon, 2011).

At a given time step during the course of our simulation, two adjacent segments on the same filament may become temporarily disconnected because of other forces. The PAIRS algorithm analytically determines the displacement necessary to reconnect the adjacent ends within one time step. Moreover, these adjacent filament segments are rotated to maintain a prescribed angle between them. The PAIRS forces have associated damping coefficients, which serve as a tuning mechanism to achieve desired filament flexibility. In addition to becoming disconnected, adjacent FG-Nup segments may temporarily overlap. The PAIRS algorithm also displaces segments to resolve overlap. Thus, in this model, a filament comprises a collection of rigid cylindrical filaments where adjacent segments are connected through a translational and rotational spring. The PAIRS algorithm provides a correction to the Euler time integration scheme to solve the system of differential equations for the filament dynamics along with algebraic constraints corresponding to setting the strain in both the translational and rotational springs is zero (Andrews, 2014).

FG-repeat sites

FG-Nup–repeat sites are fixed relative to the center of mass of the segment. Placement of FG repeats on particular segments and their positions on segments are determined by overlaying the primary amino acid sequence for the particular FG-Nup on the segmented filament and then performing a search for FxFG, FG, GLFG, and PxFG (where x is any amino acid). An FG site was then placed in the middle of

the FG sequence. Hydrophobic interactions between different FG repeats (either on different or the same filaments) are modeled as bonds that behave as harmonic springs with an equilibrium bond, $r_b = 0.6$ nm, length equal to the twice the radius of the filament. When the distance between two FG-repeat sites is less than 0.9 nm, three times the filament radius a bond is formed. In the event that there are multiple FG-repeat sites within 0.9 nm of a particular FG-repeat site, one of them is randomly chosen to form a bond with the FG-repeat site.

All bonds dissociate stochastically based on a predetermined off rate set at the start of the simulation. Because the FG-repeat sites do not necessarily coincide with the center of mass of the corresponding filament segment, the forces caused by these springs also result in a torque on the participating segments. Bonds are not allowed to form between FG sites on adjacent segments on the same filament. I enforce this condition, as I believe that these interactions are sterically unfavorable.

The following describes binding between two segments:

Allow $\vec{x}_{b,1}$ and $\vec{x}_{b,2}$ to be two binding sites bound to each other. Let $\vec{y}_i$ and $\vec{y}_j$ be the center of mass of segments i and j corresponding to the binding sites $\vec{x}_{b,1}$ and $\vec{x}_{b,2}$ respectively. The forces $\vec{F}_i$ and $\vec{F}_j$ due to this FG-FG interaction are given by:

$$\vec{F}_i = k\left(\left\| \vec{x}_{b,2} - \vec{x}_{b,1} \right\| - r_b\right) \frac{\left(\vec{x}_{b,2} - \vec{x}_{b,1} \right)}{\left\| \vec{x}_{b,2} - \vec{x}_{b,1} \right\|}$$

$$\vec{F}_j = k\left(\left\| \vec{x}_{b,1} - \vec{x}_{b,2} \right\| - r_b\right) \frac{\left(\vec{x}_{b,1} - \vec{x}_{b,2} \right)}{\left\| \vec{x}_{b,1} - \vec{x}_{b,2} \right\|},$$

where the spring constant, $k = 10^3$ pN/nm, is unchanged from the previous model. The torque on the corresponding segments is:

$$\vec{T}_i = (\vec{x}_{b,1} - \vec{y}_i) \times \vec{F}_i$$

$$\vec{T}_j = \left(\vec{x}_{b,2} - \vec{y}_j\right) \times \vec{F}_j \, .$$

FG-Nup interaction with geometry

The filament segments are not allowed to collide with either the NPC scaffold or the nuclear envelope. These collisions are prevented in two ways. When the segment is outside the lumen of the NPC and the calculated displacement would cause the segment to overlap the nuclear envelope, movement is only allowed perpendicular to the nuclear–cytoplasmic axis. This prevents collisions with the membrane. When the segment is inside the lumen of the NPC and the calculated displacement would cause the segment to overlap with the scaffold of the NPC, displacement is only allowed parallel to the nuclear–cytoplasmic axis.

Implementation

The strength of the FG-bond off rate was assessed over several orders of magnitude: FG4 = 10^4/s, FG5 = 10^5/s, FG6 = 10^6/s, FG7 = 10^7/s, and FG_{off} = 10^∞/s. At each time step for all binding conditions, FG repeats are checked to see which are close enough to form a bond. In the case of FG_{off}, the binding algorithm is not entered.

However, in the case of FG4, FG5, FG6, and FG7, a bin sort (described in detail in the following section) was performed, and bonds were made or broken.

Bin sort FG-FG–binding scheme

At each time step, FG repeats are checked to see which are close enough to form a bond. A priori one may think to compare each FG-repeat location with every

other one when determining whether a given FG repeat is in the vicinity of a potential binding partner. This scheme, however, results in a large computational cost that makes it infeasible to run simulations to the biological timescale of interest. The computational cost (number of operations) scales as the square of the number of FG-repeat sites in this scheme, referred to as “order N-squared,” or $O(N^2)$ (Knuth, 1998).

A more efficient method involves bin sorting (Knuth, 1998). Specifically, FG-repeat sites are sorted into bins of size 1 nm in each direction. The search for possible bonding partners for a given FG repeat then becomes local, and consequently, this data structure enables checking for bonds with computational cost that is on the order of the number N of FG repeats, referred to as “order N,” or O(N). Because the FG–FG interactions are in fact local and do not extend over a larger spatial range, the resulting dynamics are equivalent to the $O(N^2)$ method.

The pseudocode for this process is as follows: step 1: bin sort all FG repeat sites; step 2: shuffle the list of FG-repeat sites; step 3: loop over the shuffled list of FG-repeat sites; step 4: determine the bin j in which FG-repeat site i resides; step 5: store FG-repeat sites that reside in either bin j or reside in bins m, which share a vertex with bin j, in a temporary array; step 6: shuffle this temporary array; and step 7: check for binding criterion for each FG repeat site in this list.

The magnitude of speed-up achieved with the bin sort method is significant. 5,000 iterations of the algorithm (corresponding, for a 2-ns time step, to 10 μs of simulation time), took 64.3 s for the bin sort method as opposed to 43,182.4 s for the naive $O(N^2)$ implementation.

Anisotropy and autocorrelation functions

Anisotropy and autocorrelation functions are both measurements of the orientational freedom of molecules. The relationship between these measurements can be formalized by the Perin equation:

$$\frac{r_0}{r} = 1 + {}^{\tau}/_{\Theta},$$

where τ is the fluorescence lifespan, θ is the rotational correlation time, r is the measured anisotropy and r_0 is the fundamental anisotropy (the anisotropy of the probe in a fixed position).

Faster decay of autocorrelation functions correlates with a lower measured anisotropy value, and longer decay of autocorrelation functions correlates with a higher measured anisotropy value.

We have previously measured the anisotropy of Nups in their native context inside the NPC. This approach was taken because we found that Nups in the NPC showed altered anisotropy when we changed their location in the NPC and much lower anisotropy when they were expressed elsewhere in the cell, outside of the packing in the NPC (Atkinson et al., 2013). We evaluated their orientation and dynamics by inserting fluorescent probes at several points along the unstructured domain of the FG-Nups and measuring the fluorescence anisotropy at the different positions (Atkinson et al., 2013; Kampmann et al., 2011; Mattheyses et al., 2010)

Fluorescent anisotropy experiments are performed by exciting fluorophores with a given linear polarization of light. By measuring the light emitted parallel to the excitation and the light emitted perpendicular to the excitation, one can calculate a

fluorophore's anisotropy, or its orientational freedom. The measured anisotropy is directly related to the rotational correlation time.

To compare these experimental results to our coarse-grained model, I needed a method to measure orientational flexibility in our simulation. I calculated the autocorrelation function, a measure of orientational self-correlation, which can be calculated for a single filament segment over the time course of the entire experiment as follows:

$$f(k) = \frac{1}{(n-k)} \cdot \sum_{t=1}^{n-k} (\bar{u}_t) \cdot (\bar{u}_{t+k}) \ ,$$

where *k* represents the difference in time, n represents the total number of data points, and $\bar{u}_t$ represents the orientation unit vector at time *t*. In an ideal case, this autocorrelation is expected to approximate a single exponential decay, the half-life of which should be directly correlated to the decay of anisotropy that a fluorescent probe placed along the filament length should experience. Therefore, a faster decay in the autocorrelation function is equivalent to a lower anisotropy, and a longer decay in the autocorrelation function is equivalent to a higher anisotropy.

Nematic order parameters

The nematic order parameter is used to characterize the orientational order in liquid crystals. It is calculated by taking the largest positive eigenvalue from a second order orientational descriptor *Q* (Eppenga and Frenkel, 2006).

Q takes the form of a three-by-three second order tensor, where each element, $Q_{\alpha\beta}$, is defined as follows by α and β, which represent *x*, *y*, and *z*:

$$Q_{\alpha\beta} = \frac{1}{2\times N}\left(\left(3 \times \sum_i \bar{u}_{i\alpha} \times \bar{u}_{i\beta}\right) - \delta_{\alpha\beta}\right),$$

where *N* represents the number of segments, $\bar{u}_{i\alpha}$ is the α component of the orientation unit vector of the i^{th} segment, and $\delta_{\alpha\beta}$ is the Kronecker delta function. The nematic order parameter is always between 0 and 1, with 1 indicating the maximal order and 0 indicating complete disorder.

Analysis and visualization

All analysis and visualization of computational output was carried out using the software MATLAB (The MathWorks, Natick, MA).

Part 2: Microscopy

Microscopy: General

Cells were imaged on a custom-built microscope, based on an Olympus IX-81 frame and equipped with a custom built through-the-objective (100X UAPON 1.49 NA, Olympus) polarized TIRFM illuminator (Johnson et al., 2014) equipped with a 405-nm laser (100 mW LuxX diode laser, Omicron), a 488-nm laser (100 mW LuxX diode laser, Omicron), a 594-nm laser (100 mW iode-pumped solid-state laser, Cobolt AB), and a 647-nm laser (100 mW LuxX diode laser, Omicron). The temperature was maintained at 37C throughout imaging using custom-built housing.

The excitation TIR light was azimuthally scanned at 200 Hz with mirror galvanometers (Nutfield Technology). All emission light was collected after it was passed through a multiband polychroic (zt405/488/594/647rpc 2mm substrate, Chroma) to isolate the excitation light from the emitted light.

An electrooptic modifier (EOM, Conoptics) and a quarter-wave-plate (Thorlabs) before the galvanometers to controlled the polarization of the 488 nm laser.

Images were collected on a CMOS camera (Flash-4.0, Hamamatsu) connected with Hammatsu Camera Link interface to a workstation (Precision Model T7500, Dell) running image acquisition software (Metamorph). The galvanometers, EOM, camera shutter, and 488 laser shutters were all driven by a multifunctional data acquisition board (PCIe-6323, 577 National Instruments) and controlled from custom written software in LabView (Johnson et al., 2014).

Microscopy: pol-TIRF of mEGFP Nups

A sequence of 20 images was taken in TIR, alternating between p and s with each acquisition and yielding 10 *p* and 10 *s* images. Each individual *p* or *s* image had an exposure time of 5 ms (laser power: 100 mW), and a new image was collected every 15 ms.

Microscopy: Immunofluorescence

Cells were imaged with 488 laser (laser power: 10 mW) for 200 ms and 594 laser (laser power: 10 mW) for 200 ms. (Immunofluorescence staining protocol is below, page 180).

Microscopy: BFP-DN-Ran

BFP was visualized with 405 laser (laser power: 5mW) for 200 ms,

Microscopy: Light Activated Nuclear Shutttle (LANS)

Cells were imaged every 20 s with 594 laser (laser power: 5 mW, 200ms exposure time) for 2 minutes, then 594 laser acquisitions (laser power: 5 mW, 200ms exposure time) were interleaved with pulses of 488 acquisitions (laser power: 3 mW, 2 s exposure time) every 20 s for 13 minutes, and then cells were imaged every 20 s with 594 excitation light (laser power: 5 mW, 200ms exposure time) for 15 minutes with no 488 excitations. All excitations were done in a ‘semi’-TIRF excitation mode, which restricts fluorescent to a few micrometers near to the coverslip to illuminate more of the cytosol.

Part 3: Automated Image Analysis

All image analysis was automated with author-written analysis algorithms written in MATLAB.

p/s Imaging Pipeline Pseudocode for Static Measurements

1- 10 *p* and 10 *s* images for a given timepoint were deinterleaved, and summed to form a single *p* and a single *s* image for each time point.
2- Camera background was subtracted from each image.
3- User selects area to consider for NPC identification in order to limit the area to 1 nucleus and prevent the analysis from considering any cytoplasmic puncta.
4- NPCs are identified via an automated algorithm using the Laplacian of Gaussian (LoG) algorithm (written by Vincent Garcia, based on (Lindeberg, 1998)).
5- NPCs were excised from a background subtracted image (top-hat filtered), and both polarizations were fit to a Gaussian (Gaussian fitting algorithm, Daniel Johnson). If either polarization did not fit to a Gaussian, the data point was rejected.
6- The intensities from the original (not-top-hat filtered but camera background subtracted and summed) images were then extracted for analysis by taking the intensity from the maximum intensity pixel from each punctum at each polarization.
7- A *p/s* ratio was then calculated for each puncta.

p/s Imaging Pipeline Pseudocode for Fluctuations

1-5- Same as above.

6- The intensities from the original (camera background subtracted, deinterleaved *p* and *s* images) images were extracted for analysis by taking the intensity from the maximum intensity pixel from each punctum at each polarization image at each time point.

5- A *p/s* ratio was then calculated for each puncta for each time point.

IF Quantification

NPCs are identified via an automated algorithm using the Laplacian of Gaussian (LoG) algorithm (written by Vincent Garcia, based on (Lindeberg, 1998)) and the maximum value pixel is quantified.

FRET Quantification

NPCs are identified via an automated algorithm using the Laplacian of Gaussian (LoG) algorithm (written by Vincent Garcia, based on (Lindeberg, 1998)), and then are tracked via a cross correlation function in the post-bleach image. The maximum value pixel is quantified. FRET values are calculated as:

$$FRET_{eff} = \frac{(I_{post} - I_{pre})}{I_{post}}.$$

Part 3: Cell Maintenance and Molecular Biology

Cell Lines and Growth

All cells were grown in Dulbecco's Modified Eagle's medium (DMEM, Gibco), supplemented with l-glutamine and sodium pyruvate (from here-on referred to as DMEM) and 10% (vol/vol) fetal bovine serum (FBS, Sigma) in humidified incubators at 37C and in a 5% CO2 atmosphere, using standard sterile techniques. Cells that were starved were starved in 1x Hanks Buffered Salt Solution with calcium and magnesium (HBSS, Gibco).

Imaging Conditions

Cells were seeded onto MatTek dishes with no. 1.5 coverslips. For HeLa cells, the dishes were uncoated, but for Hap1 cells the dishes were coated with Fibronectin (Invitrogen). During imaging, the media was replaced with cell imaging media (HBSS (Sigma), 10 mM HEPES, pH7.4), supplemented with 1% FBS (vol/vol, Sigma).

Transfections

Nups and LANS constructs were transfected 48 hours before imaging, with Fugene6 (Promega). Kap1β-mCherry and DN-Ran were transfected 16 hours before imaging. Cells were transfected with 1ug DNA (for LANS, Nup133-mEGFP, Kap1β-mCherry, and Nup93-mEGFP constructs), 500 ng DNA (BFP-DNRan constructs), or

250 ng DNA (Nup54-mEGFP) and 3uL FuGENE6 (Promega) in 100 uL Opti-Mem I (Gibco) according to the manufacturer's instructions.

Digitonin Permeabilization

Cells were incubated on ice for 5 min. Then cells were washed in cold transport buffer (TB) (20 mM HEPES, 110 mM potassium acetate, 5 mM sodium acetate, 2 mM magnesium acetate, and 1 mM ethylene glycol tetraacetic acid (EGTA)). Cells were then incubated on ice in TB with 34 ug/mL digitonin (Sigma) for 5 minutes. Cells were then washed twice in cold TB and twice in 37C TB with 1.5% (wt/vol) polyvinylpyrrolidone (PVP, Sigma). Cells were imaged in 37C TB with 1.5% PVP.

Ran Purification

His-tagged Ran in the pET28 vector (a gift from Dr. Günter Blobel) was transformed into BL21 (DE3) RIL-competent cells (Stratagene). Expression was induced with 0.5 mM isopropyl β-D-1-thiogalactopyranoside (IPTG, Sigma) and cells were grown for 3 hours. Cells were spun at 6,000 x g for 10 min at 4C and the pellet was frozen overnight before lysis (Sorvall SLA-1500)

The pellet was resuspended in 50 mM TRIS pH8, 150 mM NaCl with benzoase (at 25 U/mL, Millipore) and r Lysozyme (at 12 U/mL, Novagen) and 1x cOmplete protease inhibitors (Roche). The resuspended pellet was passed through a high pressure homogenizer (Avestin EmuliFlex-C3, ATA Scientific) for lysis. The

lysate was spun at 30,600 x g at 4C for 30 min (Sorvall SS-34 rotor). Imidazole was added to the lysate to a concentration of 10 mM. The supernatant was added to Ni^{+2} beads (Qiagen) and nutated at 4C for 1 hour. This supernatant was then loaded on a column (Qiagen) and washed 3x with 50 mM Tris pH8, 150 mM NaCl, 20 mM imidazole. Ran was then eluted with 50 mM TRIS, 150 mM NaCl, 300 mM imidazole in 500 uL fractions. The concentration of Ran was estimated by OD and the highest fractions were pooled and buffer exchanged and concentrated on Amicon Ultra Centrifugal Filter (10KD cutoff, Millipore). Samples were stored in aliquots of 10 mg in 50 mM TRIS pH, 150 mM NaCl, and 10% glycerol. Purification was confirmed by running the protein on a 4-12% Tris-Glycine gel (Novex) and performing a Coomassie (Figure 45, PageBlue, Thermo Scientific).

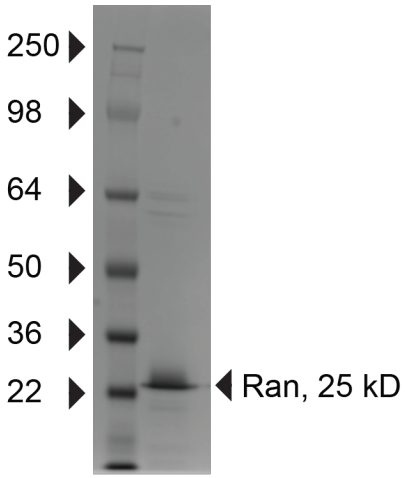

Figure 45. Coomassie-Stained Gel of Purified Ran.

The predominant band in a Coomassie-stained gel shows purified Ran with minimal contaminants.

Ran GTP Loading

Ran was incubated in 50 mM HEPES pH 7.3, 10 mM EDTA, 1 mM magnesium acetate, 2.5 mM dithreitol, and 1 mM GTP at *RT* for 30 min, before 2.5-fold dilution and addition of magnesium acetate to 5 mM. Free nucleotides were removed and the storage buffer was exchanged with TB by gel filtration on a PD-10 column (GE Healthcare).

Ran Treatment

Cells were permeabilized and as above, and were placed in 1 mL TB with 1.5% PVP at 37C. Cells transfected with both a Nup-GFP and kap1b-mCherry were imaged. A quantity of 0.5 mL of either TB at 37°C or Ran-GTP (at 3mg/mL) in TB at 37°C was added to the cells. Cells were imaged 1 hr later.

WGA Treatment

Cells were permeabilized using digitonin as above. After the digitonin incubation, cells were washed once with cold TB. Cells were then incubated with 2 mg/mL wheat germ agglutinin (WGA, either 100% WGA (Sigma) or 95% WGA (Sigma) and 5% WGA-AlexaFluor647 Conjugate (Molecular Probes, Invitrogen) in modified TB with no EGTA was added and cells were incubated on ice for 15 min. Cells were then washed twice in cold TB and twice in 37°C TB with 1.5% PVP. Cells were imaged with in TB with 1.5% PVP. *p/s* ratios were calculated from non-

fluorescent WGA incubations, fluorescent WGA incubations were imaged to validate nuclear rim accumulation.

Immunofluorescence

Cells were grown on MatTek dishes and processed at room temperature. Cells were fixed with 4% (wt/vol) paraformaldehyde in PBS for 10 minutes. Cells were washed 3 times for 5 minutes in PBS, and then permeabilized with 0.1% (vol/vol) Triton-x in PBS for 5 minutes. Cells were then blocked for 1 hour in blocking buffer (0.1% (vol/vol) Triton-x, 2.5% normal donkey serum, 2.5% normal goat serum, and 1% BSA (all from Sigma)). Primary antibodies were then added in blocking buffer and incubated overnight at 4C in a humid chamber. Cells were then washed 3 times for 5 minutes in PBS. Cells were then incubated with secondary antibody in 0.1% (vol/vol) Triton-x in PBS for 1-2 hr at room temperature. Dishes were dried and mounted with Prolong Diamond Antifade Mountant (Invitrogen). Antibodies used: polyclonal rabbit-α-mCherry (ab167453, abcam) at 1:500, monoclonal mouse-α-kap1b/impb-1 (3E9, Thermo) at 1:1000, goat α-mouse(AF488), goat α-rabbit (AF594) from molecular probes (1:1000).

Part 3: Gifted and Purchased Plasmids

TABLE 4: Table of Mammalian Expression Gifted and Purchased Plasmids.

Plasmid	Source
pmEGFP-N1	Clontech
ptagBFP	evrogen
pEGFP-C1X-Nup93	Gift from Lei Lu (Addgene plasmid # 87336 ; http://n2t.net/addgene:87336 ; RRID:Addgene_87336)
pNup133-mEGP(-7A)	(Kampmann et al., 2011)
pNup133-mEGP(-7B)	(Kampmann et al., 2011)
pNup133-mEGP(-8A)	(Kampmann et al., 2011)
pNup133-mEGP(-8B)	(Kampmann et al., 2011)
pNup54	Gift from Günter Blobel
pNup54-N1-mEGFP	(Atkinson et al., 2013)
pTriEx-mCherry::LANS4	Gift from Brian Kuhlman (Addgene plasmid # 60785 ; http://n2t.net/addgene:60785 ; RRID:Addgene_60785)

pmCherry-C1-RanQ69L	Gift from Jay Brenman (Addgene plasmid # 30309 ; http://n2t.net/addgene:30309 ; RRID:Addgene_30309)
pkap1β-mCherry	Gift from Dr. Günter Blobel

TABLE 5: Table of Bacterial Expression Gifted and Purchased Plasmids.

Plasmid	Source
His-tagged-Ran in pET28(+)	Gift from Dr. Günter Blobel

TABLE 6: Table of CRISPR Gifted and Purchased Plasmids.

Plasmid	Source
pSpCas9(BB)-2A-Puro (PX459) V2.0	Gift from Feng Zhang (Addgene plasmid # 62988; http://n2t.net/addgene:62988 ; RRID:Addgene_62988)

Part 4: Plasmids Constructed for this Study

Note: All PCR for cloning was done with Platinum™ PCR SuperMix High Fidelity (Thermo Fisher Scientific) according to manufacterer's protocols. Amplifications of mEGFP were all preformed with pmEGFP-N1 (Clontech).

pNup93-mEGFP(-4):

From pEGFP-C1X-Nup93 (gift from Lei Lu, Addgene plasmid # 87336), the plasmid was amplified with with 5'-tccggactcagatctcgacttcccgg-3' and 5'-catggtggcgaccggtagcgc-'3. The PCR product was gel purified and ligated with Quick Ligation Kit (New England BioLabs) to create an untagged pNup93. This plasmid was amplified with 5'-taagtgccatgctttgtgggagtctggg-3' and 5'-attcatgaggacctccatctgcaccagc-3' and mEGFP was amplified with overhangs: 5'-gaggtcctcatgaatGGCGAGGAGCTGTTC-3' and 5'-caaagcatggcacttaCTTGTACAGCTCGTC-3'. PCR products were gel purified and conjugated using NEBuilder® HiFi DNA Assembly Cloning Kit (New England BioLabs).

pNup54-mEGFP494(-4):

pNup54 (gift of Günter Blobel) was amplified with 5'-gagcatggactgaatgagaccatccacagc-3' and 5'- taccagcttgatatcttccaggtcgtcttttatgatgc-3' and mEGFP was amplified with 5'- gatatcaagctggtaGGCGAGGAGCTGTTC-3' and 5'- attcagtccatgctcCTTGTACAGCTCGTC-3'. PCR products were gel purified and

conjugated using NEBuilder® HiFi DNA Assembly Cloning Kit (New England BioLabs).

pNup58-mEGFP412(-4):

Nup58 was amplified from cDNA library (gift of Günter Blobel) with *5'-caccggtcccgcgacatggccacggggttctc-3'* and *5'-ctggacagcgcaatggtcatctctttcctcttttgtttccagcg*-3' and cloned into Clontech pmEGFP-N1 backbone that was PCR amplified with no GFP with *5'- gtcgcgggaccggtggatcc-3' and 5' ccattgcgctgtccagaggttcataaagct-3'.* PCR products were gel purified and conjugated using NEBuilder® HiFi DNA Assembly Cloning Kit (New England BioLabs).

pBFP-C1-RanQ69L:

pTagBFP (evrogen) was amplified with

5'-GACGAGCTGTACAAGtccggactcagatctc-3' and 5'-gatccgctagccaccatgAGCGAGCTGATTAAG-3' and *pmCherry-C1-RanQ69L* (gift of Jay Brenman) was amplified with 5'-tccggactcagatctcgagctcaagcttc and accgtcagatccgctagccaccatg-3'. PCR products were gel purified and conjugated using NEBuilder® HiFi DNA Assembly Cloning Kit (New England BioLabs).

pBFP-C1-RanT24L:

*pTagBFP (*evrogen*) was amplified with*

5’-GACGAGCTGTACAAGtccggactcagatctc-3’ and 5’-gatccgctagccaccatgAGCGAGCTGATTAAG-3’ and *pmCherry-C1-RanT24L* was amplified with 5’-tccggactcagatctcgagctcaagcttc and accgtcagatccgctagccaccatg-3’. PCR products were gel purified and conjugated using NEBuilder® HiFi DNA Assembly Cloning Kit (New England BioLabs).

The following plasmids were constructed via the QuikChange Ligthning Site-Directed Mutagenesis Kit (Agilent) with the following primer pairs:

TABLE 7: Table of Site-Directed Mutagenesis Primers for Cloning Plasmids.

Plasmid	Parent Plasmid	Primers
pNup93-mEGFP(-5)	pNup93-mEGFP(-4)	5’-*GCAGATGGAGGTCCTCATGAATGAGGAGCTGTTC*-3’ AND 5’-GAACAGCTCCTCATTCATGAGGACCTCCATCTGC-3’.

pNup93-mEGFP(-6)	pNup93-mEGFP(-4):	5’- *GATGGAGGTCCTCATGAATGAGCTGTTCACCG*-3’ AND 5’-CGGTGAACAGCTCATTCATGAGGACCTCCATC-3’.
pNup54-mEGFP494(-5)	*pNup54-mEGFP494(-4):*	5’-GAAGATATCAAGCTGGTAGAGGAGCTGTTCACCG-3’ AND 5’-CGGTGAACAGCTCCTCTACCAGCTTGATATCTTC-3’.
pNup54-mEGFP494(-6):	*pNup54-mEGFP494(-4):*	5’-CCCCGGTGAACAGCTCTACCAGCTTGATATCTTC-3’ AND 5’-GAAGATATCAAGCTGGTAGAGCTGTTCACCGGGG-3’.
pNup54-mEGFP494(0):	pNup54-mEGFP494(-4)	5’-GAAGATATCAAGCTGGTAGAAGCTGCTGCAAAGGAGGAGCTGTTCACCG-3’ AND 5’-CGGTGAACAGCTCCTCCTTTGCAGCAGCTTCTACCAGCTTGATATCTTC-3’.

pNup54-mEGFP494(1):	pNup54-mEGFP494(-4)	5’-GAAGATATCAAGCTGGTAGCAGAAGCTGCTGCAAAGGAGGAGCTGTTCACCG-3’ AND 5’-CGGTGAACAGCTCCTCCTTTGCAGCAGCTTCTGCTACCAGCTTGATATCTTC-3’.
pNup54-mEGFP494(2):	pNup54-mEGFP494(0)	5’-GAAGATATCAAGCTGGTAGCAGAAGCTGCTGCAAAGGAGGAGGAGCTGTTCACCG-3’ AND 5’-CGGTGAACAGCTCCTCCTCCTTTGCAGCAGCTTCTGCTACCAGCTTGATATCTTC-3’.
pNup54-mEGFP494(flex0):	pNup54-mEGFP494(-4)	5’-GAAGATATCAAGCTGGTAGGGGGTGGCGGCAGCTCCGAGGAGCTGTTCACCG-3’ AND 5’-CGGTGAACAGCTCCTCGGAGCTGCCGCCACCCCCTACCAGCTTGATATCTTC-3’.
pNup54-mEGFP494(flex1):	*pNup54-mEGFP494(flex0):*	5’-GAAGATATCAAGCTGGTAGGGGGTGGCGGCAGCTCCGGAGAGGAGCTGTTCACCG-3’ AND 5’-

		CGGTGAACAGCTCCTCTCCGGAGCTGCCGCCACC CCCTACCAGCTTGATATCTTC-3'.
pNup54-mEGFP494(flex2):	*pNup54-mEGFP494(flex0):*	5'-GATATCAAGCTGGTAGGGGGTGGCGGCAGCTCCG GAGAGGAGCTGTTCACCG -3' AND 5'-CGGTGAACAGCTCCTCTCCGGAGCTGCCGCCACC CCCTACCAGCTTGATATC -3'.
pNup54-mEGFP510(-4):	*pNup54-N-mEGFP (from Atkinson et al., 2011)*	5'- GCGGGGTCTTTAGCGGCGAGGAGCTGTT-3' AND 5'- AACAGCTCCTCGCCGCTAAAGACCCCGC-3'.
pNup54-mEGFP510(-5):	*pNup54-N-mEGFP (from Atkinson et al., 2011)*	5'- GGCGGGGTCTTTAGCGAGGAGCTGTTCACC-3' AND 5'-GGCGGGGTCTTTAGCGAGGAGCTGTTCACC-3'.
pNup54-mEGFP510(-6):	*pNup54-N-mEGFP (from*	5'- GCGGGGTCTTTAGCGAGCTGTTCACCGG-3' AND 5'- CCGGTGAACAGCTCGCTAAAGACCCCGC-3'.

	Atkinson et al., 2011)	
pNup58-mEGFP41 2(-5):	*pNup58-mEGFP41 2(-4)*	5’- AAAATGTTTTTGGGTGAGGAGCTGTTCACC-3’ AND 5’- GGTGAACAGCTCCTCACCCAAAAACATTTT-3’.
pNup58-mEGFP41 2(-6):	*pNup58-mEGFP41 2(-4)*	5’- AAAATGTTTTTGGGTGAGCTGTTCACCGGG-3’ AND 5’- CCCGGTGAACAGCTCACCCAAAAACATTTT-3’.
pmCherry-C1-RanT24L:	pmCherry-C1-RanQ69L (gift of Jay Brenman)	5’- TGGGACACAGCCGGCCAAGAGAAATTCGGTGGA-3’ AND 5’- TCCACCGAATTTCTCTTGGCCGGCTGTGTCCCA-3’ AND AGAIN WITH 5’- GGTACTGGAAAATTGACCTTCGTGAAACGTCAT-3’ AND 5’- ATGACGTTTCACGAAGGTCAATTTTCCAGTACC-3’.

Part 5: Building CRISPR Cell Lines

Guides and repair templates were constructed by using the Benchling CRISPR design tool (Benchling). Guides were cloned into the *pSpCas9(BB)-2A-Puro (PX459) V2.0* plasmid following standard protocols as developed by the Zhang lab (Ran et al., 2013). The guide for Nup54 5'-CGATCTAGAAGATATAAAGC-3' and guide for Nup133 were 5'-GCTCAGTGAGTACTTACCGG-3'. (Cloning primers: Nup54, 5'CACCCGATCTAGAAGATATAAAGC-3' and 5'-AAAC GCTTTATATCTTCTAGATCG-3'. Nup133 5'-CACCGCTCAGTGAGTACTTACCGG-3' and 5'-AAAC CCGGTAAGTACTCACTGAGC-3'.)

The repair templates (for Nup54-mEGFP(0) and Nup133-mEGFP(-8) were synthesized by GenScript as dsDNA. This DNA was then A'-tailed and placed in a TOPO-TA Cloning Vector (2.1-TOPO, ThermoFisher Scientific).

Repair templates for Nup54-mEGFP(1) and Nup-mEGFP(2) and Nup133-mEGFP(-7) were cloned from the repair template plasmids constructed above via the QuikChange Lightning Site-Directed Mutagenesis Kit (Agilent) with the following primer pairs:

TABLE 8: Table of Site-Directed Mutagenesis Primers for Cloning CRISPR HDR Plasmids.

Plasmid	Parent Plasmid	Primers
Nup54-mEGFP(1) Repair Template	Nup54-mEGFP(0) Repair Template	5'-CAAGCTGGTAGCAGAAGCTGCTGCAAAGGAGGAGCTGTTCAC-3' AND 5'-GTGAACAGCTCCTCCTTTGCAGCAGCTTCTGCTACCAGCTTG-3'
Nup54-mEGFP(1) Repair Template	Nup54-mEGFP(0) Repair Template	5'-CAAGCTGGTAGCAGAAGCTGCTGCAAAGGAGGAGCTGTTC-3' AND 5'-GAACAGCTCCTCCTTTGCAGCAGCTTCTGCTACCAGCTTG

		-3’.
Nup133-mEGFP(-7) Repair Template	Nup133-mEGFP(-8) Repair Template	5’-GAAAGCAAATTATGAATATTATGTTCAGGGAGAGCTGTTCACCGGGGTGGTGCCCATC-3’ AND 5’-GATGGGCACCACCCCGGTGAACAGCTCTCCCTGAACATAATATTCATAATTTGCTTTC-3’.

Plasmids containing the repair templates were digested with XhoI (New England BioLabs) and gel purified.

For each CRISPR cell line, 3 wells of a 6 well plate were seeded with low passage number (~p4) HAP1 cells. These cells were transfected with FuGENE HD (Promega) with a Reagent : DNA ratio of 3 : 1 (20 uL FUGENE HD: 3.67 ug linearized HDR and 3.0 ug pSpCas9(BB)-2A-Puro(PX459)V2.0 containing the appropriate guide) according to manufacturer’s protocol. Transfected cells were selected via antibiotic selection with puromycin (Sigma: 0.6 ug/mL) for 48 hours. Cells were released from antibiotic selection and allowed to recover for 24 hours. GFP positive cells were collected in the Rockefeller University Flow Cytometry Resource Center using a FACSAria II flow cytometer (BD Biosciences). Cells were

resuspended in PBS (no calcium/no magnesium, Gibco), 0.5% (vol/vol) bovine serum albumin (BSA, VWR International), 5mM EDTA (Gibco), and 15 mM HEPES (ThermoFischer). GFP positive cells were sorted to 96 wells and screened via live cell microscopy for signal at the nuclear rim (~95% of GFP positive cells showed nuclear rim GFP signal).

PCR: Cell lines were screened for homozygosity via PCR. For Nup54, primers were 5'-CCTGTGACTAGCTTGCAGTT-3' and 5'-ACCTCTGATGTGGATGGTTTC-3'. These primer pairs should yield a product of ~896 bp if mEGFP is present and ~197 bp if mEGFP is absent. For Nup133, primers were 5'-AGTCCAATCCTTACTTCGAGTTT-3' and 5'- AGGAACAACAACTGACACATTTC -3'. These primer pairs should yield a product of ~982 bp if mEGFP is present and ~283 bp if mEGFP is absent. Two bands were seen for heterozygotes and one band for homozygotes, both fragments were sequenced to confirm amplification of correct region and proper incorporation of the mEGFP.

Westerns: In order to confirm that the mEGFP was not incorporated elsewhere an producing another labeled protein within our cells, western blots were performed. Protein samples were run on a 4-12% Tris-Glycine gel (Novex) and were Western blotting with the following antibodies: α-GFP (Clontech Living Colors 632381 (JL-8), mouse monoclonal, 1:1,000), and goat α-mouse–HRP (Sigma–Aldrich A-9917, 1:50,000), α-bactin (Sigma–Aldrich Ac-74, 1:1,000), and goat α-rabbit–HRP (Sigma–Aldrich A-0545, 1:50,000). All blocking and incubations were done in 5% (wt/vol) nonfat milk powder in Tris-buffered saline with Tween 20.

REFERENCES

Adam, S., Sterne-Marr, R., and Gerace, L. (1992). Nuclear protein import using digitonin-permeabilized cells. Methods Enzymol *219*, 97–110.

Ader, C., Frey, S., Maas, W., Schmidt, H., Görlich, D., and Baldus, M. (2010). Amyloid-like interactions within nucleoporin FG hydrogels. Proc National Acad Sci *107*, 6281–6285.

Adl, S.M., Simpson, A.G., Lane, C.E., Lukeš, J., Bass, D., Bowser, S.S., Brown, M.W., Burki, F., Dunthorn, M., Hampl, V., et al. (2012). The Revised Classification of Eukaryotes. J Eukaryot Microbiol *59*, 429–514.

Alber, F., Dokudovskaya, S., Veenhoff, L.M., Zhang, W., Kipper, J., Devos, D., Suprapto, A., Karni-Schmidt, O., Williams, R., Chait, B.T., et al. (2007a). Determining the architectures of macromolecular assemblies. Nature *450*, 683.

Alber, F., Dokudovskaya, S., Veenhoff, L.M., Zhang, W., Kipper, J., Devos, D., Suprapto, A., Karni-Schmidt, O., Williams, R., Chait, B.T., et al. (2007b). The molecular architecture of the nuclear pore complex. Nature *450*, 695.

Alberts, J.B. (2009). Biophysically Realistic Filament Bending Dynamics in Agent-Based Biological Simulation. Plos One *4*, e4748.

Allen, N.P., Huang, L., Burlingame, A., and Rexach, M. (2001). Proteomic Analysis of Nucleoporin Interacting Proteins. J Biol Chem *276*, 29268–29274.

Anantharam, A., Axelrod, D., and Holz, R.W. (2010a). Polarized TIRFM Reveals Changes in Plasma Membrane Topology Before and During Granule Fusion. Cell Mol Neurobiol *30*, 1343–1349.

Anantharam, A., Onoa, B., Edwards, R.H., Holz, R.W., and Axelrod, D. (2010b). Localized topological changes of the plasma membrane upon exocytosis visualized by polarized TIRFM. J Cell Biology *188*, 415–428.

Ando, D., Zandi, R., Kim, Y., Colvin, M., Rexach, M., and Gopinathan, A. (2014). Nuclear Pore Complex Protein Sequences Determine Overall Copolymer Brush Structure and Function. Biophys J *106*, 1997–2007.

Andrews, S.S. (2014). Methods for modeling cytoskeletal and DNA filaments. Phys Biol *11*, 011001.

von Appen, A., and Beck, M. (2016). Structure Determination of the Nuclear Pore Complex with Three-Dimensional Cryo electron Microscopy. J Mol Biol *428*, 2001–2010.

von Appen, A., Kosinski, J., Sparks, L., Ori, A., DiGuilio, A.L., Vollmer, B., Mackmull, M.-T., Banterle, N., Parca, L., Kastritis, P., et al. (2015). In situ structural analysis of the human nuclear pore complex. Nature *526*, 140.

Atkinson, C.E., Mattheyses, A.L., Kampmann, M., and Simon, S.M. (2013). Conserved Spatial Organization of FG Domains in the Nuclear Pore Complex. Biophys J *104*, 37–50.

Bayliss, R., Ribbeck, K., Akin, D., Kent, H.M., Feldherr, C.M., Görlich, D., and Stewart, M. (1999). Interaction between NTF2 and xFxFG-containing nucleoporins is required to mediate nuclear import of RanGDP 11Edited by I. B. Holland. J Mol Biol *293*, 579–593.

Bayliss, R., Littlewood, T., Strawn, L.A., Wente, S.R., and Stewart, M. (2002). GLFG and FxFG Nucleoporins Bind to Overlapping Sites on Importin-β. J Biol Chem *277*, 50597–50606.

Beausang, J.F., Schroeder, H.W., Nelson, P.C., and Goldman, Y.E. (2008). Twirling of Actin by Myosins II and V Observed via Polarized TIRF in a Modified Gliding Assay. Biophys J *95*, 5820–5831.

Beck, M., and Hurt, E. (2016). The nuclear pore complex: understanding its function through structural insight. Nat Rev Mol Cell Bio *18*, 73–89.

Beck, M., Förster, F., Ecke, M., Plitzko, J.M., Melchior, F., Gerisch, G., Baumeister, W., and Medalia, O. (2004). Nuclear Pore Complex Structure and Dynamics Revealed by Cryoelectron Tomography. Science *306*, 1387–1390.

Berke, I.C., Boehmer, T., Blobel, G., and Schwartz, T.U. (2004). Structural and functional analysis of Nup133 domains reveals modular building blocks of the nuclear pore complex. J Cell Biology *167*, 591–597.

Bleck, M., Itano, M.S., Johnson, D.S., Thomas, K.V., North, A.J., Bieniasz, P.D., and Simon, S.M. (2014). Temporal and spatial organization of ESCRT protein recruitment during HIV-1 budding. Proc National Acad Sci *111*, 12211–12216.

Brohawn, S.G., Leksa, N.C., Spear, E.D., Rajashankar, K.R., and Schwartz, T.U. (2008). Structural Evidence for Common Ancestry of the Nuclear Pore Complex and Vesicle Coats. Science *322*, 1369–1373.

Bui, K., von Appen, A., DiGuilio, A.L., Ori, A., Sparks, L., Mackmull, M.-T., Bock, T., Hagen, W., Andrés-Pons, A., Glavy, J.S., et al. (2013). Integrated Structural Analysis of the Human Nuclear Pore Complex Scaffold. Cell *155*, 1233–1243.

Burghardt, T.P. (1984). Model-Independent fluorescence polarization for measuring order in a biological assembly. Biopolymers *23*, 2383–2406.

Cassany, A., and Gerace, L. (2008). The Nucleus, Volume 2: Chromatin, Transcription, Envelope, Proteins, Dynamics, and Imaging. Methods Mol Biology Clifton N J *464*, 181–205.

Chen, X., Zaro, J.L., and Shen, W.-C. (2013). Fusion protein linkers: Property, design and functionality. Adv Drug Deliver Rev *65*, 1357–1369.

Chug, H., Trakhanov, S., Hülsmann, B.B., Pleiner, T., and Görlich, D. (2015). Crystal structure of the metazoan Nup62•Nup58•Nup54 nucleoporin complex. Science *350*, 106–110.

Corrie, J., Brandmeier, B., Ferguson, R., Trentham, D., Kendrick-Jones, J., Hopkins, S., van der Heide, U., Goldman, Y., Sabido-David, C., Dale, R., et al. (1999). Dynamic measurement of myosin light-chain-domain tilt and twist in muscle contraction. Nature *400*, 425.

Counterman, A.E., and Clemmer, D.E. (1999). Volumes of Individual Amino Acid Residues in Gas-Phase Peptide Ions. J Am Chem Soc *121*, 4031–4039.

Crampton, N., Kodiha, M., Shrivastava, S., Umar, R., and Stochaj, U. (2009). Oxidative Stress Inhibits Nuclear Protein Export by Multiple Mechanisms That Target FG Nucleoporins and Crm1. Mol Biol Cell *20*, 5106–5116.

Cronshaw, J.M., Krutchinsky, A.N., Zhang, W., Chait, B.T., and Matunis, M.J. (2002). Proteomic analysis of the mammalian nuclear pore complex. J Cell Biology *158*, 915–927.

Dale, R.E., Hopkins, S.C., an der Heide, U.A., Marszałek, T., Irving, M., and Goldman, Y.E. (1999). Model-Independent Analysis of the Orientation of Fluorescent Probes with Restricted Mobility in Muscle Fibers. Biophys J *76*, 1606–1618.

Dange, T., Grünwald, D., Grünwald, A., Peters, R., and Kubitscheck, U. (2008). Autonomy and robustness of translocation through the nuclear pore complex: a single-molecule study. J Cell Biology *183*, 77–86.

D'Angelo, M.A., Gomez-Cavazos, S.J., Mei, A., Lackner, D.H., and Hetzer, M.W. (2012). A Change in Nuclear Pore Complex Composition Regulates Cell Differentiation. Dev Cell *22*, 446–458.

DeGrasse, J.A., DuBois, K.N., Devos, D., Siegel, N.T., Sali, A., Field, M.C., Rout, M.P., and Chait, B.T. (2009). Evidence for a Shared Nuclear Pore Complex Architecture That Is Conserved from the Last Common Eukaryotic Ancestor. Mol Cell Proteom Mcp *8*, 2119–2130.

Delavoie, F., Soldan, V., Rinaldi, D., Dauxois, J.-Y., and Gleizes, P.-E. (2019). The

path of pre-ribosomes through the nuclear pore complex revealed by electron tomography. Nat Commun *10*, 497.

Devos, D., Dokudovskaya, S., Alber, F., Williams, R., Chait, B.T., Sali, A., and Rout, M.P. (2004). Components of Coated Vesicles and Nuclear Pore Complexes Share a Common Molecular Architecture. Plos Biol *2*, e380.

Devos, D., Dokudovskaya, S., Williams, R., Alber, F., Eswar, N., Chait, B.T., Rout, M.P., and Sali, A. (2006). Simple fold composition and modular architecture of the nuclear pore complex. P Natl Acad Sci Usa *103*, 2172–2177.

Drin, G., Casella, J.-F., Gautier, R., Boehmer, T., Schwartz, T.U., and Antonny, B. (2007). A general amphipathic α-helical motif for sensing membrane curvature. Nat Struct Mol Biology *14*, nsmb1194.

Eibauer, M., Pellanda, M., Turgay, Y., Dubrovsky, A., Wild, A., and Medalia, O. (2015). Structure and gating of the nuclear pore complex. Nat Commun *6*, 7532.

Elsliger, M.-A., Wachter, R.M., Hanson, G.T., Kallio, K., and Remington, J.S. (1999). Structural and Spectral Response of Green Fluorescent Protein Variants to Changes in pH†,‡. Biochemistry-Us *38*, 5296–5301.

Eppenga, R., and Frenkel, D. (2006). Monte Carlo study of the isotropic and nematic

phases of infinitely thin hard platelets. Mol Phys *52*, 1303–1334.

Fahrenkrog, B., Hurt, E.C., Aebi, U., and Panté, N. (1998). Molecular Architecture of the Yeast Nuclear Pore Complex: Localization of Nsp1p Subcomplexes. J Cell Biology *143*, 577–588.

Feldherr, C., and Akin, D. (1990). The permeability of the nuclear envelope in dividing and nondividing cell cultures. J Cell Biology *111*, 1–8.

Fernandez-Martinez, J., Phillips, J., Sekedat, M.D., Diaz-Avalos, R., Velazquez-Muriel, J., Franke, J.D., Williams, R., Stokes, D.L., Chait, B.T., Sali, A., et al. (2012). Structure–function mapping of a heptameric module in the nuclear pore complex. J Cell Biology *196*, 419–434.

Finlay, D., Newmeyer, D., Price, T., and Forbes, D. (1987). Inhibition of in vitro nuclear transport by a lectin that binds to nuclear pores. J Cell Biology *104*, 189–200.

Finlay, D., Meier, E., Bradley, P., Horecka, J., and Forbes, D. (1991). A complex of nuclear pore proteins required for pore function. J Cell Biology *114*, 169–183.

Fischer, J., Teimer, R., Amlacher, S., Kunze, R., and Hurt, E. (2015). Linker Nups connect the nuclear pore complex inner ring with the outer ring and transport

channel. Nat Struct Mol Biol *22*, 774–781.

Franks, T.M., Benner, C., Narvaiza, I., Marchetto, M., Young, J.M., Malik, H.S., Gage, F.H., and Hetzer, M.W. (2016). Evolution of a transcriptional regulator from a transmembrane nucleoporin. Gene Dev *30*, 1155–1171.

Frey, S., and Görlich, D. (2007). A Saturated FG-Repeat Hydrogel Can Reproduce the Permeability Properties of Nuclear Pore Complexes. Cell *130*, 512–523.

Frey, S., Richter, R.P., and Görlich, D. (2006). FG-Rich Repeats of Nuclear Pore Proteins Form a Three-Dimensional Meshwork with Hydrogel-Like Properties. Science *314*, 815–817.

Gamini, R., Han, W., Stone, J.E., and Schulten, K. (2014). Assembly of Nsp1 Nucleoporins Provides Insight into Nuclear Pore Complex Gating. Plos Comput Biol *10*, e1003488.

Ghavami, A., Veenhoff, L.M., van der Giessen, E., and Onck, P.R. (2014). Probing the Disordered Domain of the Nuclear Pore Complex through Coarse-Grained Molecular Dynamics Simulations. Biophys J *107*, 1393–1402.

Gomez-Cavazos, S.J., and Hetzer, M.W. (2015). The nucleoporin gp210/Nup210 controls muscle differentiation by regulating nuclear envelope/ER homeostasis. J

Cell Biology *208*, 671–681.

Görlich, D., and Kutay, U. (1999). TRANSPORT BETWEEN THE CELL NUCLEUS AND THE CYTOPLASM. Annu Rev Cell Dev Bi *15*, 607–660.

Göttlinger, H., Sodroski, J., and Haseltine, W. (1989). Role of capsid precursor processing and myristoylation in morphogenesis and infectivity of human immunodeficiency virus type 1. Proc National Acad Sci *86*, 5781–5785.

Griffin, A.B., Adams, S.R., and Tsien, R.Y. (1998). Specific Covalent Labeling of Recombinant Protein Molecules Inside Live Cells. Science *281*, 269–272.

Guan, T., Müller, S., Klier, G., Panté, N., Blevitt, J., Haner, M., Paschal, B., Aebi, U., and Gerace, L. (1995). Structural analysis of the p62 complex, an assembly of O-linked glycoproteins that localizes near the central gated channel of the nuclear pore complex. Mol Biol Cell *6*, 1591–1603.

Gustin, K.E., and Sarnow, P. (2001). Effects of poliovirus infection on nucleo-cytoplasmic trafficking and nuclear pore complex composition. Embo J *20*, 240–249.

Hayama, R., Sparks, S., Hecht, L.M., Dutta, K., Karp, J.M., Cabana, C.M., Rout, M.P., and Cowburn, D. (2018). Thermodynamic characterization of the multivalent interactions underlying rapid and selective translocation through the nuclear pore

complex. J Biol Chem *293*, 4555–4563.

Hoelz, A., Debler, E.W., and Blobel, G. (2011). The Structure of the Nuclear Pore Complex. Biochemistry-Us *80*, 613–643.

Hülsmann, B.B., Labokha, A.A., and Görlich, D. (2012). The Permeability of Reconstituted Nuclear Pores Provides Direct Evidence for the Selective Phase Model. Cell *150*, 738–751.

Inoué, S., Shimomura, O., Goda, M., Shribak, M., and Tran, P. (2002). Fluorescence polarization of green fluorescence protein. Proc National Acad Sci *99*, 4272–4277.

Jiang, C.-J., Imamoto, N., Matsuki, R., Yoneda, Y., and Yamamoto, N. (1998). In vitro characterization of rice importin β1: molecular interaction with nuclear transport factors and mediation of nuclear protein import. Febs Lett *437*, 127–130.

Johnson, D.S., Toledo-Crow, R., Mattheyses, A.L., and Simon, S.M. (2014). Polarization-Controlled TIRFM with Focal Drift and Spatial Field Intensity Correction. Biophys J *106*, 1008–1019.

Johnson, D.S., Bleck, M., and Simon, S.M. (2018). Timing of ESCRT-III protein recruitment and membrane scission during HIV-1 assembly. Elife *7*, e36221.

Johnson, D.S., Bleck, M., and Simon, S.M. (2019). Recruitment Dynamics of Escrt-III Proteins during HIV-1 Gag Assembly and Plasma Membrane Scission. Biophys J *116*, 373a.

Jouvenet, N., Neil, S.J., Bess, C., Johnson, M.C., Virgen, C.A., Simon, S.M., and Bieniasz, P.D. (2006). Plasma Membrane Is the Site of Productive HIV-1 Particle Assembly. Plos Biol *4*, e435.

Jouvenet, N., Bieniasz, P.D., and Simon, S.M. (2008). Imaging the biogenesis of individual HIV-1 virions in live cells. Nature *454*, 236.

Jouvenet, N., Zhadina, M., Bieniasz, P.D., and Simon, S.M. (2011). Dynamics of ESCRT protein recruitment during retroviral assembly. Nat Cell Biol *13*, 394.

Jovanovic-Talisman, T., Tetenbaum-Novatt, J., McKenney, A.S., Zilman, A., Peters, R., Rout, M.P., and Chait, B.T. (2009). Artificial Nanopores that Mimic the Transport Selectivity of the Nuclear Pore Complex. Biophys J *96*, 545a.

Kampmann, M., and Blobel, G. (2009). Three-dimensional structure and flexibility of a membrane-coating module of the nuclear pore complex. Nat Struct Mol Biol *16*, 782–788.

Kampmann, M., Atkinson, C.E., Mattheyses, A.L., and Simon, S.M. (2011). Mapping

the orientation of nuclear pore proteins in living cells with polarized fluorescence microscopy. Nat Struct Mol Biol *18*, 643.

Kapinos, L.E., Schoch, R.L., Wagner, R.S., Schleicher, K.D., and Lim, R. (2014). Karyopherin-Centric Control of Nuclear Pores Based on Molecular Occupancy and Kinetic Analysis of Multivalent Binding with FG Nucleoporins. Biophys J *106*, 1751–1762.

Kaplan, A., Manchester, M., and Swanstrom, R. (1994). The activity of the protease of human immunodeficiency virus type 1 is initiated at the membrane of infected cells before the release of viral proteins and is required for release to occur with maximum efficiency. J Virol *68*, 6782–6786.

Kelley, K., Knockenhauer, K.E., Kabachinski, G., and Schwartz, T.U. (2015). Atomic structure of the Y complex of the nuclear pore. Nat Struct Mol Biol *22*, 425–431.

Keminer, O., and Peters, R. (1999). Permeability of Single Nuclear Pores. Biophys J *77*, 217–228.

Kiessling, V., Domanska, M.K., and Tamm, L.K. (2010). Single SNARE-Mediated Vesicle Fusion Observed In Vitro by Polarized TIRFM. Biophys J *99*, 4047–4055.

Kim, S., Fernandez-Martinez, J., Nudelman, I., Shi, Y., Zhang, W., Raveh, B.,

Herricks, T., Slaughter, B.D., Hogan, J.A., Upla, P., et al. (2018). Integrative structure and functional anatomy of a nuclear pore complex. Nature *555*, 475.

Kiseleva, E., Goldberg, M.W., Daneholt, B., and Allen, T.D. (1996). RNP Export is Mediated by Structural Reorganization of the Nuclear Pore Basket. J Mol Biol *260*, 304–311.

Kiseleva, E., Goldberg, M., Allen, T., and Akey, C. (1998). Active nuclear pore complexes in Chironomus: visualization of transporter configurations related to mRNP export. J Cell Sci *111 (Pt 2)*, 223–236.

Kiseleva, E., Allen, T.D., Rutherford, S., Bucci, M., Wente, S.R., and Goldberg, M.W. (2004). Yeast nuclear pore complexes have a cytoplasmic ring and internal filaments. J Struct Biol *145*, 272–288.

Kita, K., Omata, S., and Horigome, T. (1993). Purification and Characterization of a Nuclear Pore Glycoprotein Complex Containing p62. J Biochem *113*, 377–382.

Kodiha, M., Tran, D., Morogan, A., Qian, C., and Stochaj, U. (2009). Dissecting the Signaling Events That Impact Classical Nuclear Import and Target Nuclear Transport Factors. Plos One *4*, e8420.

Kohl, N., Emini, E., Schleif, W., Davis, L., Heimbach, J., Dixon, R., olnick, E., and

Sigal, I. (1988). Active human immunodeficiency virus protease is required for viral infectivity. Proc National Acad Sci *85*, 4686–4690.

Kosinski, J., Mosalaganti, S., von Appen, A., Teimer, R., DiGuilio, A.L., Wan, W., Bui, K., Hagen, W., Briggs, J.A., Glavy, J.S., et al. (2016). Molecular architecture of the inner ring scaffold of the human nuclear pore complex. Science *352*, 363–365.

Kraemer, D., Wozniak, R., Blobel, G., and Radu, A. (1994). The human CAN protein, a putative oncogene product associated with myeloid leukemogenesis, is a nuclear pore complex protein that faces the cytoplasm. Proc National Acad Sci *91*, 1519–1523.

Kuss, S.K., Mata, M.A., Zhang, L., and Fontoura, B.M. (2013). Nuclear Imprisonment: Viral Strategies to Arrest Host mRNA Nuclear Export. Viruses *5*, 1824–1849.

Kutay, U., Hartmann, E., Treichel, N., Calado, A., Carmo-Fonseca, M., Prehn, S., Kraft, R., Görlich, D., and Bischoff, R.F. (2000). Identification of Two Novel RanGTP-binding Proteins Belonging to the Importin β Superfamily. J Biol Chem *275*, 40163–40168.

Lei, E.P., and Silver, P.A. (2002). Protein and RNA Export from the Nucleus. Dev Cell *2*, 261–272.

Liashkovich, I., Meyring, A., Kramer, A., and Shahin, V. (2011). Exceptional structural and mechanical flexibility of the nuclear pore complex. J Cell Physiol *226*, 675–682.

Lim, R.Y., Fahrenkrog, B., Köser, J., Schwarz-Herion, K., Deng, J., and Aebi, U. (2007). Nanomechanical Basis of Selective Gating by the Nuclear Pore Complex. Science *318*, 640–643.

Lin, D.H., Stuwe, T., Schilbach, S., Rundlet, E.J., Perriches, T., Mobbs, G., Fan, Y., Thierbach, K., Huber, F.M., Collins, L.N., et al. (2016). Architecture of the symmetric core of the nuclear pore. Science *352*, aaf1015.

Liu, X., Mitchell, J.M., Wozniak, R.W., Blobel, G., and Fan, J. (2012). Structural evolution of the membrane-coating module of the nuclear pore complex. Proc National Acad Sci *109*, 16498–16503.

Loeb, D., Hutchison, C., Edgell, M., Farmerie, W., and Swanstrom, R. (1989). Mutational analysis of human immunodeficiency virus type 1 protease suggests functional homology with aspartic proteinases. J Virol *63*, 111–121.

Lupu, F., Alves, A., Anderson, K., Doye, V., and Lacy, E. (2008). Nuclear Pore Composition Regulates Neural Stem/Progenitor Cell Differentiation in the Mouse

Embryo. Dev Cell *14*, 831–842.

Mattheyses, A.L., Kampmann, M., Atkinson, C.E., and Simon, S.M. (2010). Fluorescence Anisotropy Reveals Order and Disorder of Protein Domains in the Nuclear Pore Complex. Biophys J *99*, 1706–1717.

Mehlin, H., Skoglund, U., and Daneholt, B. (1991). Transport of Balbiani ring granules through nuclear pores in Chironomus tentans. Exp Cell Res *193*, 72–77.

Melčák, I., Hoelz, A., and Blobel, G. (2007). Structure of Nup58/45 Suggests Flexible Nuclear Pore Diameter by Intermolecular Sliding. Science *315*, 1729–1732.

Miao, L., and Schulten, K. (2010). Probing a Structural Model of the Nuclear Pore Complex Channel through Molecular Dynamics. Biophys J *98*, 1658–1667.

Mincer, J.S., and Simon, S.M. (2011). Simulations of nuclear pore transport yield mechanistic insights and quantitative predictions. Proc National Acad Sci *108*, E351–E358.

Monette, A., Panté, N., and Mouland, A.J. (2011). HIV-1 remodels the nuclear pore complex. J Cell Biology *193*, 619–631.

Moore, M., and Blobel, G. (1993). The GTP-binding protein Ran/TC4 is required for

protein import into the nucleus. Nature *365*, 365661a0.

Mosalaganti, S., Kosinski, J., Albert, S., Schaffer, M., Strenkert, D., Salomé, P.A., Merchant, S.S., Plitzko, J.M., Baumeister, W., Engel, B.D., et al. (2018). In situ architecture of the algal nuclear pore complex. Nat Commun *9*, 2361.

Moussavi-Baygi, R., and Mofrad, M. (2016). Rapid Brownian Motion Primes Ultrafast Reconstruction of Intrinsically Disordered Phe-Gly Repeats Inside the Nuclear Pore Complex. Sci Rep-Uk *6*, 29991.

Moussavi-Baygi, R., Jamali, Y., Karimi, R., and Mofrad, M.R. (2011a). Brownian Dynamics Simulation of Nucleocytoplasmic Transport: A Coarse-Grained Model for the Functional State of the Nuclear Pore Complex. Plos Comput Biol *7*, e1002049.

Moussavi-Baygi, R., Jamali, Y., Karimi, R., and Mofrad, M.R.K. (2011b). Biophysical Coarse-Grained Modeling Provides Insights into Transport through the Nuclear Pore Complex. Biophys J *100*, 1410–1419.

Neumann, N., Lundin, D., and Poole, A.M. (2010). Comparative Genomic Evidence for a Complete Nuclear Pore Complex in the Last Eukaryotic Common Ancestor. Plos One *5*, e13241.

Niopek, D., Benzinger, D., Roensch, J., Draebing, T., Wehler, P., Eils, R., and

Ventura, B. (2014). Engineering light-inducible nuclear localization signals for precise spatiotemporal control of protein dynamics in living cells. Nat Commun *5*, 4404.

Obado, S.O., Brillantes, M., Uryu, K., Zhang, W., Ketaren, N.E., Chait, B.T., Field, M.C., and Rout, M.P. (2016). Interactome Mapping Reveals the Evolutionary History of the Nuclear Pore Complex. Plos Biol *14*, e1002365.

Oreopoulos, J., and Yip, C.M. (2009). Probing Membrane Order and Topography in Supported Lipid Bilayers by Combined Polarized Total Internal Reflection Fluorescence-Atomic Force Microscopy. Biophys J *96*, 1970–1984.

Oreopoulos, J., Epand, R.M., Epand, R.M., and Yip, C.M. (2010). Peptide-Induced Domain Formation in Supported Lipid Bilayers: Direct Evidence By Combined Atomic Force and Polarized Total Internal Reflection Fluorescence Microscopy. Biophys J *98*, 86a.

Ori, A., Banterle, N., Iskar, M., Andrés-Pons, A., Escher, C., Bui, H., Sparks, L., Solis-Mezarino, V., Rinner, O., Bork, P., et al. (2013). Cell type-specific nuclear pores: a case in point for context-dependent stoichiometry of molecular machines. Mol Syst Biol *9*, 648.

Pack, C.-G., Yukii, H., Toh-e, A., Kudo, T., Tsuchiya, H., Kaiho, A., Sakata, E.,

Murata, S., Yokosawa, H., Sako, Y., et al. (2014). Quantitative live-cell imaging reveals spatio-temporal dynamics and cytoplasmic assembly of the 26S proteasome. Nat Commun *5*, 3396.

Paine, P.L., and Feldherr, C.M. (1972). Nucleocytoplasmic exchange of macromolecules. Exp Cell Res *74*, 81–98.

Paine, P.L., Moore, L.C., and Horowitz, S.B. (1975). Nuclear envelope permeability. Nature *254*, 109–114.

Patel, S.S., Belmont, B.J., Sante, J.M., and Rexach, M.F. (2007). Natively Unfolded Nucleoporins Gate Protein Diffusion across the Nuclear Pore Complex. Cell *129*, 83–96.

Peters, R. (2009). Functionalization of a nanopore: The nuclear pore complex paradigm. Biochimica Et Biophysica Acta Bba - Mol Cell Res *1793*, 1533–1539.

Peyro, M., Soheilypour, M., Lee, B.L., and Mofrad, M.R.K. (2015a). Evolutionarily Conserved Sequence Features Regulate the Formation of the FG Network at the Center of the Nuclear Pore Complex. Sci Rep-Uk *5*, 15795.

Peyro, M., Soheilypour, M., Ghavami, A., and Mofrad, M.R. (2015b). Nucleoporin's Like Charge Regions Are Major Regulators of FG Coverage and Dynamics Inside

the Nuclear Pore Complex. Plos One *10*, e0143745.

Piston, D.W., and Rizzo, M.A. (2008). Methods in Cell Biology. Methods Cell Biol *85*, 415–430.

Pulupa, J., Rachh, M., Tomasini, M.D., Mincer, J.S., and Simon, S.M. (2017). A coarse-grained computational model of the nuclear pore complex predicts Phe-Gly nucleoporin dynamics. J Gen Physiology *149*, jgp.201711769.

Rabut, G., Doye, V., and Ellenberg, J. (2004). Mapping the dynamic organization of the nuclear pore complex inside single living cells. Nat Cell Biol *6*, ncb1184.

Radu, A., Blobel, G., and Moore (1995). Identification of a protein complex that is required for nuclear protein import and mediates docking of import substrate to distinct nucleoporins. Proc National Acad Sci *92*, 1769–1773.

Rangl, M., Ebner, A., Yamada, J., Rexach, M., and Hinterdorfer, P. (2012). Single-Molecule Analysis of the Recognition Forces Underlying Nucleo-Cytoplasmic Transport. Biophys J *102*, 12a.

Reichelt, R., Holzenburg, A., Buhle, E., Jarnik, M., Engel, A., and Aebi, U. (1990). Correlation between structure and mass distribution of the nuclear pore complex and of distinct pore complex components. J Cell Biology *110*, 883–894.

Ribbeck, K., and Görlich, D. (2001). Kinetic analysis of translocation through nuclear pore complexes. Embo J *20*, 1320–1330.

Rizzo, M.A., and Piston, D.W. (2005). High-Contrast Imaging of Fluorescent Protein FRET by Fluorescence Polarization Microscopy. Biophys J *88*, L14–L16.

Rout, M.P., Aitchison, J.D., Suprapto, A., Hjertaas, K., Zhao, Y., and Chait, B.T. (2000). The Yeast Nuclear Pore Complex Composition, Architecture, and Transport Mechanism. J Cell Biology *148*, 635–652.

Rout, M.P., Aitchison, J.D., Magnasco, M.O., and Chait, B.T. (2003). Virtual gating and nuclear transport: the hole picture. Trends Cell Biol *13*, 622–628.

Satterly, N., Tsai, P.-L., van Deursen, J., Nussenzveig, D.R., Wang, Y., Faria, P.A., Levay, A., Levy, D.E., and Fontoura, B.M. (2007). Influenza virus targets the mRNA export machinery and the nuclear pore complex. Proc National Acad Sci *104*, 1853–1858.

Schwoebel, E.D., Talcott, B., Cushman, I., and Moore, M. (1998). Ran-dependent Signal-mediated Nuclear Import Does Not Require GTP Hydrolysis by Ran. J Biol Chem *273*, 35170–35175.

Sellés, J., Penrad-Mobayed, M., Guillaume, C., Fuger, A., Auvray, L., Faklaris, O., and Montel, F. (2017). Nuclear pore complex plasticity during developmental process as revealed by super-resolution microscopy. Sci Rep-Uk *7*, 14732.

Shabman, R.S., Gulcicek, E.E., Stone, K.L., and Basler, C.F. (2011). The Ebola Virus VP24 Protein Prevents hnRNP C1/C2 Binding to Karyopherin α1 and Partially Alters its Nuclear Import. J Infect Dis *204*, S904–S910.

Shulga, N., Roberts, P., Gu, Z., Spitz, L., Tabb, M., Nomura, M., and Goldfarb, D. (1996). In vivo nuclear transport kinetics in Saccharomyces cerevisiae: a role for heat shock protein 70 during targeting and translocation. J Cell Biology *135*, 329–339.

Simon, D.N., and Rout, M.P. (2014). Cancer Biology and the Nuclear Envelope, Recent Advances May Elucidate Past Paradoxes. 285–307.

Simon, S.M., Peskin, C., and Oster, G. (1992). What drives the translocation of proteins? Proc National Acad Sci *89*, 3770–3774.

Siniossoglou, S., Wimmer, C., Rieger, M., Doye, V., Tekotte, H., Weise, C., Emig, S., Segref, A., and Hurt, E.C. (1996). A Novel Complex of Nucleoporins, Which Includes Sec13p and a Sec13p Homolog, Is Essential for Normal Nuclear Pores. Cell *84*, 265–275.

Smith, A.E., Slepchenko, B.M., Schaff, J.C., Loew, L.M., and Macara, I.G. (2002). Systems Analysis of Ran Transport. Science *295*, 488–491.

Solmaz, S.R., Chauhan, R., Blobel, G., and Melčák, I. (2011). Molecular Architecture of the Transport Channel of the Nuclear Pore Complex. Cell *147*, 590–602.

Solmaz, S.R., Blobel, G., and Melčák, I. (2013). Ring cycle for dilating and constricting the nuclear pore. Proc National Acad Sci *110*, 5858–5863.

Stanley, G.J., Fassati, A., and Hoogenboom, B.W. (2018). Atomic force microscopy reveals structural variability amongst nuclear pore complexes. Life Sci Alliance *1*, e201800142.

Stochaj, U., Rassadi, R., and Chiu, J. (2000). Stress-mediated inhibition of the classical nuclear protein import pathway and nuclear accumulation of the small GTPase Gsp1p1. Faseb J *14*, 2130–2132.

Strambio-de-Castillia, C., Blobel, G., and Rout, M.P. (1999). Proteins Connecting the Nuclear Pore Complex with the Nuclear Interior. J Cell Biology *144*, 839–855.

Stuwe, T., Bley, C.J., Thierbach, K., Petrovic, S., Schilbach, S., Mayo, D.J., Perriches, T., Rundlet, E.J., Jeon, Y.E., Collins, L.N., et al. (2015). Architecture of

the fungal nuclear pore inner ring complex. Science *350*, 56–64.

Sun, C., Yang, W., Tu, L.-C., and Musser, S.M. (2008). Single-molecule measurements of importin α/cargo complex dissociation at the nuclear pore. Proc National Acad Sci *105*, 8613–8618.

Sund, S.E., Swanson, J.A., and Axelrod, D. (1999). Cell Membrane Orientation Visualized by Polarized Total Internal Reflection Fluorescence. Biophys J *77*, 2266–2283.

Tagliazucchi, M., Peleg, O., Kröger, M., Rabin, Y., and Szleifer, I. (2013). Effect of charge, hydrophobicity, and sequence of nucleoporins on the translocation of model particles through the nuclear pore complex. Proc National Acad Sci *110*, 3363–3368.

Teimer, R., Kosinski, J., von Appen, A., Beck, M., and Hurt, E. (2017). A short linear motif in scaffold Nup145C connects Y-complex with pre-assembled outer ring Nup82 complex. Nat Commun *8*, 1107.

Thompson, N.L., McConnell, H.M., and Burhardt, T.P. (1984). Order in supported phospholipid monolayers detected by the dichroism of fluorescence excited with polarized evanescent illumination. Biophys J *46*, 739–747.

Timney, B.L., Raveh, B., Mironska, R., Trivedi, J.M., Kim, S., Russel, D., Wente,

S.R., Sali, A., and Rout, M.P. (2016). Simple rules for passive diffusion through the nuclear pore complex. J Cell Biol *215*, jcb.201601004.

Tu, L.-C., and Musser, S.M. (2011). Single molecule studies of nucleocytoplasmic transport. Biochim Biophys Acta *1813*, 1607–1618.

Vasu, S., Shah, S., Orjalo, A., Park, M., Fischer, W.H., and Forbes, D.J. (2001). Novel vertebrate nucleoporins Nup133 and Nup160 play a role in mRNA export. J Cell Biology *155*, 339–354.

Vovk, A., Gu, C., Opferman, M.G., Kapinos, L.E., Lim, R.Y., Coalson, R.D., Jasnow, D., and Zilman, A. (2016). Simple biophysics underpins collective conformations of the intrinsically disordered proteins of the Nuclear Pore Complex. Elife *5*, e10785.

Vrabioiu, A.M., and Mitchison, T.J. (2006). Structural insights into yeast septin organization from polarized fluorescence microscopy. Nature *443*, 466.

Wälde, S., and Kehlenbach, R.H. (2010). The Part and the Whole: functions of nucleoporins in nucleocytoplasmic transport. Trends Cell Biol *20*, 461–469.

Walther, T.C., Alves, A., Pickersgill, H., Loïodice, I., Hetzer, M., Galy, V., Hülsmann, B.B., Köcher, T., Wilm, M., Allen, T., et al. (2003). The Conserved Nup107-160 Complex Is Critical for Nuclear Pore Complex Assembly. Cell *113*, 195–206.

Wang, H., and Clapham, D.E. (1999). Conformational Changes of the in Situ Nuclear Pore Complex. Biophys J *77*, 241–247.

Wozniak, R.W., Rout, M.P., and Aitchison, J.D. (1998). Karyopherins and kissing cousins. Trends Cell Biol *8*, 184–188.

Wu, J., Matunis, M.J., Kraemer, D., Blobel, G., and Coutavas, E. (1995). Nup358, a Cytoplasmically Exposed Nucleoporin with Peptide Repeats, Ran-GTP Binding Sites, Zinc Fingers, a Cyclophilin A Homologous Domain, and a Leucine-rich Region. J Biol Chem *270*, 14209–14213.

Yamada, J., Phillips, J.L., Patel, S., Goldfien, G., Calestagne-Morelli, A., Huang, H., Reza, R., Acheson, J., Krishnan, V.V., Newsam, S., et al. (2010). A Bimodal Distribution of Two Distinct Categories of Intrinsically Disordered Structures with Separate Functions in FG Nucleoporins. Mol Cell Proteomics *9*, 2205–2224.

Yang, W., Gelles, J., and Musser, S.M. (2004). Imaging of single-molecule translocation through nuclear pore complexes. P Natl Acad Sci Usa *101*, 12887–12892.

Yumerefendi, H., Dickinson, D.J., Wang, H., Zimmerman, S.P., Bear, J.E., Goldstein, B., Hahn, K., and Kuhlman, B. (2015). Control of Protein Activity and Cell

Fate Specification via Light-Mediated Nuclear Translocation. Plos One *10*, e0128443.

Zahn, R., Osmanović, D., Ehret, S., Callis, C., Frey, S., Stewart, M., You, C., Görlich, D., Hoogenboom, B.W., and Richter, R.P. (2016). A physical model describing the interaction of nuclear transport receptors with FG nucleoporin domain assemblies. Elife *5*, e14119.

Zenisek, D., Steyer, J.A., Feldman, M.E., and Almers, W. (2002). A Membrane Marker Leaves Synaptic Vesicles in Milliseconds after Exocytosis in Retinal Bipolar Cells. Neuron *35*, 1085–1097.

Zilman, A., Talia, S., Chait, B.T., Rout, M.P., and Magnasco, M.O. (2007). Efficiency, Selectivity, and Robustness of Nucleocytoplasmic Transport. Plos Comput Biol *3*, e125.

Zwerger, M., Eibauer, M., and Medalia, O. (2016). Insights into the gate of the nuclear pore complex. Nucl Austin Tex *7*, 1–7.